# Fundamental Aspects of the Exchange Bias Effect in (Ni/Co)/$Ni_xMn_{100-x}$/(Ni/Co) Bilayers, Trilayers and Multilayers on $Cu_3Au(001)$


zur Erlangung des
DOKTORGRADES DER NATURWISSENSCHAFTEN
(DR. RER. NAT.)
Im Fachbereich Physik
der Freien Universität Berlin
eingereichte Dissertation von

**Tauqir Shinwari**
aus Landikotal,
Khyber Pakhtunkhwa, Pakistan

16. Juni 2022

This work was completed in Prof. Dr. Wolfgang Kuch's research group at the Physics Department of Freie Universität Berlin.

**Erstgutachter:** Prof. Dr. Wolfgang Kuch
**Zweitgutachterin:** Prof. Dr. Katharina J. Franke

**Datum des Promotionskolloquiums**: 09. 02. 2022

# Abstract

This study is concerned with three broad topics facing the technological application of exchange bias (EB). The antiferromagnetism of single-crystalline $Ni_xMn_{100-x}$ ultrathin films in contact with ferromagnetic (FM) Co (Ni/Co) film(s) in bilayers, trilayers and multilayers on $Cu_3Au(001)$ deposited under ultrahigh vacuum conditions, is investigated by means of magneto-optical Kerr effect (MOKE).

In the first study, the aim is to identify the contribution of interface and bulk antiferromagnetic (AFM) spins to the EB. Structural or chemical defects are deliberately introduced at the surface of the AFM layer or at a certain depth inside the AFM layer. The creation of defects in the bulk of the AFM layer enhances the magnitude of EB and its blocking temperature. It is also observed that the deeper the insertion of defects, the higher the value of the EB field and coercivity. These findings are discussed as the effect of additional pinning centers in the bulk of the AFM layer.

In the second problem, we compare artificially layered [Ni/Mn] films with the corresponding disordered $Ni_xMn_{100-x}$ alloys with almost the same Ni/Mn ratio and the same film thickness. It is revealed that the perpendicular interatomic lattice distance is decreased in the artificially layered [Ni/Mn] samples. These changes in the structure are discussed as the buckling or reconstruction of Mn atoms (probably Ni atoms too) in the bulk and also at the surface, which causes higher coercivity, EB-field, and stronger interlayer exchange coupling.

In the third project, we unveil that a cover of Mn films that exhibit contracted vertical-to-in-plane lattice constant ratio and expanded structures at different thickness levels, induces perpendicular magnetic anisotropy (PMA) in an FM layer, confirming that the interlayer distance in the AFM can be a crucial parameter for establishing perpendicular magnetization.

# Kurzfassung

Diese Studie befasst sich mit drei breit gefächerten Themen, welche die technologische Anwendung des Exchange Bias (EB) (zu Deutsch: Austauschverschiebung) betreffen. Der Antiferromagnetismus von ultradünnen einkristallinen $Ni_xMn_{100-x}$ Filmen, welche sich im Kontakt zu ferromagnetischen (FM) Co (Ni/Co) Filmen, die in Zwei-, Drei- oder Mehrlagen systemen auf $Cu_3Au(001)$ im Vakuum aufgedampft werden, wird mithilfe des magneto-optischen Kerr-Effekts untersucht.

Das Ziel der ersten Untersuchung ist es den Beitrag zum EB von antiferromagnetischen (AFM) Spins an der Grenzfläche und in tieferen Lagen zu bestimmen. Strukturelle oder chemische Defekte werden absichtlich auf der Oberfläche der AFM-schicht oder in einer bestimmten Tiefe eingebracht. Die Erzeugung der Defekte tiefer in der AFM Lage bewirken eine Verstärkung des EB sowie eine Erhöhung der Blocking- (Sperr-) Temperatur. Es wird weiterhin festgestellt, dass mit zunehmender Tiefe der Defekte das EB- sowie das Koerzitivfeld zunehmen. Die Beobachtungen werden als Effekt von zusätzlichen Pinning-Zentren in der Tiefe der AFM-Lage diskutiert.

Als zweites System vergleichen wir künstlich erzeugte Anordnungen von [Ni/Mn]-Lagen mit dazugehörigen ungeordneten $Ni_xMn_{100-x}$ Legierungen, welche das gleiche Ni/Mn-Verhältnis und die gleiche Filmdicke besitzen. Es wird gezeigt, dass der senkrechte inter-atomare Gitterabstand in den [Ni/Mn]-Filmen mit künstlicher Lagenanordnung abnimmt. Die strukturellen Änderungen werden als Ausbeulen oder Neuanordnung der Mn-Atome (wahrscheinlich auch der Ni-Atome) in den tieferen Lagen und an der Oberfläche diskutiert, welche das hohe Koerzitivfeld, EB-Feld, und die starke Kopplung zwischen den Lagen bewirken.

Im dritten Projekt wird aufgezeigt, dass eine Mn Schicht, welche ein reduziertes Verhältnis der vertikalen zur ebenen Gitterkonstante sowie verschiedene Strukturen bei unterschiedlicher Lagendicke besitzt, eine senkrechte magnetische Anisotropie (perpendicular magnetic anisoropy or PMA) in einer anliegenden ferromagnetischen Schicht bewirkt. Dies beweist, dass der senkrechte Lagenabstand im AFM ein kritischer Parameter für die Erzeugung einer vertikalen Magnetisierung ist.

# Contents

# 1 Introduction

## 1.1 Nanotechnology and magnetic data Storage

Nanotechnology and nanoscience are the leading modern research fields in engineering and science, respectively. Both have the potential to reshape the world around us. It has so many useful applications; one of the most useful and demanding among them is "data storage". The earliest form of storage used by humans was using paper, tape, stone, and in the form of "brain". The brain is the natural data storage system, but it is not enough for all purposes. One can use the brain for the storage of specific kinds of information, but how reliable the information is, it depends on the circumstances and individuals. Also, the information saved inside the brain cannot be shared or transferred if that person no more exists. So basically, humans need the data storage for two purposes. The first one is to preserve reliable data and retrieve it when we need it. The second is to communicate and share authentic information or data with others. With time when human beings realized these facts, they invented other means of storing data and information.

It was probably more than a century ago, when Valdemar Poulsen invented the magnetic recording system. After thirty years of that invention, magnetic tapes were commercialized successfully. It fulfils some of the features quite well, it was utilized for audio recording and archival, but the weakness was they lacked random access. So access time comparatively was too much longer than in other systems, available at that time such as punch cards. The solution then came in the form of the first hard disk drive (HDD), it was introduced in 1956 by IBM. In this form, now one can have both benefits of magnetic recording and random access capability. The suitable name for that HDD was the random access method of accounting and control (RAMAC). Using 50 magnetic discs (24 inches of diameter each), RAMAC had a capacity of 5 MB. For each magnetic disc, areal density (AD) was 2 kilobits/in$^2$. After a lot of effort and hard work, the technology behind each part of HDD was developed with time. In more than 60 years, scientists are able now to have an AD of more than 1 Tbits/in$^2$. The bit dimensions are already in the length of

nanometer and thoroughly shrinking because of the growing market for greater recording densities. It is assumed that if the tempo of the AD graph is kept moving at the current speed for the next few years, then no doubt the size of the bit will attain the sub-10 nm level. At this stage, the read and writing procedures will become very tricky.

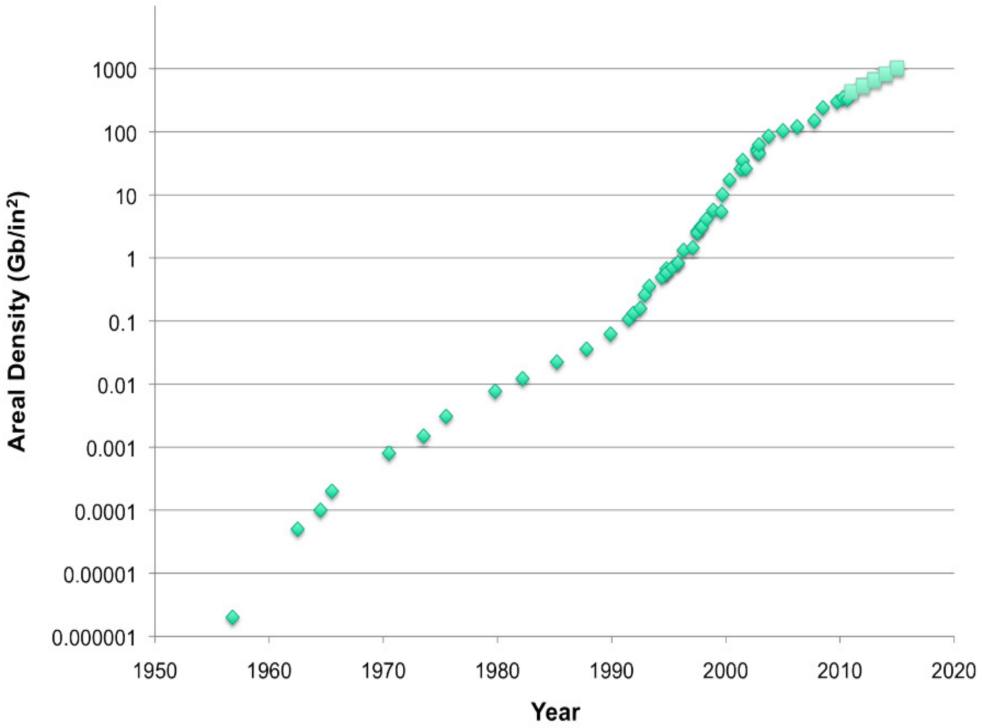


**Figure 1.1:** Schematic diagram of the areal density evolution for HDD memory products

The fast contraction of recording bit size poses difficult tasks to the read and write sensors. It is a pre-requisite of the practical devices that the sensor must be designed very tiny, equal to the bit size or less than that. At the same time, the sensitivity factor must be modified thoroughly to have a solution for the loss in signal-to-noise ratio (SNR) due to the shrinkage in the dimension of a bit. This is dependent entirely on the advance of nanotechnology [1–4]. The nanotechnology also developed magnetic random access memories (MRAMs) along with HDDs in the field of data storage [5–9]. A further advance in nanotechnology, along with a newly emerging field named "spintronics", is the key to areal densities of more than 1 terabits/in$^2$ in HDDs presently. The devices designed for data storage can be mainly grouped into three categories, i.e., magnetic, optical, and solid-state memory data storage. Nanotechnology is crucial for all devices based on any three types of data storage systems.

The aim and motivation behind all these efforts are to achieve higher AD and less impedance of the recording bits. It is also the target that it should be cost-effective, too. When the AD rises by 2 orders, then bit size shrinks by one order. To function well, the head size must be smaller than the bit size to write and read on these tiny bits, and the spacing between the tiny head and rotating disc should be close enough to each other. At present, researchers are only improving with these issues in the form of making multilayer media, and it improved the thermal stability of the bits but still there is a long way to go for achieving the ideal solution. This is a very challenging task, and nanotechnology can play a crucial role here using nanofabrication techniques [10–12]. Soon, the size of the sensor will reach less than a few nm, and at that point, there may not even be an answer from the semiconductor technology. In addition to the designing issues, one can also think about increasing the performance or the output of the sensors. From the above brief discussion one can realize the significance of nanotechnology in the field of data storage. Spintronics has a very close relation to nanotechnology in a way that most of the surface and bulk magnetism phenomena have a characteristic length in the units of a nanometer.

## 1.2 Spintronics

Moore's law has been practiced for so many years in the area of information technology (IT). Gordon Moore (Intel's co-founder) predicted in 1965 that, "the number of transistors on an integrated circuit would double about every two years". That prediction adequately described a trend that has continued for several decades. In the last couple of years, the inherent complexities of the semiconductor-based technology have increasd. These extreme complexities, even that the transistors are now three-dimensional, slowed down the pace of Moore's law. The miniaturization almost changed every aspect of our lives. To keep the advancement of electronics in line with Moore's law, new technology is required. Spintronics is a promising field and will have a significant impact on modern science and technology. Here the electronic spin can easily be controlled with the help of an external magnetic field without suffering from the electrostatic screening effect. Normally this screening effect occurs when the charges are subjected to an external electric field. Magnetic material conductivity can be changed without altering the carrier distribution within the material. This is the foundation of giant-magnetoresistance (GMR) based electronics or, in other words, magnetoelectronics, which comes under the umbrella of spintronics [13–23]. In a broader context, the field of spintronics includes every type of electronics which exploits both functionalities of

electrons, i.e., spins and charges. The specialty of semiconductor-based electronics is to exploit the charge of the electrons solely, but it is difficult for them to take care of spins, while magnetic materials manipulate the spin easily and vice versa. So do we have materials that can take care of both charges and spins at the same time? The answer for the moment is "yes," these materials are named as magnetic semiconductors [24–43].

With the availability of ultra-high vacuum technology, scientists developed a technique that allows the deposition of ultra-thin films with an amazing accuracy in thickness manipulation. In this technique, the evaporated atoms or molecules deposit directly on the surface of substrate to initiate the growth of ultra-thin films. The foundation of the molecular beam epitaxy (MBE) process was laid by K. G. Günther. The films he synthesized were not epitaxial, as he used glass substrates for those films. Davey *et al*. were the first to grow GaAs epitaxial films on a single crystal in an ultra-high vacuum, exploiting Günther's method. J. R. Arthur made a further significant contribution to growing films by MBE in the 1960s [44]. Being such a promising technique, the magnetic surface community decided to use MBE to grow multi-layer structures of various materials. This process made it possible to grow different super-lattice structures, of even a few atomic layers of thickness. The thin films grown in this fashion were then used to probe surface magnetism and magnetic interactions across an ultra-thin nonmagnetic spacer [45]. These studies mainly open all the way towards the discovery of GMR in Fe/Cr super-lattices.

The GMR effect, which is an updated version of AMR, was discovered in the late 1980s by two physicists working independently: Peter Grünberg from Jülich, Germany, and Albert Fert from Paris, France. In response to an external applied magnetic field they observed very large change in the electrical resistance in systems comprised of alternating ultra-thin layers of several metallic elements. At the time it was a huge surprise for the scientific community and this discovery led the scientists to perceive how they can exploit the power of the GMR effect. The drastic change in the electrical resistance of the multilayer system arises when the applied field aligns the spin configuration of the sequential FM layers. In the absence of the external magnetic field the magnetic moments of the FM layers are antiparallel to each other. Application of the external magnetic field aligns and saturates the magnetization of the FM layers, which leads to a sudden drop in the electrical resistance of the multilayer.

In the GMR effect, the quantum nature of electrons is exploited. Conductive electrons with spin orientation parallel to the magnetization of the material move freely while the motion of those electrons with anti-parallel ori-

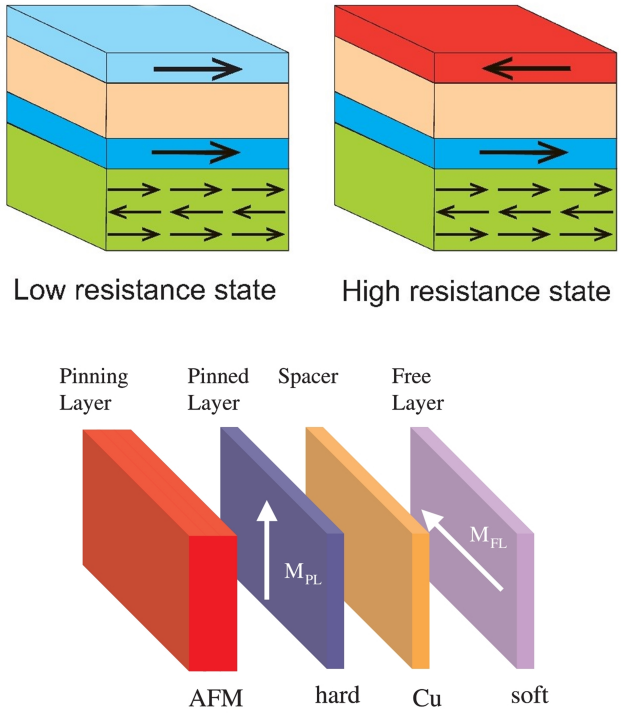


**Figure 1.2:** Principle of a spin valve GMR sensor. The magnetization of the lower FM layer is pinned by an AFM layer through an exchange-coupling. The top FM layer is parted by a nonmagnetic but conducting spacer layer such as Cu, and its magnetization can be controlled by rather small fields.

entation is blocked. When there is an alignment of the magnetic moments between the two FM layers, spin-up electrons move freely in both magnetic layers, which corresponds to the low-resistance configuration. On the other hand, when the magnetic moments of the two FM are anti-aligned, motion of spin up electrons is hindered by one FM layer, while the movement of spin down electrons has resistance from the other FM layer, resulting in a higher resistance. In the GMR sensor, a recorded bit rotates the magnetization of the free FM layer relative to that of the pinned FM layer, effectively switching the device between these two possible arrangements, i.e., either high or low resistance.

A spin-valve is a multilayer GMR device and is very promising for read-head applications in HDDs. Spin-valves in its simplest form consist of a non-magnetic spacer such as Cu, which is sandwiched between two FM layers (normally permalloy or CoFe) and an AFM layer such as NiMn, which is also in physical contact with one of the FM layers. It is customary that the non-magnetic spacer thickness must be so thin that there is a possibility of slight

exchange coupling among the two FM layers. The AFM layer pins one of the two FM layers which is deposited next to it. The device structure is illustrated schematically in Fig. 1.2.

For its proper operation, both pure semiconductor-based transistor and spintronics-based spin valve needs some bias. To get a linear response with minimized asymmetry, the spin-valve typically needs a proper magnetic bias. One of the main targets of the construction of the spin-valve is to establish the pinned FM layer as rigid as possible with an AFM layer, which indirectly means to keep thermal stability at higher temperatures. At the junction where FM/AFM is pinned, the exchange energy dictates the magnetic order while the anisotropy defines the easy and hard axes of magnetization. In general, FM material has a smaller anisotropy but greater exchange energy, which enables it to sustain its magnetic order at elevated temperatures. On the other hand, AFMs, in general, show higher anisotropy values and accordingly hold preferred orientations. Coupling between an AFM and FM at the interface in GMR spin-valve may provide a unique effect, i.e., strong magnetic order and larger anisotropy, where anisotropy may be a unidirectional feature that normally one cannot find in FMs. The magnetic hysteresis loop linked with an AFM-FM interface can show non-centrosymmetric behavior at some non-zero magnetic field; this effect is named as exchange bias. Exchange bias is used to pin the magnetization (as firm as possible) of the FM layer with an AFM layer in these kinds of structures.

The exchange bias is not a new topic; it was discovered several decades ago. In the EB phenomenon, not only the coercivity ($H_c$) of the FM changes, but the hysteresis loop also shifts along the magnetic field axis. Although it is accepted that EB is an interfacial phenomenon where the spin-spin interaction occurs at the FM/AFM junction, EB is influenced by various other parameters, too. These other parameters might include interface roughness, chemical order, magnetic proximity effects, crystalline structure, composition, and many more. EB is a very complex issue having a very subtle nature, and its behavior varies from system to system and case to case. Despite its importance in day to day life and a large quantity of work done on the topic, its nature and origin are not yet well defined. A considerable amount of theoretical models have been introduced to explain the experimental results. Few of these models are (1) Domain state model, (2) the Neel model, (3) the coherent rotation model (4) the random and compensated interface model, (5) the random interface model (6) the AFM domain- wall model, (7) the interface spin canting model and so on [138]. Some of these models, which we will use to discuss our results, will be briefly discussed in chapter 2.

## 1.3 Criteria for choosing AFM materials

Up to now, several AFM materials have been studied to be used in reading heads of the spin-valve for practical usage. To achieve a trustworthy and proper operation of the spin-valve, the following six parameters in no particular order have to be chosen wisely when selecting the AFM materials.

### 1.3.1 Strength of the EB field ($H_{eb}$)

As discussed earlier, that pinned or reference layer plays a vital role in spin-valve operations. It can lead to the degradation of the output signal and asymmetry due to thermal fluctuations. The exchange bias field (pinning field) must have a high value ($>$ 30 mT) to make the pinned layer "firm" in the presence of some external field B.

### 1.3.2 Thermal stability and blocking temperature ($T_b$)

$H_{eb}$ usually decreases with the temperature of AFM materials, and the temperature at which it becomes zero is named “blocking temperature”. How fast $H_{eb}$ decreases depends on various parameters and properties of the materials. Few of them are; structural, their intrinsic nature, thickness, and the way they were synthesized. A high $T_b$ ($>$260 $^0$C) is needed to make certain that the sensor works properly at room temperature or above.

### 1.3.3 Large resistivity of AFM

High resistivity material is needed because then the shunting effect is negligible, which decreases GMR. The shunting effect can also be suppressed by using a perfect insulator in the form of AFM layer (which does not contribute to MR by itself). Most AFM materials like NiO, which shows a high resistivity value of 108 (µΩ.cm), unfortunately, cannot meet other criteria and are therefore inappropriate as an AFM to be used in real devices.

### 1.3.4 Small critical thickness

The critical thickness is the minimum thickness for the AFM film to show the EB effect. For practical application devices, AFM material thickness must be selected well beyond the critical thickness, taking into account the temperature dependence of the EB. A considerable thickness of the AFM layer will yield a sizeable total width of the sensor, which is not favorable for sensor miniaturization. Hence, one should use the AFM materials with reduced critical

thickness.

### 1.3.5 Good corrosion resistance

AFM materials which show higher corrosion resistance are required for functional application devices.

### 1.3.6 Low-temperature process

The high thermal-annealing process can disturb the functioning of spin-valve. A low-temperature procedure is preferred.

Antiferromagnets composed of oxide-based (like NiO/CoO) and chromium-based alloy are the most favorite and are still the focus of recent research; one reason is that they have a high resistivity. Besides these oxide-based systems, metallic AFMs have also attracted considerable attention. Among these, Mn-based metallic AFMs are hot favorites, and numerous alloys have already made it to practical spin-valve sensors in HDDs. We can divide them into two groups. The first consists of RuMn, IrMn, RhMn, and FeMn, while the second consists mainly of PdMn, PtMn, and NiMn.The crystal structure of the first group is *fcc* while it is CuAu-I type *fct* for the second group. The alloy system FeMn is the most studied metallic AFM system in the EB field. The reason is its suitable Néel temperature ($T_N$) of 490 K. With permalloy as FM, it is one of the most widely studied systems which exhibits a $H_{eb}$ of about 42 mT for a 4 nm thick FM permalloy without annealing. This combination has potential use in EB TMR devices. However, because of weak corrosion resistance and low $T_b$ of 150 $^0$C, it is unfit for use in spin-valve applications. IrMn, with the CoFe system from the first group, needs annealing. It has better properties than FeMn systems, like corrosion resistance and smaller critical thickness. However, its moderate $T_b$ of 250 $^0$C restricts its usage in practical devices. From the second group, suitable AFM model system is the chemically ordered $L_{10}$ phase of NiMn. This NiMn system has a collinear AFM spin structure and a remarkably high $T_N$ in bulk form. The second group, compared to the first one, gives a much higher $T_b$ (350-450 $^0$C), higher EB values (50-80 mT), and better corrosion resistance and thus is fit for use in devices. The drawback of the second group of AFM materials is their respective higher critical thicknesses, which may restrict their applications in ultrahigh-density recording devices. Table 1.1 on page 9 lists the properties of some widely studied AFM materials [47–65].

| Materials | $H_{ex}$(Oe) (NiFe 4nm) | Required thick-ness (nm) | $T_b$(°C) | Reistivity ($\mu\Omega.cm$) | Corrosion Resistance | Annealing |
|---|---|---|---|---|---|---|
| NiMn | $\geq 390$ | $> 25$ [53] | 450 [53], > 425 [52] | 175 [53] | Moderate | Required [53] |
| | | $> 35$ [52] | 430 [57] | 210 [52] | Good [55,61] | |
| | | $> 30$ [55] | 400 [56,60] | | | |
| FeMn | 420 | 7 [53] | 150 [53,54], 165 [55] | 150 | Poor | No [53] |
| | | | 175 [56] | 130 [53] | | |
| | | | 170 [60] | | | |
| IrMn | 200 | 7 [52] | 190, 230 [52] | 200 | Good [51,61] | No [61] |
| | | 7.5 [55] | $\sim$ 250 [55,56] | 325 [52] | Moderate [55] | |
| | | 10 [62] | 130 [62] | | | |
| PtMn | 500 | 30 | 380 [62] | $\sim 200$ | Good | Required |
| | | | 400 [56] | | | |
| | | | 310 [60] | | | |
| PdPtMn | 280 | 25 [52,63] | 300 [63], 350 [52,56] | 185 [52] | Good | Required |
| CrMnPt | 220 | 30 [51,64] | 380 [51,64] | 310-345 [51] | Good | No |
| | | 35 [52] | 300 [52] | 300-350 [64] | | |
| | | | | 360 [52] | | |
| NiO | 200 | 35 [53] | 200 [53,58,59] 190 [55] | Insulator | Good | No [53] |
| | | 30 [55] | | $\geq 10^8$[ [51]] | Exellent [55] | |
| | | 50 [58] | | | | |
| $\alpha$-$Fe_2O_3$ | $40-75$ | 100 | 200-250 | Insulator | Good | No |
| | | | 250 [63] | | | |
| | | | 250-300 [65] | | | |

**Table 1.1:** Widely studied AFMs and a few of their properties

## 1.4 Why $Ni_xMn_{100-x}$?

NiMn plays a leading role in the second group having the highest $T_N$ of 1070 K in its bulk form [66, 67] as well as a high $T_b$ of 725 K in the form of polycrystalline thin film [68, 69] amongst both Mn-based groups. Very little experimental work on the structural and magnetic properties of single-crystalline $Co/Ni_xMn_{100-x}$ systems in the vicinity of smaller Ni concentration prepared by thermal deposition of Ni and Mn on $Cu_3Au(001)$ is published to the author 's best knowledge. Although this system may be of reasonable interest in implementations, it is assumed that the investigation would lead to a deeper understanding of the fundamental interactions at FM/AFM interfaces, about pinned magnetic moments within the volume/bulk of the AFM and it's contribution to the EB effect. Thus it is possible to consider $Co/Ni_xMn_{100-x}$ as a model system compared to systems prepared through sputter deposition techniques because epitaxially grown films allow accurate control of the interface properties down to the atomic scale. Furthermore, the absence of structural imperfections such as grain boundaries and misfit dislocations (which undoubtedly affect the magnetic properties of sputter-deposited systems) reduces the complexity of the magnetic interaction at the AFM/FM interface or within the bulk of AFM considerably.

## 1.5 Previous studies on $Ni_xMn_{100-x}$

As affirmed beforehand, amongst all Mn-based AFM alloys NiMn shows the highest $T_N$ of 1070 K, and in polycrystalline form, it has the highest $H_{eb}$ as well as $T_b$. Due to the minimal amount of lattice mismatch between the $Ni_xMn_{100-x}$ film and the substrate $Cu_3Au(001)$, it gives well-defined growth and shows similar c(2x2) structure like pristine $Cu_3Au(001)$ [70–77]. At the interface of thin films, the magnetic properties are governed by the spin structure. Which is well recognised for $Ni_xMn_{100-x}$ in thin film form as well as in bulk form, in the former case the spin structure is mostly concentration-dependent (for lower Ni concentration it is collinear and non-collinear close to the equiatomic case) in contrast, while in the latter case, the $Ni_xMn_{100-x}$ spin structure is in-plane (IP) collinear.

NiMn in the form of bulk down to ultrathin films has been extensively studied on various seed layers or single crystalline substrates since the last two decades, to find out their correlation between structure and magnetism. Being one of the most encouraging AFM systems, $Ni_{50}Mn_{50}$ depicts an *fct* $L1_0$ structure. The corresponding lattice constants of the *fct* structure are a = b

= 3.74 Å and c = 3.52 Å [78,79]. $T_N$ of chemically ordered $Ni_{50}Mn_{50}$ with the $L1_0$ structure was reported as high as 1070 K. It consists of alternating atomic sheets of Mn and Ni along the c-axis, with a contraction perpendicular to the planes [68, 80–82]. Synthesis of $Ni_{50}Mn_{50}$ films having $L1_0$ chemical order is crucial. Typically, this needs time consuming post-deposition heat treatment to persuade chemical ordering, action that may end in strong intermixing at the FM/AFM interface. For samples prepared by magnetron-sputtering, heating up to several hours at 300 $^0$C is required to persuade chemical order [54,57,67, 83,84]. Since EB is considered as an interface phenomenon, the study based on synthesized FM/AFM layers with ordered $L1_0$ NiMn films achieved by epitaxial growth is of great concern. Various investigations show that $Ni_{50}Mn_{50}$ films can be grown epitaxially on Cu(100) and Cu(111) [69, 85–87]. On Cu(111), chemical order was obtained just by heating up to 250 $^0$C in the presence of an applied magnetic field of 250 Oe for a few hours. Tieg *et al.*, suggested an c(2×2) bulk-like $L1_0$ crystal structure for $Ni_{50}Mn_{50}$, which shows growth along the a-axis on Cu(001) [86].

The EB dependency on various crystallographic directions of the AFM is an open issue. Various groups have shown that MnPd (001) with similar $L1_0$ structure can be grown epitaxially with direction either parallel or perpendicular to the surface normal, depending on the substrate, deposition temperature, or morphology of the surface [88, 89]. In the case of $L1_0$ NiMn, growth on $Cu_3Au$(001) substrates leads to c-axis direction growth and has a smaller mismatch with NiMn, compared to the Cu(001) substrate [90]. Such a tactic allowed for studying the effect of different crystallographic directions on the coupling at the FM/AFM interface for the $Ni_xMn_{100-x}$ system. When prepared by the magnetron-sputtering method, NiMn has been studied widely in its polycrystalline form. Ni/NiMn/Cu(111) required heating in a magnetic field and showed a complex temperature-dependent EB effect for a thickness of 35 Å. Tieg *et al.*, showed antiferromagnetism of $Ni_{50}Mn_{50}$ in the Co/NiMn bilayer system on Cu(001) [86]. An increase in Co coercivity has been assigned to the interfacial magnetic coupling as NiMn above 8 ML thickness has shown AFM behavior at room temperature. Reinhardt *et al.*, afterwards reproduced these results and found stronger magnetic coupling in $Co/Ni_{35}Mn_{65}$ bilayers on Cu(001) compared to $Co/Ni_{50}Mn_{50}$ bilayers [87]. In a common theoretical and experimental finding, Gao *et al.*, have revealed, with the help of spin-polarized scanning tunneling microscopy (SP-STM), that the surface spin density of NiMn thin films on Cu(001) is non-collinear, which was out of expectations at that time [69]. This was linked to the broken symmetry at the surface and explained further by the help of LEED images [69]. Only a few thicknesses and temperature-dependent MOKE measurements of Co/NiMn

IP-magnetized bilayers have been performed on Cu(001) and $Cu_3Au(001)$.

The different crystal structure has been shown related to different compositions of NiMn in its bulk form. NiMn has an fct crystal structure for $Ni_{50}Mn_{50}$ concentration with c/a $< 1$. Its crystal structure is susceptible to the Ni content. Cubic fcc lattice undertakes a tetragonal phase c/a $< 1$ or an orthorhombic phase c/a $> 1$, at lower temperatures. Bulk $Ni_{28}Mn_{72}$ depicts a non-collinear three-dimensional spin structure [71, 73]. Mitsumata *et al.*, [91] theoretically calculated comparable results for lower concentrations of Ni in NiMn, where thinner AFM films are needed for the commencement of EB for the 3Q (three dimensional) spin structure compared to the 1Q (collinear ones), due to differences in domain-wall width for both cases [28]. Mitsumata *et al.*, have generalized that the AFM domain wall width could be remarkably smaller than the FM domain wall width. Hereafter, the AFM layer thickness mandatory to introduce EB could be approximately $1/\sqrt{3}$ less for any AFM owing a 3Q spin structure compared to the ones with 1Q [28]. Interestingly, Khan *et al.* have shown some detailed work in the form of ultrathin $Ni_xMn_{100-x}$ films on single crystal $Cu_3Au(001)$ probed with FM Ni. They have experimentally obtained similar results as in the bulk for equiatomic concentration, which shows a fct structure. Khan *et al.* found that $Ni_xMn_{100-x}$ can couple to IP as well as OoP magnetized FM Ni layer, the latter can be tuned by deposition of a thin Co layer at the bottom or top of the Ni layer. Their results further recommend that for smaller Ni concentration, the non-collinear (3D) spin structure of $Ni_xMn_{100-x}$ deviates from a more-OoP to a more-IP arrangement. Which is driven by composition-dependent strain, with an associated increment in magnetic anisotropic energy to create EB at reduced $Ni_xMn_{100-x}$ thicknesses. The work of Hagelschuer *et al.*, supports these results [70, 72–77].

## 1.6 Aim of the thesis

With the help of this well established and well known $Ni_xMn_{100-x}$ single-crystalline system, we want to know whether it is possible to clarify the origin of exchange bias in this system if it is solely due to interfaces or could be also from the bulk contribution of the AFM. This work aimed to investigate the magnetic properties of the $Ni_xMn_{100-x}$ in contact with an adjoining FM Co, the magnetic easy axis of which is in IP direction. We also wanted to know if instead of the chemically disordered alloy $Ni_xMn_{100-x}$ (for $x \neq 50$), we could prepare artificial NiMn multilayer structures to see the difference in structural and magnetic properties. Last but not the least we prepared pure Mn films in form of bilayers and trilayers with Co as an FM on the same substrate, to

see the structural and magnetic properties. It might be an ideal AFM system to be employed at elevated temperatures in existing devices like read heads (which are based on GMR or TMR sensors) where $Ni_xMn_{100-x}$ as an AFM could pin the magnetization of an adjoining FM layer through the EB effect.

### 1.6.1 Outline of the thesis

This thesis is composed of six chapters. The next three contain an introduction, literature review and the experimental techniques (where the basics will be discussed), followed by chapter four, in which bilayers of $Co/Ni_xMn_{100-x}$ on $Cu_3Au$ (001) will be under discussion. Then come the last two chapters, chapter five will mainly contain work about $Ni_xMn_{100-x}$ artificial layers on $Cu_3Au$(001) with Co as an FM on top and finally in chapter six we will discuss bilayers and trilayers of Mn on $Cu_3Au$(001), probing with Co(/Ni) as an FM1 at the bottom and as an FM2 on the top. All results will be summarized at the end of the thesis.

# 2

# Fundamentals of exchange bias

## 2.1 Exchange bias

The exchange anisotropy or Exchange-bias was first introduced by Meiklejohn and Bean while studying Co FM particles implanted in their native AFM oxide CoO [92–94]. The discovery of this spectacular effect has triggered enormous interest in investigating the EB effect. As a result of the exchange interaction between the Co core and the CoO shell at the interface, the hysteresis loop shift along the magnetic field axis by the EB-field after cooling in an applied field through the Néel temperature of CoO (291 K) to 77 K. Fig.2.1 shows hysteresis loops of Co/CoO nanoparticles from Meiklejohn and Bean [92]. The particles were cooled from 300 K to 4.2 K, with either zero-field cooling (ZFC) or merely field cooled (FC) in 10 kOe.

Instead of the symmetric ZFC loop (dotted curve), the FC loop (solid curve) shifted along the field axis. The shift in the FC loop is known as the EB effect. The EB effect has been observed in various systems since this discovery, including granular systems, thin films, nanoparticles, and other magnetic nanostructures. Reference [95] comprehensively reviews prominent systems which exhibit EB effect. Meiklejohn and Bean also noticed significant rotational hysteresis in torque magnetometry of their Co/CoO nanoparticles [92,93] (see Fig.2.1(b)). Rotational hysteresis is the integrated displacement of torque curves measured by rotating the field in clockwise and counterclockwise directions in the sample plane. As shown in Fig.2.1(b), the clockwise and counterclockwise torques measured for Co/CoO nanoparticles are different. The presence of rotational hysteresis has been attributed to some irreversible changes in the magnetic state of the AFM defined after the initial FC process [48, 95, 96]. It has to be noticed that the system did not display any rotational hysteresis when it is ZFC from a demagnetized state of the FM. The coupling between the CoO shell and the magnetized Co core plays a vital role in setting the EB effect and its related properties.

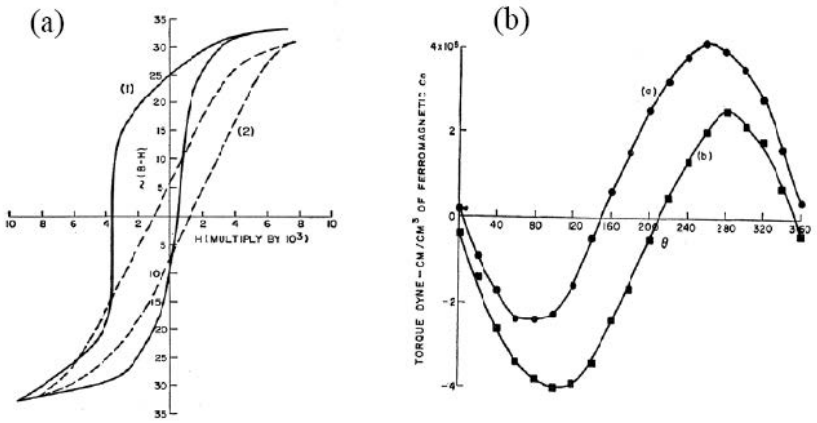


**Figure 2.1:** "(a) Hysteresis loops at 77 K of partially oxidized Co particles. Curve (1) shows the loop after field cooling in 10 kOe (the loop shift is 1600 Oe). Curve (2) shows the loop when cooled in zero field. (b) Torque curves on partially oxidized Co particles cooled in a magnetic field to 77 K. $\theta$ is the angle between the cooling field axis and the direction of the measuring field. Curves (a) and (b) in Fig.2.1(b) are for counterclockwise and clockwise rotations, respectively". Adopted from Ref. [92]

.

The EB effect discovery has motivated extensive research in nanoparticles during the last decades [48, 95, 96]. However, the bulk of work has focused mainly on thin-film systems [48,96]. There are many reasons for this preference [50]:

- **(i).** Experimentally these techniques allow the precise control and characterization of the interface [96–98].
- **(ii).** Many practical devices which are based on EB properties, are designed in the thin-film form [99, 100];.
- **(iii).** Thin films are most suitable candidtaes to carry out the investigation of specific features, such as the role of interface roughness or structure [101], interfacial coupling [102], the EB enhancement [97], cooling field dependence [103, 104], coercivity enhancement [105, 106].

## 2.2 Basic phenomenology

As discussed above, EB refers to the shift of the hysteresis loop by $H_{eb}$ along the magnetic field axis after field-cooling an FM/AFM system from above $T_N$ of the AFM (and below $T_C$ of the FM) to below $T_N$ [48, 96]. Physically, EB

originates due to the interface exchange coupling between the antiferromagnetic and ferromagnetic spins. To understand the basic phenomenology of EB, we consider a system with a well-defined interface, i.e., an FM/AFM bilayer. At temperatures well above $T_N$ but below $T_C$, the FM's hysteresis loop is centered at zero magnetic field, i.e., unaffected by the AFM (see Fig.2.2 (1)).

When an external field of sufficiently large magnitude is applied, it will align the FM spins, while the AFM spins (localized at the atomic sites) will remain random (since $T > T_N$). The hysteresis curve of the FM has centered at zero magnetic field, i.e., unaffected by the AFM. When cooling in the external field's presence, the AFM spins align with those of the FM (assuming ferromagnetic interaction). The other atomic spin planes in the AFM will follow the AFM order to produce zero net magnetization (see Fig.2.2). There will be a finite uncompensated interfacial AFM magnetization if the AFM spins are uncompensated. For simplicity, we assume single domain states for both the FM and the AFM during the magnetization reversal process. Under this assumption, if the external field has reversed, the FM spins start to rotate in-plane in the opposite direction. However, the AFM spins remain unchanged for sufficiently large AFM anisotropy (see Fig.2.2 (3)). In other means, to keep them in their original position (ferromagnetically aligned at the interface), the AFM spins exert a microscopic torque on the FM spins. Therefore, the FM spins have one stable arrangement, i.e., the anisotropy is unidirectional. Thus, the field needed to reverse an FM layer in contact with an AFM layer ultimately will be larger than the $H_C$ of the FM layer, because an extra field is required to overcome the microscopic torque (see Fig.2.2 (2)). Contrarily, when the external magnetic field has returned to the positive values, the FM spins will rotate at a smaller field due to the exchange interaction with the AFM spins Fig.2.2 (5). Therefore, the coercivity on the positive axis will reduce. The net effect in the aftermath will shift the hysteresis loop by an amount $H_{eb}$ along the magnetic field axis. The material acts as if there were an extra (internal) biasing field; therefore, the FM hysteresis loop is shifted along the field axis [92]. It has to be noticed that the AFM spins are supposed to be rigid and fixed to the field-cooling direction during the entire rotation process of the magnetic field. It is also clear that EB can also occur upon depositing the FM/AFM bilayer in a magnetic field [96].

## 2.3 Theoretical models

Although the simple phenomenological model described in section 2.2 provides a useful, intuitive picture, it lacks in quantitative understanding of the phe-

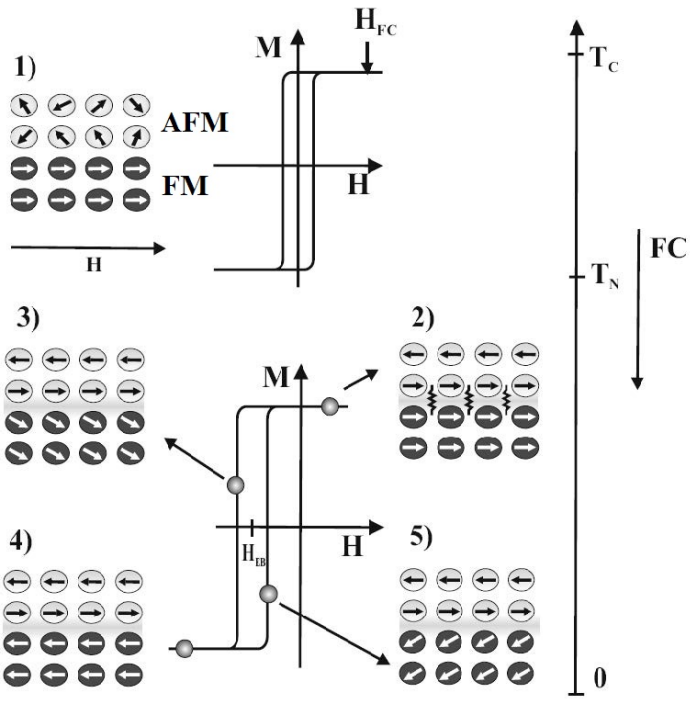


**Figure 2.2:** "Phenomenological model describing the shift of the hysteresis loop of an FM/AFM bilayer. Panel 1): The initial state showing the spin configuration at a temperature higher than the $T_N$ of the AFM but lower than the Curie temperature $T_C$ of the FM. The AFM layer is in a paramagnetic state while the FM layer is ordered. The magnetization curve of the bilayer (top-center) is centered at zero applied field. Panel 2): The spin configuration of the FM/AFM bilayer obtained after field cooling below $T_N$. The FM layer is coupled to the AFM layer. Panel 4): Saturated state of the FM/AFM bilayer at negative field. Panel 3) and 5): The spin configuration in the FM/AFM bilayer during the reversal process, assuming that this takes place through in-plane rotations of the FM spins. The magnetization curve is displaced towards negative values of the applied field by the exchange bias field $H_{eb}$". Adopted from Ref. [107].

.

nomenon. To reach a clear picture of the effect at microscopic level, one needs to consider various factors affecting EB in systems, such as anisotropy, magnetic and structural roughness, bulk, and interface spin configuration of the AFM, crystallinity, interfacial and bulk magnetic defects [48, 50, 95, 96, 107]. The EB's physical origin is generally accepted as the interface's exchange coupling between the Antiferromagnet and a ferromagnet. However, the exact microscopic mechanism by which this exchange coupling restates into $H_{eb}$ is still under debate. Several attempts have been made to model the EB phe-

nomenon. However, no single model could provide a complete explanation of the effect. In the following section, we describe some significant theoretical models of EB. As is usual, the Meiklejohn–Bean approach [92, 93] will be discussed before some more sophisticated models.

## 2.4 Meiklejohn–Bean approach

The phenomenological description of EB for the model system of section 2.2 could be extended to a more quantitative description of the coupling [92, 93]. If the coupling at the FM/AFM interface of Fig. 2.2 is taken as $J_{EB}$, then for coherent rotation of the FM layer magnetization, the system's energy per unit area can be written as [92, 93];

$$E = -\mu_0 H M_{FM} t_{FM} \cos(\theta - \beta) + K_{FM} t_{FM} \sin^2\beta + K_{AFM} t_{AFM} \sin^2\alpha - J_{EB} \cos(\beta - \alpha), \tag{2.1}$$

where H is the applied field making an angle $\theta$ with the AFM and FM anisotropy axes denoted by their respective anisotropy constants $K_{AFM}$ and $K_{FM}$. $M_{FM}$ is the saturation magnetization, $t_{FM}$, and $t_{AFM}$ are the thicknesses of the FM layer and AFM layer, respectively. $J_{INT}$ is the interface coupling constant. Angles $\alpha$ and $\beta$ represent the angles between the AFM (sublattice) and FM magnetizations concerning their respective anisotropy axes (see Fig. 2.3). For simplicity, we assume single-domain FM and AFM such that their anisotropy axes are parallel to each other along the cooling field direction. The first term in equation 2.1 represents the Zeeman interaction energy of the ferromagnetic layer with the field, i.e., the work which has to be carried out to rotate the spins in the FM along the external field. The second and third terms are the magnetocrystalline anisotropy energy terms of the ferromagnetic and antiferromagnetic layers. Finally, the fourth term represents the FM–AFM interface exchange coupling. For simplicity we assume that H is applied along the FM easy axis ($K_{FM}$), i.e., $\theta \to 0$. Equation 2.1 can now be used to describe two limiting cases.

- **Case-1;**

$K_{AFM}\ t_{AFM} \gg J_{EB}$, i.e. the AFM anisotropy is large such that AFM spins do not rotate with H, i.e. they keep aligned along the AFM easy axis so that $\alpha \approx 0$. In this case Equation 2.1 reduces to

$$E = -\mu_0 H M_{FM} t_{FM} \cos(\beta) + K_{FM} t_{FM} \sin^2\beta - \quad J_{EB} \cos(\beta) \tag{2.2}$$

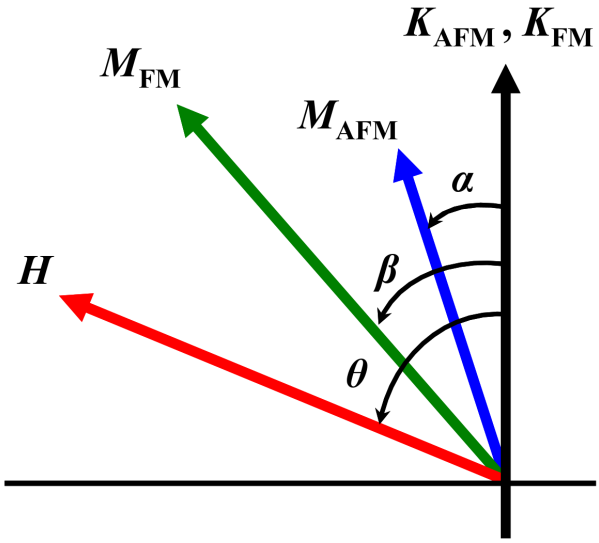


**Figure 2.3:** Vector diagram showing the net magnetization of antiferromagnet, MAFM, the magnetization of the ferromagnet, $M_{FM}$ and the applied field H. The vectors $M_{AFM}$, $M_{FM}$ and H are making the angles $\alpha$, $\beta$ and $\theta$ with respect to easy axis of ferro- (antiferro-) magnet represented by their respective anisotropy constants $K_{FM}$ ($K_{AFM}$).

.

$$E = -\mu_0 M_{FM}[H - J_{EB}/M_{FM}t_{FM}]\cos(\beta) + K_{FM}t_{FM}\sin^2\beta \tag{2.3}$$

Setting, $H_{eff}$=H-$J_{EB}/M_{FM}t_{FM}$ will make Equation 2.3 identical to the energy equation of a single-domain non-interacting ferromagnetic particle layer, the latter is given by [108],

$$E = -\mu_0 H\cos(\beta) + K_{FM}V_{FM}\sin^2\beta, \tag{2.4}$$

where $V_{FM}$ represents the volume of the FM particle. Clearly, in the present case the exchange coupling with the AFM results in a shift of the hysteresis loop of the FM by an amount

$$H_{eb} = H - J_{EB}/M_{FM}t_{FM} \tag{2.5}$$

Equation 2.5 gives Meiklejohn and Bean's expression of $H_{eb}$. It gives the expected characteristics of the hysteresis loop for an ideal case assumed in section 2.2.

• **Case-2;**

$K_{AFM}t_{AFM} \ll J_{EB}$, i.e. the AFM anisotropy is small. In this case it is energetically more favorable that the spins in the FM and the AFM rotate together during a hysteresis loop. As a result, $\alpha \approx \beta$ and equation 2.2 becomes

$$E = -\mu_0 H M_{FM} t_{FM} \cos(\beta) + (K_{FM} t_{AFM} + K_{AFM} t_{FM}) \sin^2 \alpha - \quad J_{EB} \quad (2.6)$$

A comparison with equation 2.4 reveals that in this case there will be no loop shift. However, the value of $H_C$ will be enhanced, since the overall magnetic anisotropy is modified due to the coupling. Hence the condition: $K_{AFM}t_{AFM} \gg J_{EB}$ is necessary for EB.

The simple description of the Meiklejohn–Bean model delivers an excellent fundamental argument of EB. However, there is, in general, no quantitative agreement between this model and experimental results. This model foresees hysteresis loop shift which is usually several rankings of magnitude bigger than experimentally measured in most thin-film based systems [50, 95, 96, 101, 107], although in some cases better agreement is reported [97, 109].

## 2.5 Random field model – Malozemoff

Malozemoff [110] explained the EB as originating from a random exchange field, which he ascribed to interface roughness. The rough FM/AFM compensated and uncompensated interfaces, as illustrated in Fig.2.4(a), give rise to randomness in the exchange interactions. When the system is cooled through $T_N$, the AFM experiences a random field. To minimize the exchange energy the AFM breaks up into domains (Imray- Ma domains) [111, 112] with domain walls orthogonal to the interface (Fig.2.4(b) and (c)) and sizes approximately provided by $\pi(A_{AFM}/K_{AFM})^{1/2}$, where $A_{AFM}$ is the exchange stiffness of the AFM. The statistical asymmetry of AFM moments at these domains' surfaces generates uncompensated moments at the interface that couple to the FM, resulting in EB. Despite its success in obtaining the right order of magnitude for the $H_{eb}$, this model has a critical deficiency: it imperatively depends on a defect concentration at the FM/AFM interface, which is not compatible with experimental observations. This model also lacks information about the thermal relaxation effect on the antiferromagnetic spin structure. Furthermore, the expense of energy for establishing domain walls orthogonal to the AFM/FM interface was not addressed in detail [50].

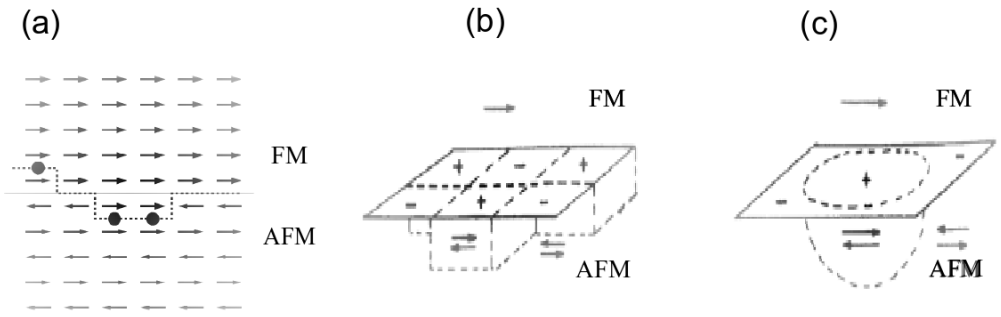


**Figure 2.4:** (a) "AFM rough interface with frustrated interactions marked by full dots. The dashed line shows the boundary between the FM and the AFM. From Ref. [50]. (b) Schematic perspective view of AFM domains (dashed lines) stabilized by a net (locally averaged) interface field surrounded by regions of net oppositely directed interface field." Arrows indicate macroscopic FM and AFM moments. (c) Enlarged view of a sole domain shown in (b). (b) and (c) are taken from the original paper of Malozemoff [110].

.

## 2.6 Domain state model

Nowak, Beckmann, Miltényi, and Misra *et al.*, [113–117] used the bilayer FM/AFM system at some finite temperatures and did Monte Carlo simulations considering defects inside the AFM and not indeed at the FM/AFM interface. They assumed that the origin of the exchange bias effect is the formation of the domains inside AFM. Because these AFM bulk domains, which are orthogonal to the AFM/FM interface, are responsible for the uncompensated moments at the interface. They also proposed that introducing more defects or disorders increases the possibility of AFM domains within certain limits, which leads to larger exchange-bias [113–117]. This model is now called as "the domain state model." The basis of this model relies on the magnetic disorder (see Fig.2.5). One can call the domain state model as "microscopic model." By microscopic, I mean that it considers the spin configuration of every atom or group of atoms inside the system's volume. In this model, to clarify the surface and bulk contribution towards EB, the disorder is introduced via magnetic dilution at the AFM/FM interface and in the bulk of the AFM layer. The foundation of the domain state model consists of an AFM layer carrying the properties of a "diluted Ising antiferromagnet (DAFF)." This DAFF should have a phase diagram like the one depicted in Fig.2.6. At the dilution dependent Néel temperature (in zero field), the system goes through a magnetic phase transition, from paramagnet to AFM transition. The antifer-

romagnetic phase is stable in three dimensions in the low-temperature range for small fields. The diluted AFM acquires a DS phase with spin-glass behavior when the external magnetic field is enhanced at low temperatures. In the finite zone of the DAFF, the statistical imbalance of two antiferromagnetic sublattices' impurities causes the development of the antiferromagnetic domains in the DS phase Fig.2.6. Because of this imbalance, the change in the system leads us to a net magnetization that couples to the external magnetic field. A spin-flip of the region, or in easy words, the creation of a domain, can relax the system's energy. At a minimum cost of exchange energy, the development of a domain wall can be precisely controlled if the domain wall moves through non-magnetic defects.

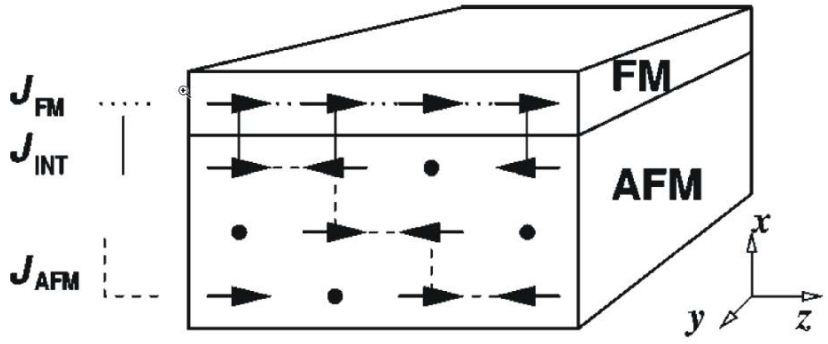


**Figure 2.5:** "Sketch of the domain state model with one ferromagnetic layer and three diluted antiferromagnetic layers. The dots represent defects". From Ref. [113].

.

In domain state model, as the AFM is modeled in a way that it must act magnetically as an diluted Ising system. The easy axis of which is same as of the FM used. Thus the Hamiltonian of their system is given as

$$\begin{aligned}\mathcal{H} = &- J_{FM} \sum_{(i,j)\epsilon FM} S_i S_j - \sum_{i\epsilon FM} (d_z S_{iz}^2 + d_x S_{ix}^2 + \mu_0 m H S_i) \\ &- J_{AFM} \sum_{(i,j)\epsilon AFM} \epsilon_i \epsilon_j \sigma_i \sigma_j - \sum_{i\epsilon AFM} \mu_0 m H_z \epsilon_i \sigma_i \\ &- J_{INT} \sum_{(i\epsilon AFM, j\epsilon FM)} \epsilon_i \sigma_i S_{jz},\end{aligned} \tag{2.7}$$

"where $\epsilon_{ij}$ are parameters used to describe fractions of sites carrying ($\epsilon_i = 0$) or not carrying ($\epsilon_i = 1$) a magnetic moment m, the $S_i$ and $\sigma_i$ represent classical spin vectors at the $i$th site of the FM and AFM, respectively. The first line describes the contribution of the FM with the z-axis as its easy axis with an anisotropy constant $d_z > 0$, and the x-axis as its hard axis with an

anisotropy constant $d_x<0$. The second line describes the diluted AFM and the third line includes the exchange coupling across the interface between FM and AFM, where it is assumed that the Ising spins in the topmost layer of the AFM interact with the z component of the Heisenberg spins of the FM. For the nearest-neighbor exchange constant $J_{AFM}$ of the AFM, which mainly determines its Néel temperature, it is assumed that $J_{AFM}$= -($J_{FM}$)/2. For simplicity, Nowak *et al.*, [113] assumed the same absolute value for the coupling constant ($J_{INT}$=± $J_{AFM}$). Nowak *et al.* [113] also assumed that the values of the magnetic moments of FM and AFM are identical ($\mu$). Eq.(2.7) suggests a simple ground-state argument for the strength of the bias field. Assuming that all spins in the FM remain parallel during field reversal and that some net magnetization of the interface layer of the AFM remains constant during the reversal of the FM. [113]"

It was experimentally shown that "the EB depends of the bulk properties of the diluted AFM, but also on the concentration of the dilution impurities. It appears that at zero dilution, the DS gives vanishing exchange bias. The exchange bias is missing at low dilutions because the domains in the AFM cannot be formed as they would cost too much energy to break the AFM bonds. Overall, it is believed that strong support for the DS model is given by experimental observations where nonmagnetic impurities are added to the AF layer in a systematic and controlled way [115, 118–120]". Also, a reasonable agreement lies within the experimental work by Ali *et al.* [121], where the reliance of the exchange bias on the temperature and antiferromagnetic layer thickness for IrMn/Co bilayers has shown.

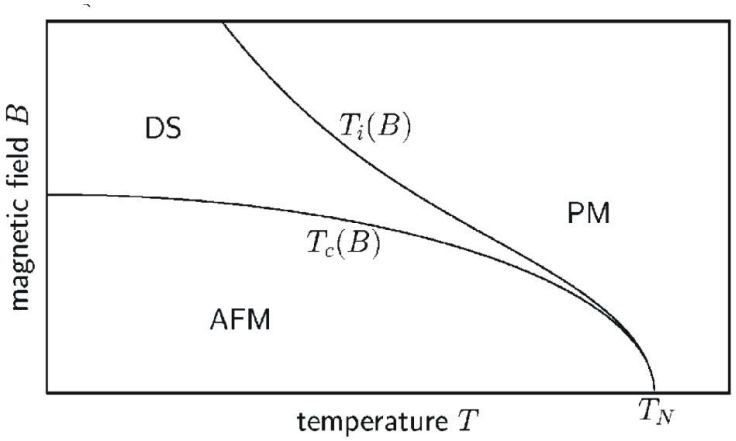


**Figure 2.6:** Schematic phase diagram of a three-dimensional diluted antiferromagnet. From Ref. [113].

.

As shown experimentally by Miltényi *et al.*, [115], the EB depends also on

the bulk properties of the DAFF layer. There, the dilution via non-magnetic defects was introduced only in the bulk of the AFM layer far away from the interface. Dependent on the Mg impurities concentration, the EB evolves as:

- "at zero dilution the exchange bias has finite values
- by increasing the Mg concentration, the EB field increases first, showing a broad peak-like behavior, and then, when the dilution is further increased the EB field decreases again.

Simulations used for the DS model showed an overall good qualitative agreement with the experimental work [115]. The peak-like behavior of the EB as a function of the dilution, as described in the work by Miltényi *et al.*, is clearly obtained in the simulations, too. However, it appears that at no inclusion of defects, the DS gives vanishing EB while finite values are observed experimentally. The EB is missing at low dilutions in the DS model because the domains in the AFM cannot be formed as they would cost too much energy to split the AFM bonds. This discrepancy [113] is thought to be explained by other imperfections such as e.g., grain boundaries in the twinned AFM layer, which is similar to dilution and which can also reduce the domain-wall energy, thus leading to domain formation and EB even without dilution of the AFM bulk.

Within the DS model, the blocking temperature can be realized by examining the DAFF phase diagram shown in Fig 2.6. The frozen domain state of the AFM occurs, following by cooling in the field below the irreversibility temperature $T_{i(b)}$. Within this study, the blocking temperature matches to $T_{i(b)}$, where in an EB system the purpose of the cooling field is complemented or substituted by the interface exchange field of the FM. Since $T_{i(b)}<T_N$, the blocking temperature should be at least somewhat below the Néel temperature and should be reliant on the strength of the interface exchange field. The simulations within the DS model reveal that EB is linearly dependent on temperature, as perceived experimentally in Co/CoO systems, but no cause for this behavior is provided [113].

Overall, it is concluded that considerable support for the DS model is provided by experimental investigations where nonmagnetic impurities are added to the AFM layer in a precise and controlled fashion [115, 118–120, 122]. Also, it seems that a good agreement is perceived with the experiments shown in Ref. [121]. The asymmetry of the magnetization reversal modes is shown to be reliant on the angle between the easy axis of the DAFF layers and the FM [114]. It was observed that either the same or different FM reversal mechanisms (coherent rotation or domain wall movement) could occur as the cor-

responding orientation between the anisotropy axis of the AFM and FM is changed" [113, 115].

## 2.7 Role of spin configuration and pinned uncompensated moments in $Ni_xMn_{100-x}$

### 2.7.1 Spin configuration and anisotropy

One of the important and basic ingredients to get exchange-bias is magnetic anisotropy energy (MAE) of the AFM, which should be greater than the interfacial exchange energy, in principle. In the early models, based on theoretical work [92,94,96,110] reporting the exchange-bias effect, the key assumption is a "collinear spin configuration" of an AFM at the FM/AFM interface. However, in reality, there are several systems in which the AFM has shown non-collinear spin structure e.g., FeMn [123–125], $Ni_{28}Mn_{72}$ [126], and $Ni_xMn_{100-x}$ [73,75,76]. Nogués *et al.*, [101] also support the fact that the spin structure at the interface of FM/AFM has strong dependency to EB. They highlighted more the role of the angle between an FM magnetization and the AFM spins for the EB. For a realistic EB model, both interdependent parameters, i.e., the AFM spin direction and magnetic anisotropy should be taken into account, especially at the interface of FM/AFM.

For AFM material (in the form of an alloy) the concentration can play a vital role in changing AFM anisotropy and its spin structure. One can play around to control the AFM anisotropy and its spin structure,one way is if the AFM is sandwiched between two FM layers. One of such specific example which could relate to our present work was presented recently by Khan *et al.*, [73]. Based on the 3Q spin structure shown by the bilayer system $Ni_xMn_{100-x}$/Ni/(/Co) on $Cu_3Au(001)$, they proposed an intuitive model (shown in Fig. 2.7). In this model it is proposed that the 3Q spin structure deviates, driven by compositional-dependent strain i.e,. from more out-of-plane (OoP) to more in-plane (IP) and vice versa. It is further added that with the decrease in Ni concentration from 50% to 20% the magnetic anisotropy of antiferromagnetic $Ni_xMn_{100-x}$ alloy increases and spin structure from more OoP switches to more IP. Fig.2.7 "shows a schematic representation of the feasible 3Q spin structure of $Ni_xMn_{100-x}$. The IP component of the surface atom spins in elongated flat (001) terraces is compensated, while the OoP spin component is not. In the upper (lower) terrace of Fig.2.7(a), all surface spins are facing upward (downward), creating a layer-wise uncompensated spin component in the OoP direction. Fig.2.7(b) represents a possible (001) surface spin config-

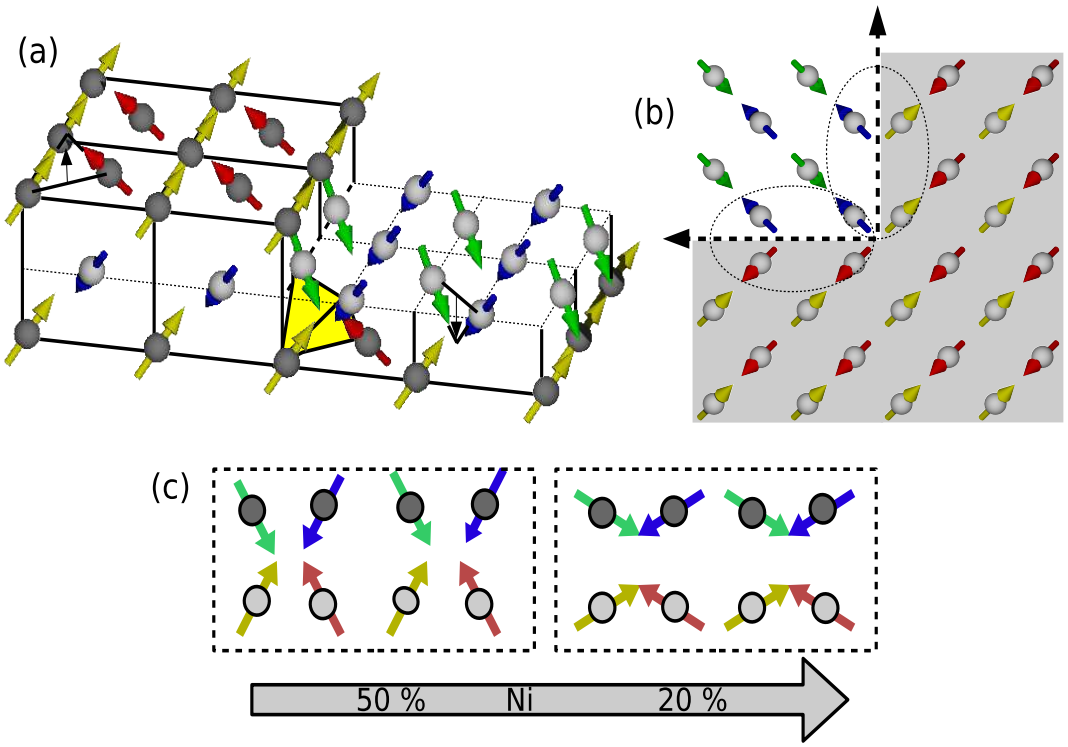


**Figure 2.7:** (a) "Schematic drawing of the non-collinear three-dimensional (3Q-like) spin structure of $Ni_xMn_{100-x}$. The different colours of the arrows representing spins only show their the four different sublattices. The tetrahedron connected by dark lines and filled yellow connects the atoms that constitute the magnetic unit cell of $Ni_xMn_{100-x}$. Within one (001) layer, all the IP spin components are compensated, but not the OoP components. (b) Top view of the spin structure at the (001) surface: the dashed ellipses show the uncompensated IP spin components at step edges. (c) The proposed change of the non-collinear spin structure of $Ni_xMn_{100-x}$ from the more-OoP to the more-IP direction upon decreasing the Ni concentration from 50 to 20 percent in a schematic cross-sectional view. The dark grey (light grey) balls represent the top (second from top) layer atoms". From Ref. [73].

.

uration of the AFM layer in a 3Q spin structure at step edges observed from the top. Light and dark coloured areas shows the next-level atomic interface planes. Ellipses at the step edges depicted by dashed lines represents areas in which the IP components of the antiferromagnetic spins do not cancel. Depending upon the concentration of Ni in $Ni_xMn_{100-x}$, the spins could be along more-OoP or more-IP directions. Fig.2.7(c) is the basis of their suggested model. It shows the situation when the spins are tilted towards the more-IP

direction on decreasing the Ni concentration from 50% to 20%" [73].

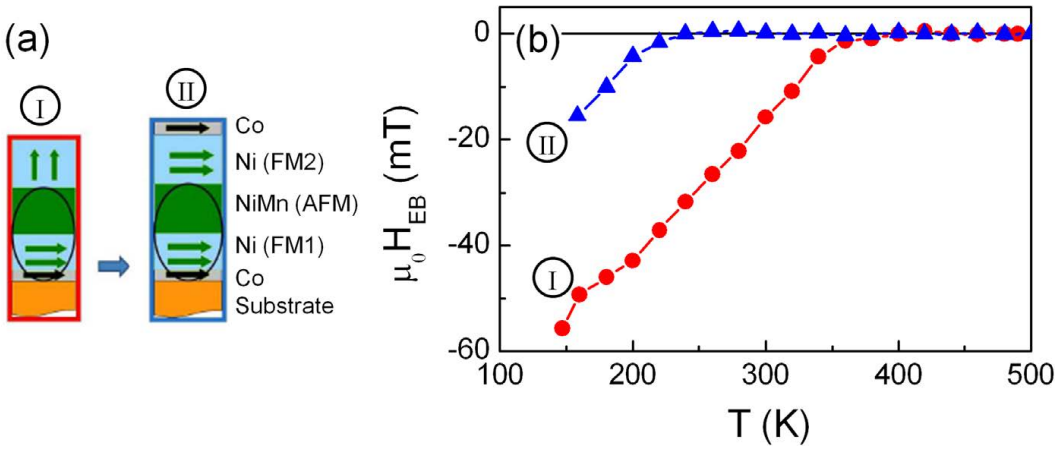


**Figure 2.8:** (a) "Fabrication steps of FM1/AFM/FM2 trilayers with in-plane/ out-of-plane (I) and in-plane/ in-plane (II) configurations. (b) Temperature dependence of the exchange bias field of the bottom Ni layer, FM1, at two fabrication steps". From Ref. [76, 127].

.

### 2.7.2 Pinned uncompensated moments (PUM)

In this section, which is related in many aspects to the DS model (described in detail in the previous section), we will discuss more specifically the role of pinned uncompensated moments in single crystalline $Ni_xMn_{100-x}$ films. Recently some groups have concluded that EB is not solely an interfacial phenomenon rather there is also some considerable contribution to the effect from the volume/bulk of the AFM layer in form of pinned uncompensated moments [75, 76, 127–130]. But the questions now are: Do the pinned uncompensated moments reside on the surface or could be found in the bulk? From where do they originate? Do the bulk spins or moments play any major role? Previously it was always thought and assumed that EB is completely an interfacial effect, where pinned uncompensated moments in the bulk only provide the support role in terms of pinning matrix. However, the experiments done by our and many other groups in recent times show evidence that AFM spins and pinned moments play an active role in establishing EB features [75,76,127–130]. We will present a brief summary of some recent work done on single crystalline $Ni_xMn_{100-x}$, which is described by help of some intuitive model and implies that bulk pinned uncompensated moments play a major role in EB.

Fig.2.8 is from a recent experiment with FM1/AFM/FM2, i.e., (Co/) Ni / NiMn / Ni(/Co) trilayers which combine IP and OoP anisotropies [76]. Here

two different ferromagnets were exploited to probe the role of bulk AFM spins. Fig.2.8(a) depicts the sample synthesis steps. In-situ L-MOKE/P-MOKE measurements were performed at each step. Fig.2.8(b) shows the temperature (T) versus exchange bias ($H_{eb}$) field graph for the same ferromagnetic layer (bottom Ni, FM1) at two fabrication steps. The EB of FM1 (always in-plane) is changed by switching the FM2 magnetization from OoP to IP. Red circles in Fig.2.8(a) correspond to the EB of FM1 as the FM2 magnetization points OoP. An ultra-thin Co layer of 2-5 monolayers tilts the FM2 magnetization from OoP to IP, and as a result, the EB of FM1 is substantially reduced (blue triangles). This reduction corresponds to the presence of pinned uncompensated moments in the AFM bulk, which magnetically connects both FM layers through exchange paths in the AFM. Or in other words, largely independent pinning centres exist for the pinning of OoP and IP directions.“

# 3

# Experimental techniques

## 3.1 Sample growth

### 3.1.1 Substrate preparation

All the experiments have been conducted under ultrahigh-vacuum (UHV) conditions at a base pressure of $2\times10^{-10}$ mbar. The UHV chamber, in which the experiments were carried out, is equipped with the necessary instruments for sample synthesis and surface characterization. The layout of the chamber is depicted in Fig. 3.1 (side view) and Fig. 3.2 (top view). A single crystal $Cu_3Au(001)$ of circular shape (having a diameter of 8 mm and height 2 mm) provided by Material Technologie and Kristalle (MaTecK) GmbH was employed as a non-magnetic substrate with miscut $\leq 0.1^\circ$. The sputtering technique in an Ar environment was used to get the clean substrate. The pressure used during sputtering was in the range of $2\times10^{-5}$ mbar. The bombardment of Ar ions in the range of 1000–1200 eV led to regular sample currents of about 2.4–3.0 $\mu$A. "Auger electron spectroscopy (AES) was used to inspect the cleanliness of the substrate prior to annealing at a temperature of about 830 K for 30 minutes. Temperatures were measured by a thermocouple of the N type that was firmly connected to the sample, mounted on the holder. After sputtering, annealing was done to restore a smooth and defect-free surface. Low-energy electron diffraction (LEED) was used to check sample surface long-range crystalline order. To confirm the excellent surface quality of the substrate, multiple sputtering–annealing cycles were performed" [148].

### 3.1.2 Film deposition

"Each metal was evaporated from a separate source utilizing electron-beam-assisted heating of high purity rods (Ni, Co: 99.99 % ), while Mn was evaporated from a tantalum crucible filled with pure Mn flakes: (99.99%)" [148]. During evaporation, the substrate was kept at room temperature. A comprehensive description of the evaporator is illustrated in Ref. [131]. "In this evaporation technique, electrons emitted from a heated tungsten filament are

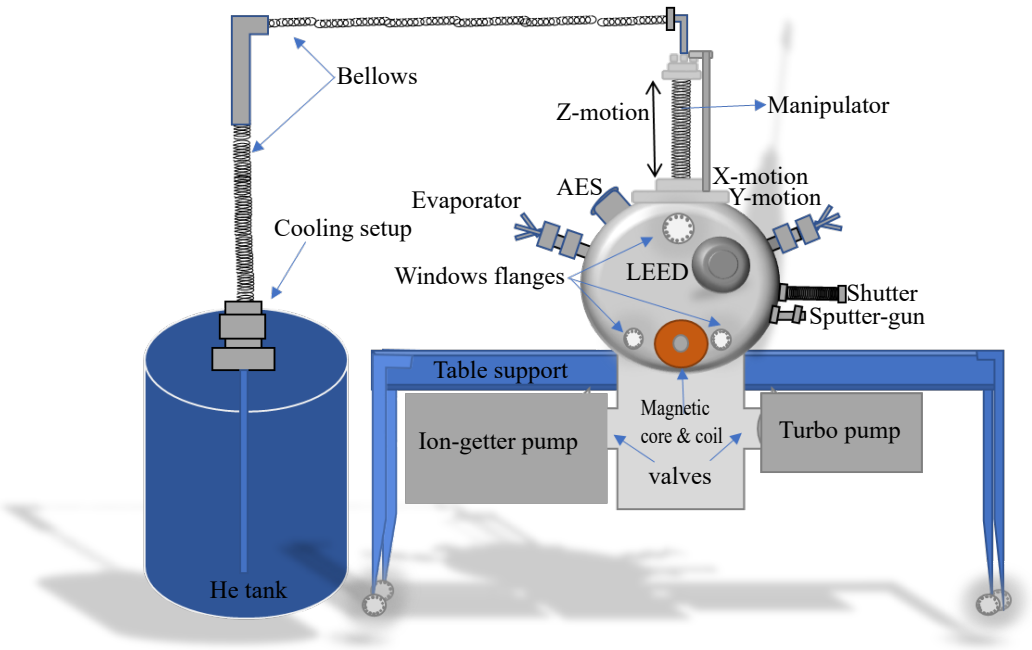


**Figure 3.1:** Schematic layout of the preparation and characterization chamber: The electron gun of the AES system and the fluorescent screen of the LEED system are utilized for MEED.

.

accelerated in a concentric electrostatic field to the tip of the crucible or rod, which is kept at positive potential (1 kV). The heating power, which was typically used between 8–25 W, can be adjusted by the few parameters, e.g., filament current, the rod potential, and the tip-to-filament (/crucible) distance " [148]. An integrated flux meter (within the Oxford Applied Research mini e-beam EGN4 evaporator with slight modifications), senses the ionised atoms in the vapour state and provides a direct measure of the evaporation rate. The flux measurement in this way is very helpful, in case, if no medium-energy electron diffraction (MEED) oscillations could be achieved for thickness control and calibration. Reproducible and stable deposition rates can be accomplished if regular evaporating parameters and a uniform geometry of tip-to-filament are preserved. The layer thickness was monitored by looking at the MEED oscillations of Co, Ni and Mn on a $Cu_3Au(001)$ substrate.

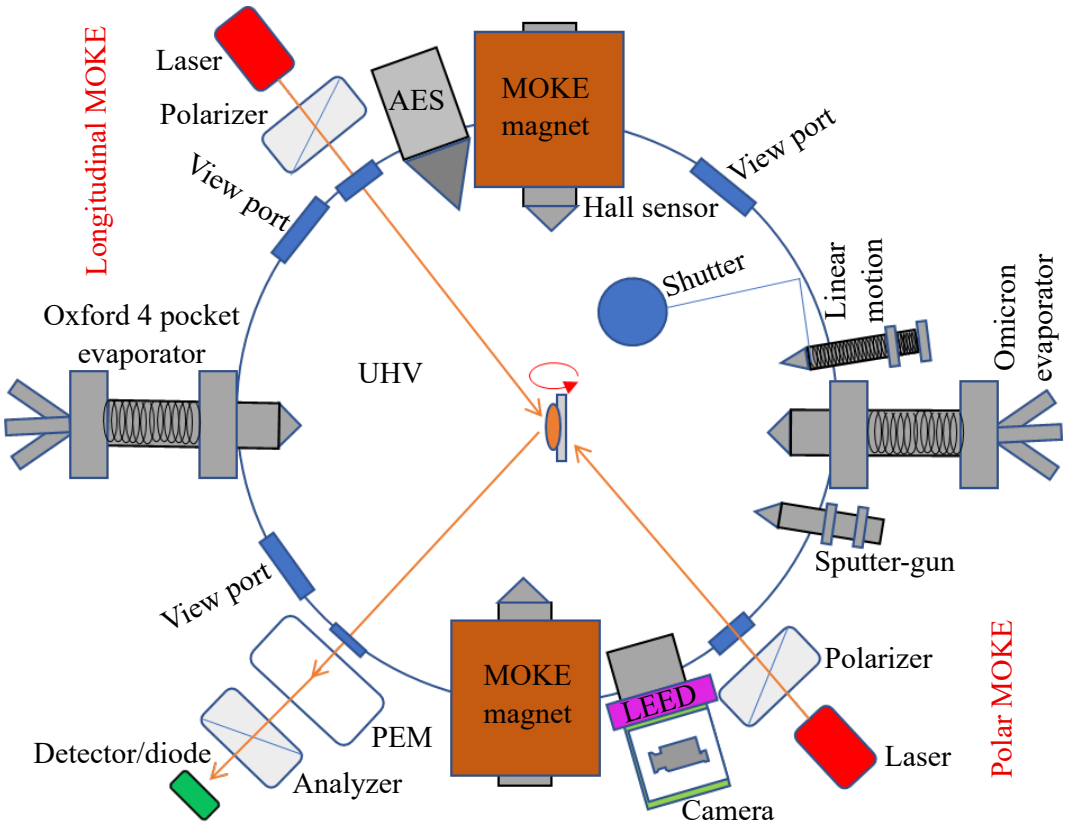


**Figure 3.2:** Top-view of the preparation and characterization chamber

.

## 3.2 Sample characterization techniques

### 3.2.1 Auger electron spectroscopy

The substrate, before doing a new experiment, was cleaned by Ar ions with an energy of 1–1.2 keV, followed by AES scans to check the cleanliness. AES requires ultrahigh-vacuum conditions, and is one of the most commonly used surface sensitive techniques for determining the composition of the surface layers of a sample. It uses the emission of electrons in the Auger process. During relaxation of the core level holes, Auger electrons are emitted from the atoms, the energy of these electrons are determined by the critical parameter, i.e., the electronic structure of the elements. As the electronic structure of an atom of each element is unique, "the Auger electrons also give the fingerprints of all the elements, except H and He [132]". The AES system comprises an integral electron gun, with an acceleration of 3–5 keV to focus and accelerate electrons towards the sample. The sample is positioned at the focal point of the Auger gun. The emitted electrons are deflected by an AES component named

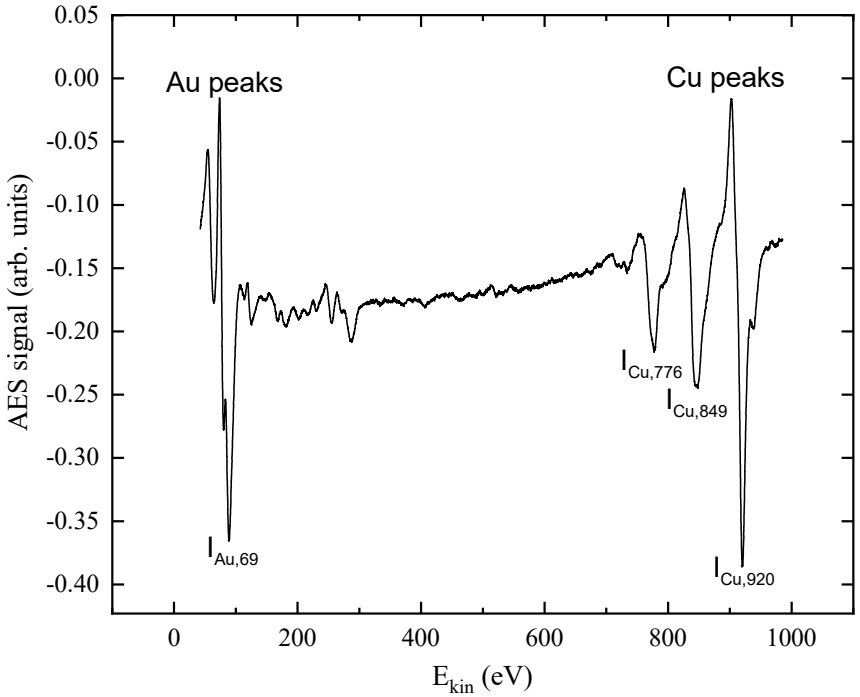


**Figure 3.3:** Auger spectrum from clean $Cu_3Au(001)$. The number in the subscript along with the element name represents the relevant AES peak energy in electron volts (eV).

.

"cylindrical mirror analyzer" (CMA). "CMA collects the favourable energetic electrons into the detection unit, multiplies the signal and send as a voltage signal to the lock-in-amplifier. From there the voltage signal is then locked to the CMA sweeping power supply as a reference frequency. The sweeping power supply is used to tune the electric field on the CMA and to collect Auger electrons as a function of their electron energy" [138]. When the sample is bombarded with accelerated electrons, holes in the core level are produced which are immediately filled by an upper-level electron, releasing the extra energy in the form of x-ray fluorescence, or this energy can be transmitted to any other electron. By exploiting the kinetic energies of emitted electrons, one can recognize different elements, as each of them has characteristic peaks at some specific energies in the Auger spectrum. From those peaks, one can get qualitative as well as quantitive information regarding the surface of the film, in some limits. A characteristic spectrum taken from the clean $Cu_3Au(001)$ substrate is shown in Fig. 3.3. From this figure, "the three prominent peaks of the LMM Auger transitions at 776 eV, 848 eV, and 920 eV can be identified for copper. For gold, the most noticeable peak is at an energy of 69 eV. The presence of surface contamination is beneath the detection limit of the Auger system" [138], less than 3% of a monolayer.

### 3.2.2 Low-energy electron diffraction

The result of an accident in the laboratory of Davisson and Germer in 1925 [133] not only marks a historic step in the development of quantum mechanics but also gave birth to the most powerful tool for the structural analysis in the field of surface science, namely low-energy electron diffraction (LEED). LEED provides qualitative as well as quantitative structural information about crystalline sample surfaces. This well-established diffraction technique has nowadays reached a grade of sophistication, allowing the retrieval of surface structures with a precision as low as 0.01 Å. A comprehensive overview can be found in Refs. [134–136]. LEED probes the long-range structural order within the surface-near region (5–l0 Å) by employing low energy electrons that have de Broglie wavelengths in the order of inter-atomic distances. In a LEED system, the sample is at normal incidence to a finely focused electron beam (spot size$<$ 1 mm) at energies in the range of 50–500 eV. A fluorescent screen is used in conjunction with a multiple-grid retarding field analyzer to map the intensity distribution of elastically back-scattered electrons that emerge from the sample surface. The intensity of elastically back-scattered electrons, even at peak maxima, is of the order of only 1% of the incident beam current ($\mu$A). The energy-dependent diffraction pattern, especially spot position, spot profile, spot intensity and intensity distribution, contains information on the size and shape of the surface unit cell, on the nature and number of defects as well as on the atomic arrangements, not only of ordered but also for disordered structures. In a kinematic description, the diffraction amplitude is given by the Fourier transform of the electron charge distribution. Therefore, the diffraction pattern is a direct representation of the reciprocal lattice of the surface. A diffraction spot occurs on the screen if the diffraction condition is fulfilled, i.e., at the intersection of the Ewald sphere, whose radius is defined by the wave vector of the incoming electrons, with an integer reciprocal lattice vector. Fig. 3.3 shows the reciprocal lattice for the real space corresponding to the c(2x2) structure of the $Cu_3Au(001)$ substrate.

Instrumental limitations, which are caused by the finite spatial and temporal coherence of the electron beam, give rise to a finite size of the LEED spots even in the case of a perfectly periodic structure. This inherent property is characterized by the term “transfer width”, which has a typical value of about 100 Å. Unlike x-ray diffraction, where the Born approximation is valid, the calculation of LEED intensities demands a dynamical theory which takes the high probability of multiple scattering events into account. In this work, a LEED system [131] with a three-grid retarding field analyzer was used.

As already described, the peak positions yield only information on the

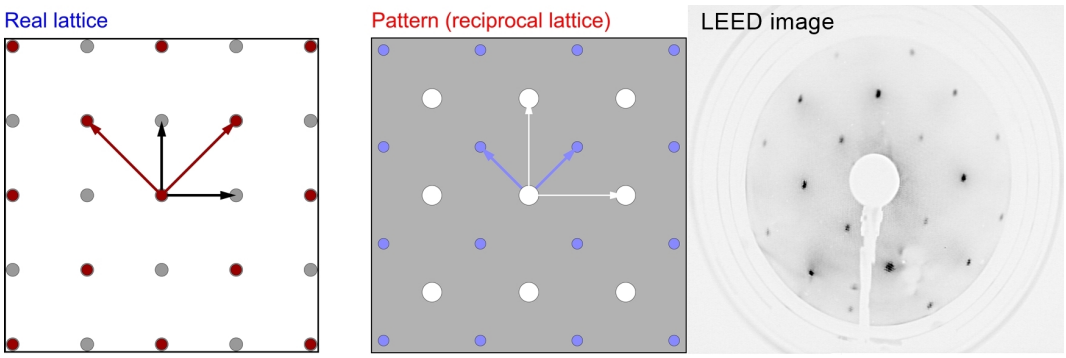


**Figure 3.4:** Simulated LEED pattern of the clean *fcc* $Cu_3Au(001)$ substrate in real space (on the left), in reciprocal space (in the middle), and on the right is the LEED image for 117 eV electron energy. $Cu_3Au(001)$ alloy substrate depicts p(1x1) symmetry (brown and white spheres in real and reciprocal space, respectively) and a clear c(2×2) superstructure (grey and brinjal spheres in real and reciprocal space, respectively). The brown and white arrows in real and reciprocal space are the basis vectors for p(1x1) while black and brinjal arrows in real and reciprocal space are the basis vectors for c(2x2) superstructures.

.

size and shape of the surface unit cell. The actual structural information, i.e., the atomic arrangement within the unit cell, is hidden in the spot intensities. The atomic positions can be obtained from the evaluation of the intensity-versus-voltage dependence of LEED spots. The voltage sweeps in these so-called LEED I(V) measurements (shown in Fig. 3.4) are equivalent to a variation of the momentum transfer vector along the surface truncation rods in reciprocal space [138]. Although sophisticated dynamical theories have to be applied to extract precise structural data, the great advantage of a LEED I(V) measurement is its relatively low experimental effort compared to surface x-ray diffraction techniques. A kinematic evaluation of LEED I(V) curves of the specular spot is already capable of retrieving the inter-atomic layer spacing along the surface normal with reasonable accuracy. Due to the vanishing in-plane momentum transfer vector, the (0 0) spot intensity does not contain information about the lateral atomic positions. The peak maxima and minima in the LEED I(V) curves originate from constructive or destructive interference of the electron waves which are scattered from atomic planes. Besides primary Bragg reflections also secondary peaks from multiple scattering events may be present in the intensity curves. In the kinematic approximation, the interlayer spacing is obtained from the energetic positions of a set of Bragg peaks. Using Bragg's law ($2d \cos \alpha = n\lambda$) and de Broglie's relation, which links via $p = h/\lambda$

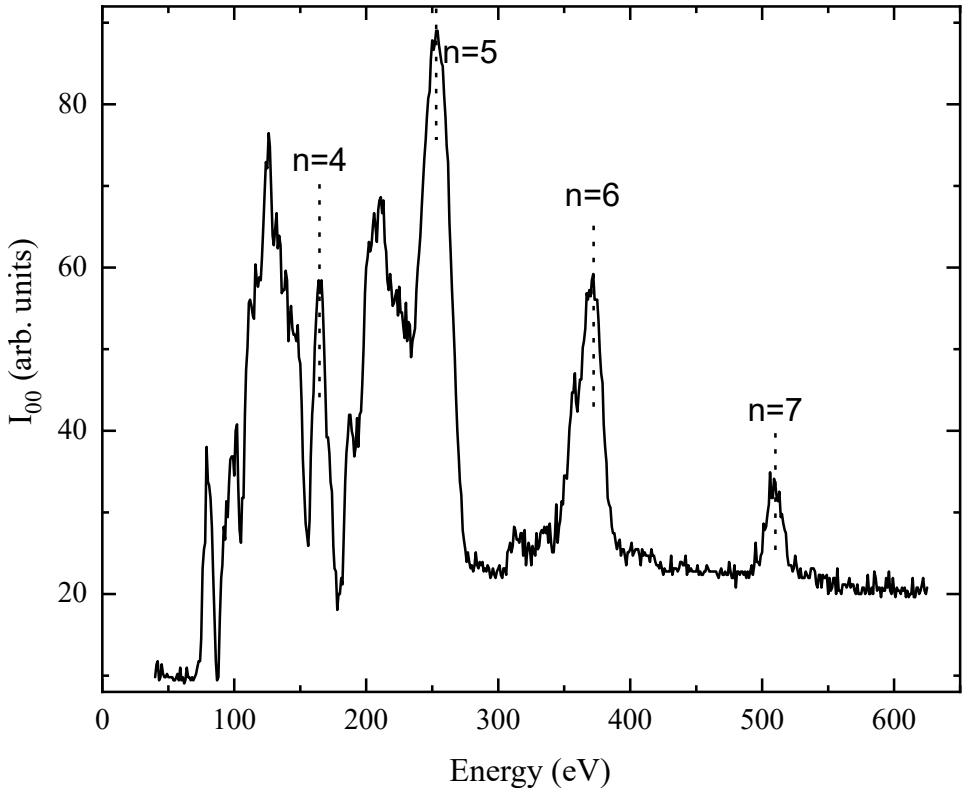


**Figure 3.5:** Room-temperature LEED I(V) curve for the clean ordered $Cu_3Au(001)$ substrate.

. from the material

the momentum p with the wavelength $\lambda$ of a quantum particle, the interlayer spacing d is given by;

$$d = \frac{nh}{(2\cos\alpha\sqrt{2m_e(E(n) - V_{ir})})}, \tag{3.1}$$

where "$\alpha$, $m_e$ and h denote the angle between sample normal and incident electron beam, electron mass, and Planck's constant, respectively. E(n) refers to the energy of an intensity maximum which corresponds to a Bragg peak of the order of n. $V_{ir}$ describes the real part of the complex inner potential. That is the energy difference ($V_{ir}$, $< 0$) between the vacuum level and the plateau of the muffin-tin potential. This correction value takes into account that the electrons gain energy when they enter the solid from the vacuum. The actual value of d is retrieved from a linear regression of E(n) versus $n^2$" [138]. The slope of these curves is related to d, and the intersection with the energy axis at $E < 0$ equals $V_{ir}$. It has to be stressed that this analysis yields a value for d which has to be interpreted as an average interlayer spacing of the first few monolayers (Fig. 3.5) . This kinematic approach has been successfully applied to thin films of 3d transition metals and their alloy films like $NiMn/Cu_3Au(001)$

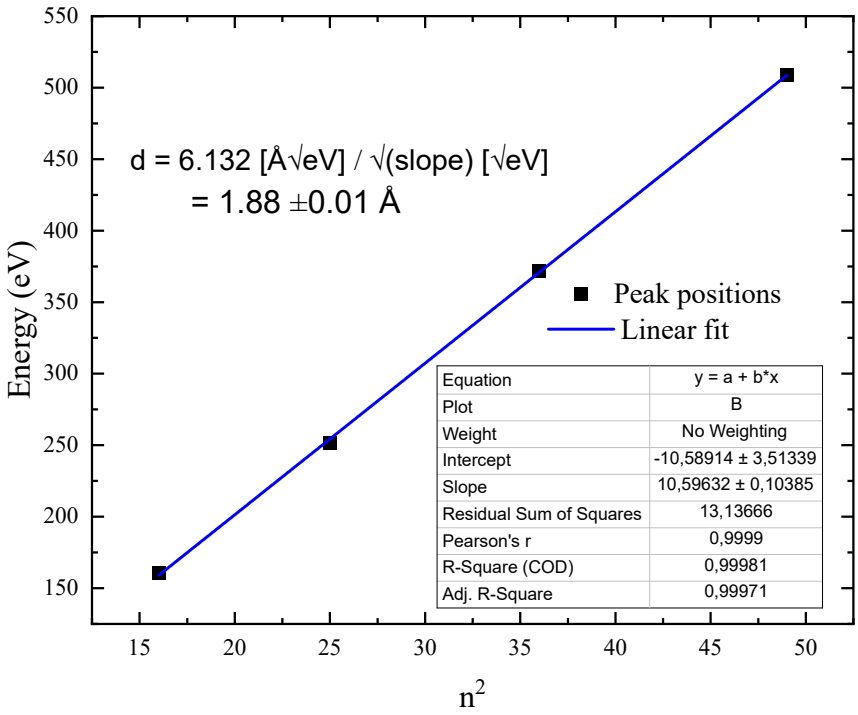


**Figure 3.6:** Electron beam energy dependence on $n^2$ for the LEED (0,0) spot of $Cu_3Au(001)$ substrate. The vertical interlayer distance d is extracted from the slope of the linear fit.

.

[71], $Mn/Cu_3Au(001)$ [137], $NiMn/Ni(/Co)/Cu_3Au(001)$ [73,138], Ni/Cu(001) [139], Fe/Cu(001) [140], FeMn/Cu(001) [141], to name only a few examples. The LEED I(V) curves presented in this work were obtained by recording the spot intensities on the fluorescent screen with a high-resolution CCD camera (EE2010).

### 3.2.3 Medium-energy electron diffraction

Medium-energy electron diffraction (MEED) was employed for monitoring and characterizing the film growth. The principle of this technique is similar to reflection high-energy electron diffraction (RHEED), which is the standard in-situ technique in molecular beam epitaxy for the growth of semiconductor films [142]. The principle of MEED is illustrated in Fig. 3.7. An electron beam of energy between 2–5 keV strikes the sample at grazing incidence. The interaction with a crystalline sample gives rise to a diffraction pattern that is monitored on a fluorescent screen opposite to the electron gun. In short, the changing diffraction properties of the surface during growth give rise to a variation of the intensity of the diffraction spots. The intensity depends on the interference conditions between electron waves scattered from a uniform

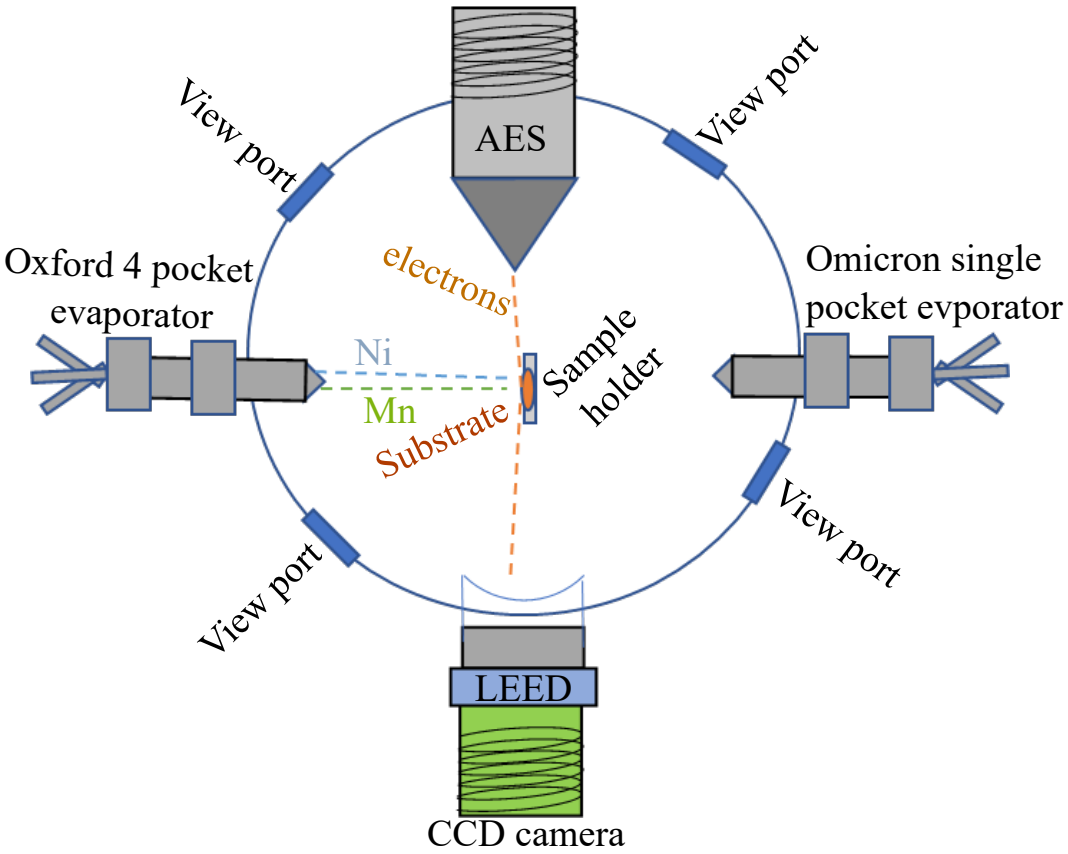


**Figure 3.7:** The electron gun of the AES system and the fluorescent screen of the LEED system are utilized for MEED. The orange dotted line indicates the electron trajectory.

.

surface and one which is populated by monolayer thick islands. In case of Frank-van-der-Merwe growth mode, intensities of the spots oscillate with a periodicity which matches the periodicity of the surface morphology during layer-wise growth. Although a phase shift between the intensity maxima and the completion of a full monolayer might be present, the oscillations are directly related to the number of deposited monolayers. Thus, the coverage of an adsorbate growing in layer-by-layer fashion can be readily determined by MEED. The thickness accuracy is typically in the range of a tenth of a monolayer. As an example, Fig. 3.8 shows the MEED intensity, i.e., the intensity of the (0 , 0) spot and that of the (1/2 , 1/2) spot, during the deposition of 15 ML $Ni_{33}Mn_{67}$ alloy film, at a rate of 2 minutes per monolayer on a $Cu_3Au(001)$ single crystal held at T = 300 K. The diffraction pattern of the pristine $Cu_3Au(001)$ is shown in the inset. The symmetry of the pattern proves that the substrate's [001] in-plane direction lies within the plane of incidence.

- **Composition and thickness of Ni in $Ni_xMn_{100-x}$**

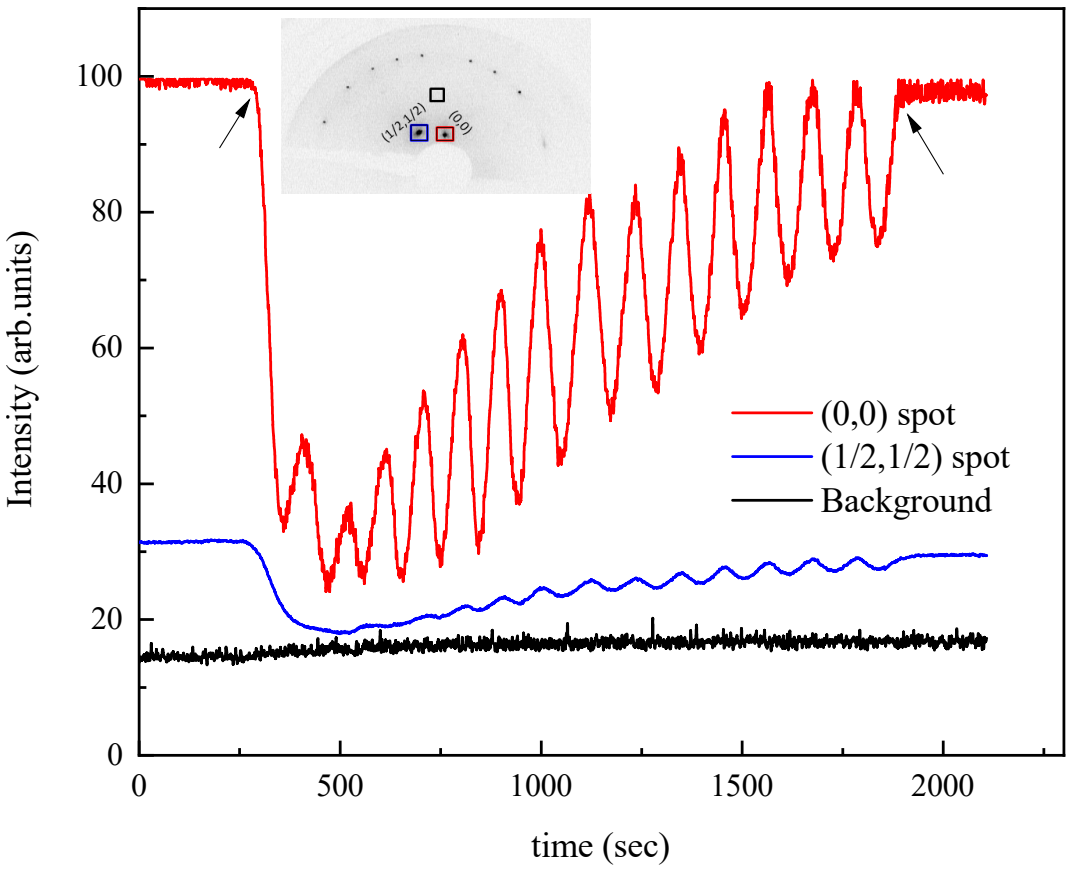


**Figure 3.8:** MEED intensity versus time during the growth of 15 ML of $Ni_{33}Mn_{67}$ alloy on $Cu_3Au(001)$ at room temperature. The inset shows the diffraction pattern of the pristine substrate in which the (0,0) spot is indicated in a red square while a blue square indicates the (1/2,1/2) spot. The pronounced intensity drop at the point where the evaporator's shutter was opened (indicated by an arrow on the left-hand side) marks the beginning of the growth. In the same way, the point at which intensity started to become constant where the evaporator's shutter was closed (indicated by an arrow on the right-hand side) marks the end of the growth. The presence of MEED oscillations indicates a layer-by-layer growth mode.

.

It is evident from the equidistant maxima and minima in Fig. 3.8, that the evaporation conditions in the Ni and Mn sources can be stabilized for a sufficiently long deposition time. Having a controllable and stable flux of materials are of utmost importance for the preparation of ordered or disordered alloy films with the desired composition employing individual or co-evaporation.

The previous section tried to convey the message that from the oscillations in the MEED intensity, it is possible to determine the evaporation rate of NiMn

($E_{NiMn}$) deposited on a substrate ($Cu_3Au(001)$) during the simultaneous co-evaporation of Ni and Mn. It also holds for the evaporation of only Ni or only Mn on to the substrate to determine their evaporation rates. In alloy formation or synthesis, one determine the rate of the second material if the first one is known already. For example, if Ni is evaporated at the same rate for the deposition of the Ni film and the $Ni_xMn_{100-x}$ film, one can compare $E_{Ni}$ and $E_{NiMn}$ as determined by MEED. In this way, one can already calculate the composition in the $Ni_xMn_{\ 100-x}$ film, since x is obtained by the ratio of $E_{Ni}$ and $E_{NiMn}$.

AES provides a complementary method to double-check the alloy concentration. In the general case of a film (F) growing on a substrate (S) in a layer-by-layer mode, the Auger intensities of the substrate and the film of thickness $d_F$ can be written as

$$I_S = I_0 * S_S * exp^{-d_F/\Lambda_S} \tag{3.2}$$

$$I_F = I_0 * S_F * (1 - exp^{-d_F/\Lambda_F}) \tag{3.3}$$

respectively, with the approximation that the attenuation of the Auger electrons within a material is determined by the mean distance the electrons can travel before an inelastic scattering event occurs. The subscripts S and F denote the substrate and the film, respectively. The quantities $S_i$ (i = S, F) are the sensitivities of the Auger transition. The effective attenuation lengths $\Lambda_i = \lambda_i / \cos\alpha$ are correlated to the attenuation length $\lambda_i$ of the Auger electrons from the materials i via the detection angle $\alpha$ of the Auger electron spectrometer. Finally, $I_0$ represents the intensity of the primary beam. From an Auger spectrum, one can measure $I_S$ and $I_F$ and determine the thickness of the film once the parameters $S_i$ and $\lambda_i$ are known. In the case of a binary alloy, the situation is more complicated, since now both the constituents of the alloy reduce the Auger signal from the substrate. Sometime an additional complication arises from the energetic overlapping of some of the prominent peaks of the different materials. In Fig. 3.9 an Auger spectrum of a 9 ML $Ni_{50}Mn_{50}$ film grown on $Cu_3Au(001)$ is shown. MEED determined thickness and concentration. As one can see, from each of the three materials, i.e., Mn, Ni, and Cu, there is at least one Auger peak not overlapping with others (though in Mn case we have 3 choices 545, 592, and 638 eV). We used 592 eV peak for Mn, 716 for the Ni and 920 for the Cu. The corresponding Auger electron intensities are defined as $I_{Mn}$, $I_{Ni}$, and $I_{Cu}$. Experimentally one can, therefore, obtain the ratio between the Cu and Mn (Ni) Auger intensities as $R_{Mn} = I_{Cu}/I_{Mn}$ ($R_{Ni} = I_{Cu}/I_{Ni}$) as a function of the thickness and the concentration of the alloy film.

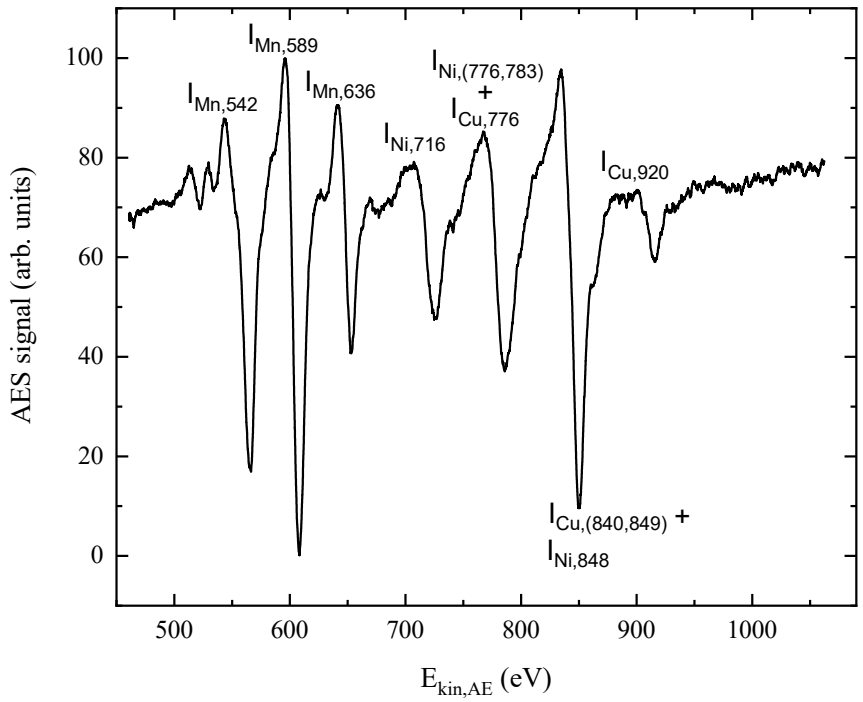


**Figure 3.9:** Auger spectrum from 9 ML $Ni_{50}Mn_{50}$ film grown on $Cu_3Au(001)$ at T=300 K. The number in the subscript along with the element name represents the relevant AES peak energy in electron volts (eV).

.

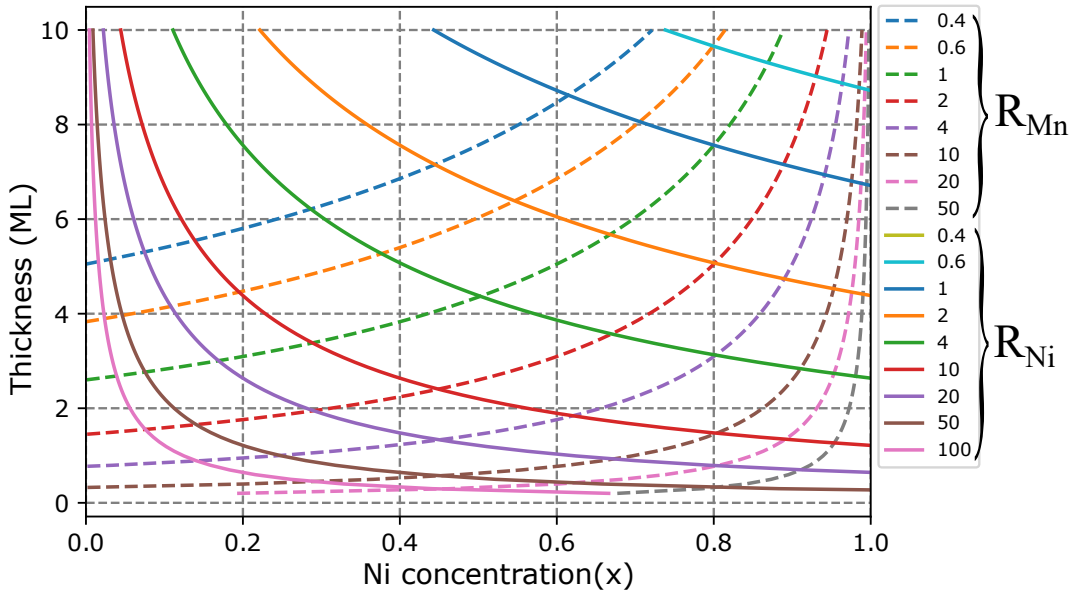


**Figure 3.10:** The use of Eq. 3.4 (rising lines), and Eq. 3.5 (falling lines) for different values of $R_{Mn}$ and $R_{Ni}$.

.

In the case of $Ni_xMn_{100-x}$ growing on $Cu_3Au(001)$, the ratio between equations 3.2 and 3.3 can be written for Mn and Ni, respectively, as

$$R_{Mn} = \frac{S_{Cu} * exp^{-d/\Lambda_{Cu}}}{S_{Mn} * (1-x) * (1 - exp^{-d/\Lambda_{Mn}})} \tag{3.4}$$

$$R_{Ni} = \frac{S_{Cu} * exp^{-d/\Lambda_{Cu}}}{S_{Ni} * x * (1 - exp^{-d/\Lambda_{Ni}})} \tag{3.5}$$

where now d is the total film thickness and x, the Ni concentration. To determine d and x from equations 3.4 and 3.5, the quantities $S_i$ (i = Mn, Ni, and Cu) and $\Lambda_i$ are needed and are taken from the work of Ref. [143]. Normally, these can be obtained by graphically adjusting the theoretical curves 3.4 and 3.5 in a way to match the experimental values of $R_{Mn}$ and $R_{Ni}$, whose corresponding thickness and concentration should be determined beforehand from MEED oscillations. The result of this procedure is shown in Fig. 3.10. For each point, an observed value of $R_{Mn}$ and $R_{Ni}$, as measured by AES, is given. Of course, for pure Mn (Ni), just the parameter $R_{Mn}$ ($R_{Ni}$) is measured. Therefore, "using equations 3.4 and 3.5, the values of thickness (d) and Ni concentration (x) can be determined. In a plot of d versus x, the solution of these two equations form lines that are monotonically rising (3.4) or falling (3.5), as shown in Fig. 3.10. The crossing of these two lines for $R_{Ni}$ and $R_{Mn}$ yields d and x. For NiMn films of thickness smaller than 15 ML and grown on $Cu_3Au(001)$" [143], Auger is quite useful to calculate the thickness and concentration in this way with an error of 0.5 ML thickness and 4% concentration.

### 3.2.4 Scanning tunneling microscopy (STM)

STM is a technique that allows imaging a conducting surface and its local electronic structure at the atomic scale. It was developed in 1981 by two IBM scientists, Gerd Binnig and Heinrich Rohrer, and because of this milestone invention, they won the Nobel Prize in 1986.

#### Principles of Scanning Tunneling Microscopy

An STM uses "a sharp needle, referred to as 'tip,' to scan the topography of the surface without touching it. A sketch for the primary mechanism of an STM setup is shown in Fig. 3.11. A voltage is applied between the metallic tip and the conducting sample within a distance of few Å. The STM operates in the regime of minimal distances between the tip and the surface of only 0.5 to 1.0 nm, i.e., 2 to 4 atomic diameters. Within these small distances, by applying

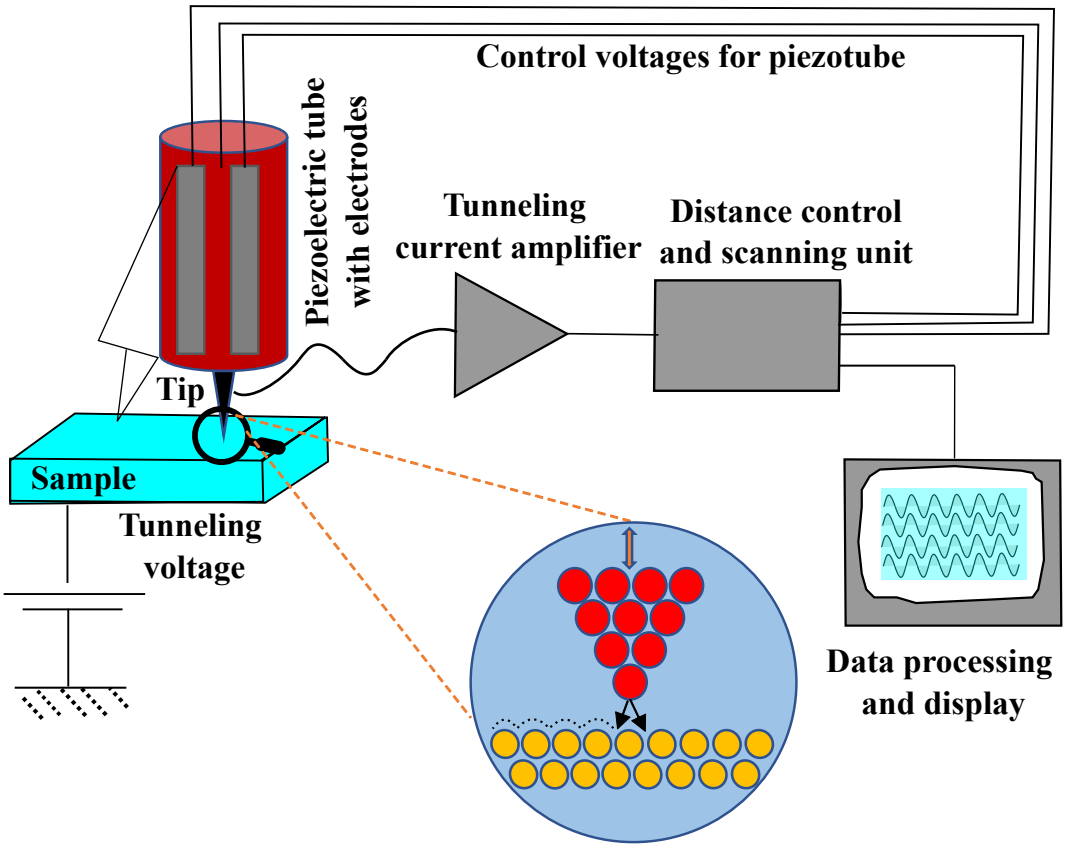


**Figure 3.11:** A sketch of the operating mechanism of STM. A small bias voltage is applied between the tip and the sample. Inside the circle, a tunneling process between the tip apex and the sample surface is sketched. Image was re-drawn and modified following [144].

.

an external electric field, the electrons can tunnel from the tip to the surface or vice versa across the vacuum barrier, hence the name of this microscope–tunneling microscope. At positive bias voltages, electrons tunnel from tip to sample, and vice versa for negative voltages. The surface topography can be measured by combining the tip with a piezoelectric drive system and a feedback loop. STM can be a challenging technique, as it requires clean and stable surfaces, sharp tips, excellent vibration control, and sophisticated electronics.

A simple schematic of the STM chamber (Omicron) is shown in Fig. 3.12. It consists of two main portions: the preparation chamber and the STM chamber, separated by a gate valve. The sample can be prepared in the preparation chamber using two separate four-pocket evaporators filled with the Ni, Mn, Co, etc., where co-evaporation is also possible. After preparation, the sample is then transferred to the STM chamber with the help of a wobble stick to a transfer rod, then from the transfer rod to the STM stage by another wobble

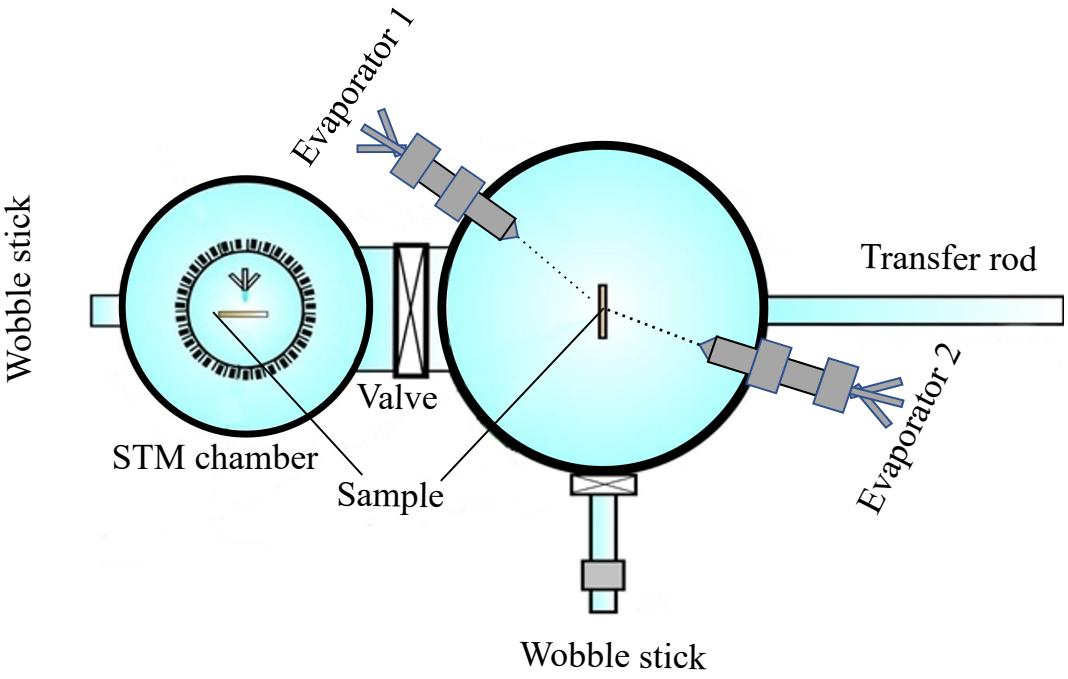


**Figure 3.12:** Sketch of the top cross section view of the STM chamber.

.

stick shown in Fig. 3.12. The STM stage is suspended by four springs and magnetically damped in vacuum during the measurement to reduce noise while scanning. The turbo pump is also switched off for the same purpose. An ultra-high vacuum with a pressure of lower than $9\times10^{-10}$ mbar can be maintained with the help of ion-getter pumps in both parts of the chambers" [138].

Fig. 3.13 (a) shows an STM image of pristine $Cu_3Au(001)$. Fig. 3.13 (b) shows a line profile taken along the solid line in image Fig. 3.13 (a). This topographic image of the $Cu_3Au(001)$ substrate is obtained using an Fe ring. The tip was prepared from Fe wire by an electrochemical etching method. The line scan profile in Fig. 3.13 (b) shows the presence of monolayer steps.

**Advantages of STM Compared with Other Techniques;**

Each of the techniques introduced earlier has particular strengths and limitations. For example, LEED relies on large-scale order and can at best give average information about local and defect structure. The higher vertical resolution of STM relative to other microscopes also offers advantages concerning a qualitative analysis of surface roughness on a nanometer scale. The other unique feature of the STM is it's genuinely local interaction on the atomic scale rather than the averaged properties of the bulk phase or of a large sur-

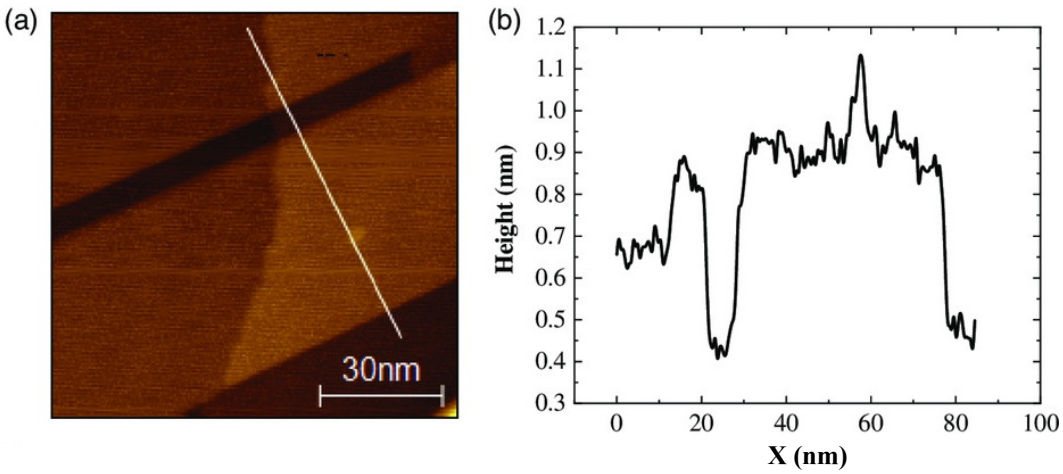


**Figure 3.13:** Constant-current STM topography image (U = 1 V, I = 0.48 nA): (a) pristine $Cu_3Au(001)$ substrate. (b) Line profile along the white line in image (a).

.

face area, which allows the study of individual surface defects, and surface reconstructions at unprecedented resolution.

### 3.2.5 Magneto-optical Kerr effect

The magneto-optical Kerr effect (MOKE) was exploited for measuring magnetic hysteresis loops. The effect was discovered by J. Kerr in 1877 and was first adapted for studies in the field of surface magnetism in the late 1985 by Moog and Bader [145]. A modern review can be found in reference [146]. The magneto-optical Kerr effect "relies on the response of optical properties on the magnetic state of a sample. The magneto-optical interaction causes a polarization change upon reflection of polarized light from a magnetic surface. The reflection of linearly polarized light impinging on the sample leads to a rotation of the polarization axis and to the appearance of a small fraction of elliptically polarized light in the reflected beam. The former effect is quantified by the so-called Kerr angle and the latter by the Kerr ellipticity. Both quantities are proportional to the magnetization within the probing volume but do also depend on wavelength and material. The probing depth is given by the penetration depth of light, which is of the order of a few hundred Å.

There exist different MOKE geometries, depending on the orientation of the magnetization vector M relative to the incidence plane. In the polar geometry, as illustrated in Fig. 3.2, the polarized light beam hits the surface close to normal incidence. This geometry is sensitive to an out-of-plane magnetization. In the longitudinal geometry Fig. 3.2, the magnetization lies within the

surface plane and also within the plane of incidence" [138]. And in the transverse geometry (not shown), the magnetization lies within the surface plane but orthogonal to the plane of incidence.

### UHV-compatible MOKE setup

In this work a MOKE system was set up that is based on a polarization modulation technique. A scheme is sketched in Fig. 3.2. "An intensity stabilized 5 mW laser diode emitting partially polarized light at a wavelength of $\lambda = 632$ nm acts as a light source. The key element of this setup is a photo elastic modulator which consists of a transparent piezo-driven birefringent crystal. The modulation axis is set to 45° relative to the polarizer. The electric field component of the light pointing along the modulation axis receives a periodic retardation at the modulation frequency f (50 kHz) with an amplitude of $\lambda/4$. Thus, the polarization state of the modulated light is changed periodically according to the following sequence: linear, right-circular, linear and left-circular, whereas it is elliptically polarized in between. The linear component experiences a Kerr rotation upon reflection by the sample. Eventually, the reflected light passes an analyzer and a 632 nm interference filter before being detected by a photodiode. The pre-amplified output signal from the photodiode as well as a reference signal from the modulator are fed into a lock-in amplifier. It can be shown that the Kerr rotation yields an AC signal at twice the modulation frequency [147]. This 2f signal is recorded and normalized to the DC-signal, while computer-controlled two bipolar power supplies sweep the current of the magnet coils. Those two coils provide a maximum field of about 150 mT at the sample position. The illustration in Fig. 3.2 shows the layout for the polar geometry. The longitudinal geometry was achieved by a setup where the light from a second laser diode was used. In this case the sample normal is oriented perpendicular to the magnetic field " [138]. The same analyzer and photo-diode are used for both MOKE geometries.

# 4

# Bulk and interfacial effects in $Co/Ni_xMn_{100-x}$ exchange bias system due to creation of defects by $Ar^+$ sputtering

## 4.1 Growth and structure of $Ni_xMn_{100-x}$ on $Cu_3$-Au(001) and Co on $Ni_xMn_{100-x}$.

In this work [1] the detailed mechanism leading to EB in single-crystalline thin film systems with NiMn binary alloys and Mn as the antiferromagnetic layers and Co as FM layer is investigated. The approach is to influence both the interface coupling between an FM and an AFM material as well as the pinning sites inside the AFM material by the controlled insertion of disorder at defined depths of the layered system. This is achieved via deliberately sputtering by $Ar^+$ either at the surface of the AFM layer or at a certain depth between two deposition steps. To create defects inside the AFM layer, we stopped the deposition shortly to expose the surface for 40 seconds to Ar ions of 1 keV energy, using an Ar pressure of 2 $\times 10^{-5}$ mbar. These exposure conditions have been optimized in a way not to lose any measurable part of a monolayer, as detected by Auger electron spectroscopy (AES). By placing a mechanical shutter in front of the substrate, this can be applied to one half of the sample, while the other is unaffected. Comparison of the magnetic properties measured at the two parts of the sample then allows a precise determination of the influence of the additional step during the sample preparation, since all other parameters such as film thicknesses and precise composition of the alloy are identical. The influence of this disorder on the EB is then monitored as a function of the position of this defect layer. If disorder within the AFM layer

[1] This chapter contains parts from Ref. [148], published in Physica Status Solidi Rapid Research Letters."

plays a role in the pinning, a clear influence on the EB effect should be observed by comparing the two sides, defected and undefected, of the sample. This would help to verify or falsify different models of EB discussed in chapter 2. The antiferromagnetic systems under study are $Ni_xMn_{100-x}$ including pure Mn on $Cu_3Au(001)$.

## 4.2 Results

The growth of AFM $Ni_xMn_{100-x}$ on $Cu_3Au(001)$ at T=300 K was monitored by means of MEED for the concentration range from pure Mn to equiatomic NiMn.

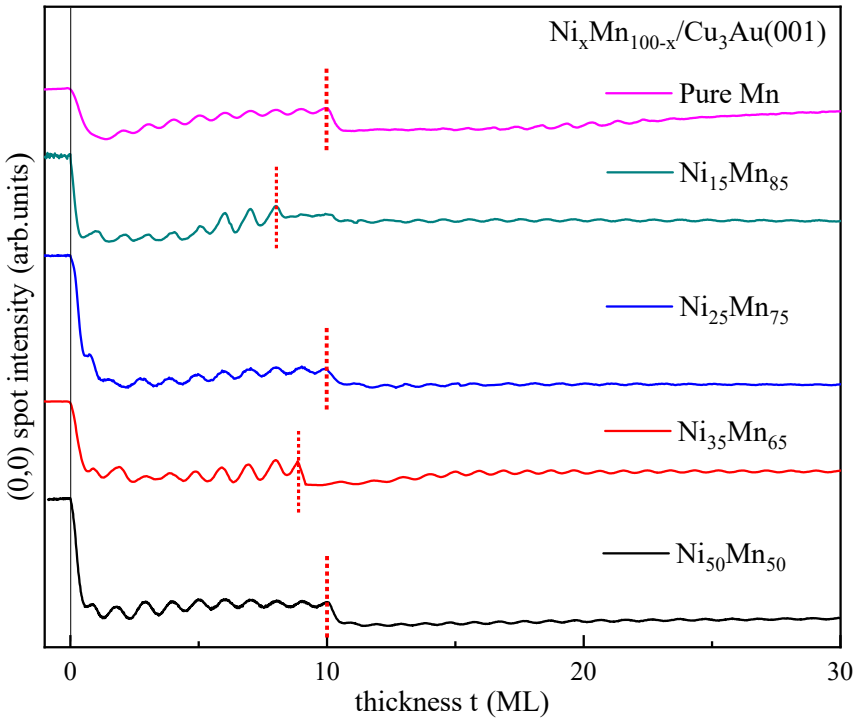


**Figure 4.1:** MEED curves of the (0 0) spot recorded during the deposition of $Ni_xMn_{100-x}$ films on $Cu_3Au(001)$ at 300 K for various values of x. All $Ni_xMn_{100-x}$ samples are 30 monolayers thick and on top 5 monolayers cobalt are deposited. The red vertical dashed bars represent the thickness at which one sample was sputtered or sandwiched defects are introduced. The shutter was opened at 0 ML and closed at the dashed bars, then after creating defects it was opened at the dashed bars and closed at the end, i.e, at 30 ML.

Figure 4.1 shows the reflected MEED intensity as a function of deposition time for increasing Ni content (x) from top to bottom. The curves are normal-

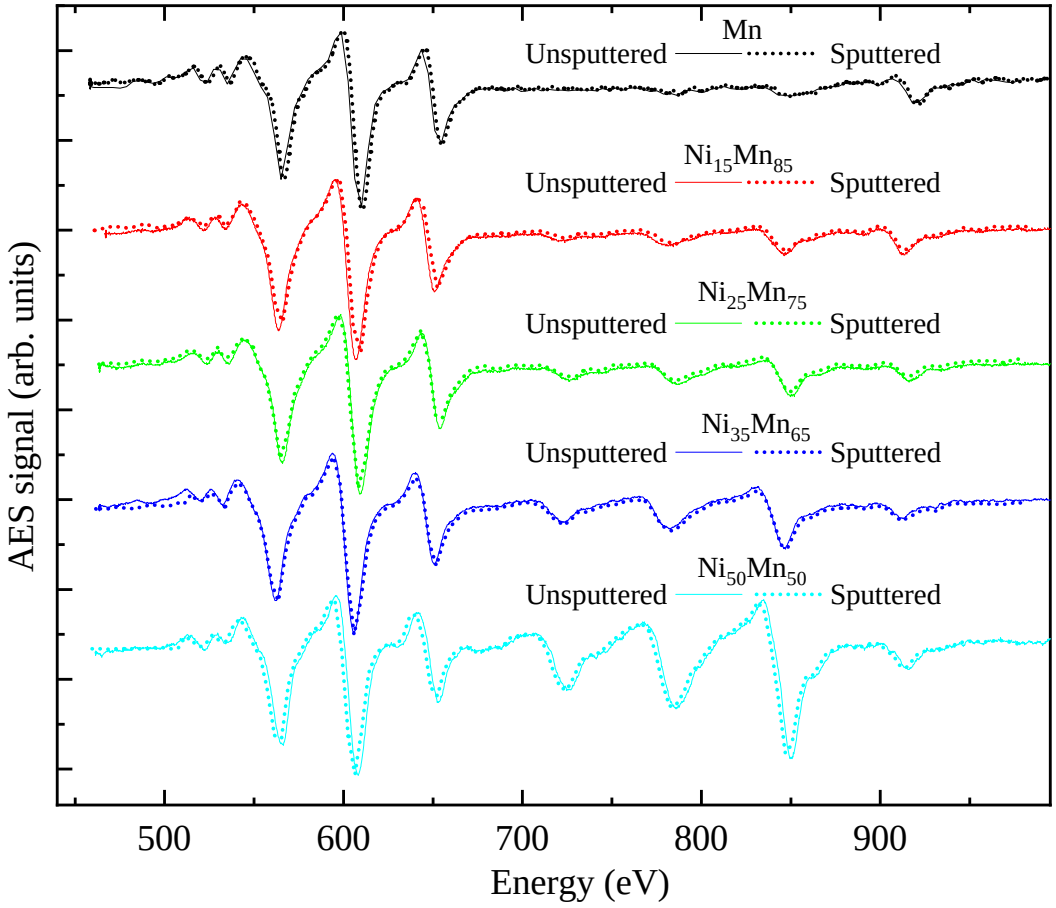


**Figure 4.2:** Normalized AES spectra of unsputtered and sputtered (dotted lines) part of the samples for different concentrations of Ni in the $Ni_xMn_{100-x}$ alloy. All samples are ~ 8-10 ML's thick. AES spectra for both unsputtered and sputtered parts of the sample, approximately look the same and roughly gives the same Ni concentration, too.

ized to the initial MEED intensity at the time before opening the shutters, i.e., at t=0 ML, and shifted vertically for clarity. The deposition time was converted into a monolayer thickness scale under the assumption that a maximum in the MEED intensity corresponds to a filled integer monolayer, neglecting a possible phase shift. This conversion allows a convenient presentation of MEED curves obtained from films deposited at different growth rates in a single figure. An oscillating MEED intensity, which is a fingerprint of a layer-by-layer growth mode, was found for all $Ni_xMn_{100-x}$ films, including x=0. The MEED oscillations of the NiMn alloy on $Cu_3Au(001)$ exhibit improved layer-by-layer growth in comparison to NiMn alloy on Cu(001), which only shows fifteen pronounced maxima [86]. The reason may lie in the differences in lattice mismatch with the different substrates. NiMn has less mismatch with $Cu_3Au(001)$ in comparison to Cu(001) substrate. The growth axis of NiMn alloy on both

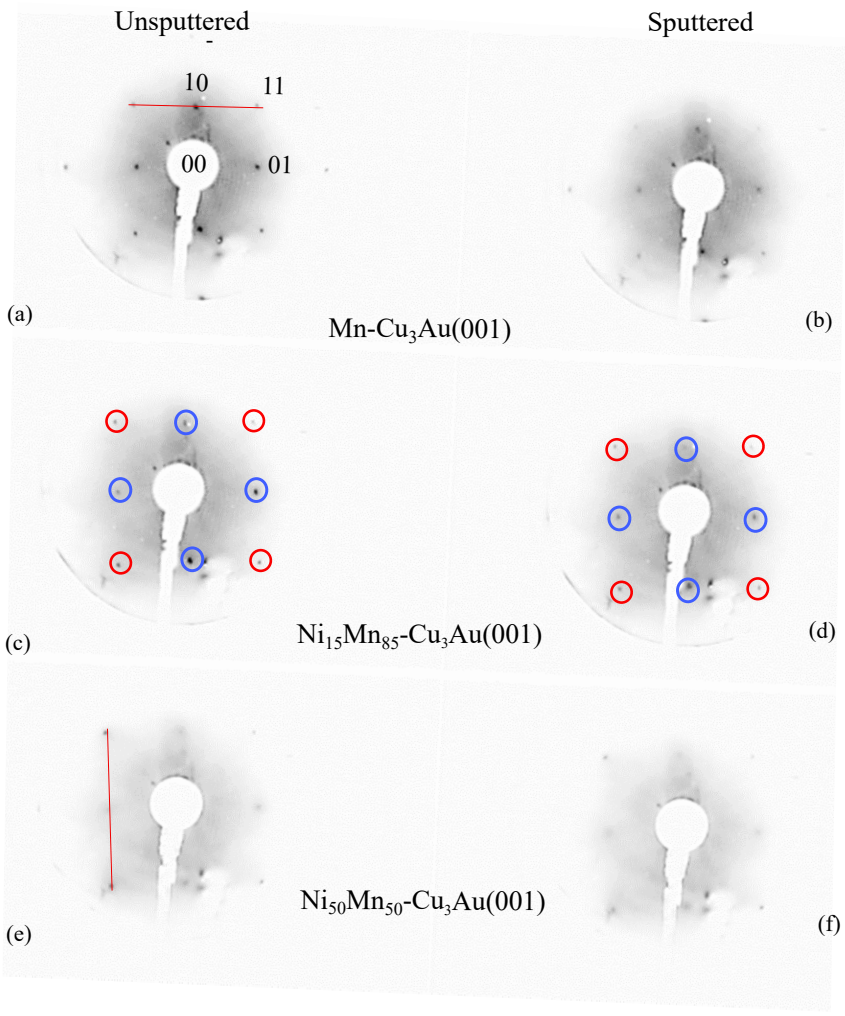


**Figure 4.3:** LEED patterns of ~10 monolayers thick $Ni_xMn_{100-x}$ films grown on $Cu_3Au(001)$ at T=300 K: unsputtered and sputtered (a,b) Mn (c,d) $Ni_{15}Mn_{85}$ and (e,f) $Ni_{50}Mn_{50}$. The spot positions are highlighted in (c) and (d) which show c(2×2) structure, not to be confused with artifacts in the LEED system we used. (a) and (e) show how the line profile analysis is perfomed using a line through three spots, in a similar way for both sputtered and unsputtered part of the samples.

substrates also shows differences [70, 86, 87, 138, 148]. The stronger reduction in the amplitude of oscillation indicates the onset of simultaneous growth of several layers, which is named three-dimensional growth mode. Oscillation amplitude is reduced after sputtering.

Figure 4.2 shows the spectra of the unsputtered and sputtered parts of the sample for five samples of different concentrations. As stated above, the film thickness is calibrated by means of oscillations in the MEED intensity

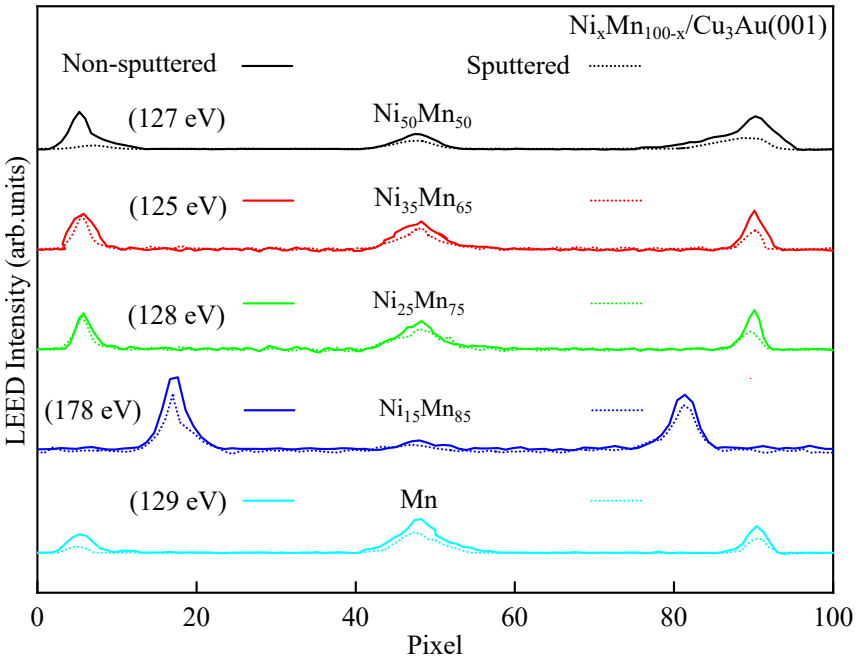


**Figure 4.4:** Intensity profiles (line scans) from the LEED patterns for $Ni_xMn_{100-x}$ films on $Cu_3Au(001)$. The dotted and straight lines for each sample show the comparison of the sputtered and the unsputtered part of the same samples. Equal values of electron energy (mentioned to the left side of each line scans) are considered for the same sample and nearly equal values for all samples except for $Ni_{15}Mn_{85}$, where higher energies are required to see the difference between both parts of the sample.

recorded during evaporation but afterward also crosschecked by AES. AES helps in finding out the precise composition i.e., the Ni concentration in the $Ni_xMn_{100-x}$ alloy; it also helps to check the aspect of erasing or varying the Ni concentration after exposing one part of the sample for a short time of 40 seconds to the Ar ions.

Figure 4.3 shows the LEED patterns of $Ni_xMn_{100-x}$ films on $Cu_3Au(001)$ at 300 K. Since the main purpose of the present study is the comparison of the magnetic properties of the sputtered and unsputtered parts of the same sample, it is important to show that the crystalline structure of both parts is very similar. LEED was performed directly after sputtering one part of the sample. As $Cu_3Au(001)$ has *fcc* structure, the LEED pattern shows the surface of a *bcc* structure. The only difference the LEED patterns show is that producing controlled defects leads to a slight change in the intensity, as is clear from Fig. 4.3 and is further supported by Fig. 4.4, which shows the line scans for these LEED patterns. So, for nearly the same electron energies of ~125 eV,

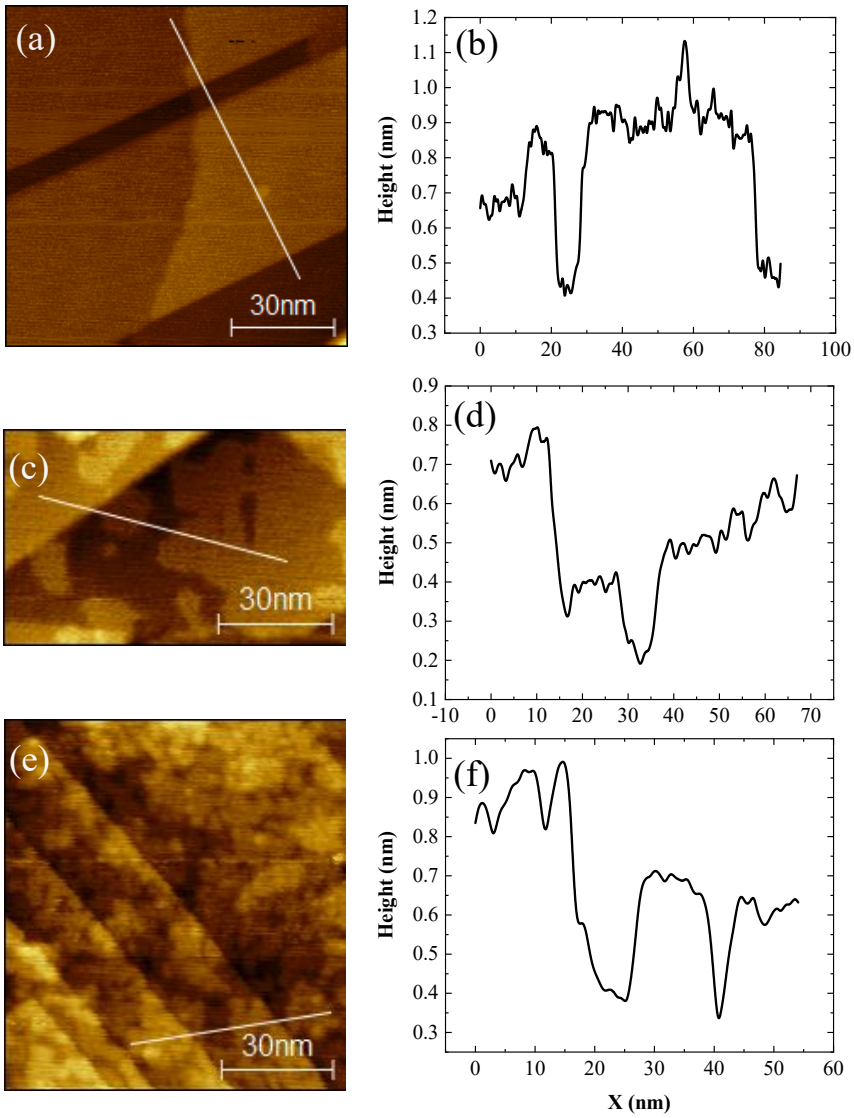


**Figure 4.5:** (a, c, e) Constant-current STM topography images (U = 1 V, I = 0.48 nA): (a) pristine $Cu_3Au(001)$ substrate, (c) room-temperature deposited nonsputtered, and (e) sputtered 4 ML Mn on $Cu_3Au(001)$. (b, d, f) Line profiles along the white lines in images (a, c, e), repectively.

.

the structure of both parts of the sample is taken in form of LEED images and compared side by side. A clear difference is observed for each sample. This suggests that after producing defects the surface becomes a bit rough, and the spots show less intensity as compared to the unsputtered part.

This is due to the roughness of the surface at the sputtered part, which is caused by the induced defects. The consistent peak positions with respect to the substrate, indicate the coherent growth throughout the investigated

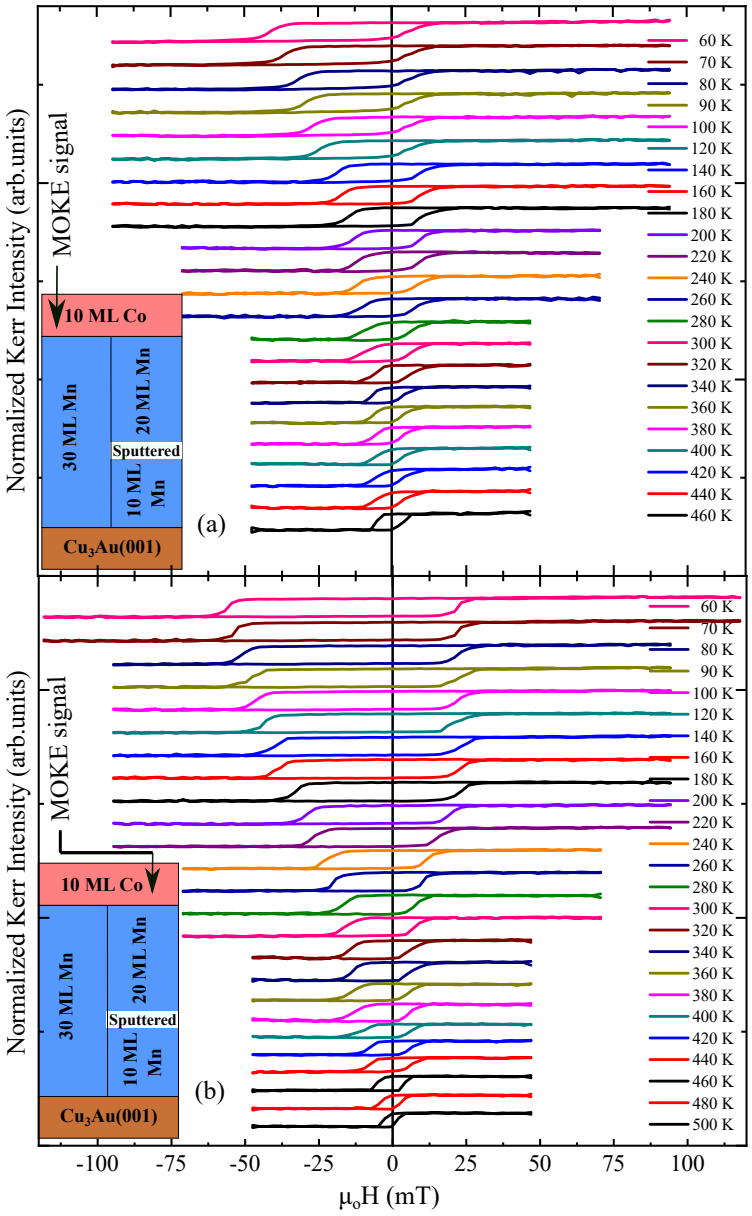


**Figure 4.6:** Normalized hysteresis loops for the sample of 10 ML Co/ 30 ML Mn/ $Cu_3Au(001)$ for the (a) unsputtered and (b) sputtered part of the sample, measured with longitudinal MOKE at different temperatures. The inset (sketches) show the two parts of the same sample, unsputtered and sputtered, respectively.

thickness of ~10 ML region. The unsputtered part of $Ni_xMn_{100-x}$ films exhibits sharp LEED spots and a high ratio of peak intensity to background depicted in Fig. 4.4. In contrast, the sputtered part of the $Ni_xMn_{100-x}$ films exhibits a bit dimmer spots in which the peak intensity decreases.

Figure 4.5 (a) shows STM images of pristine $Cu_3Au(001)$, (c) nonsputtered

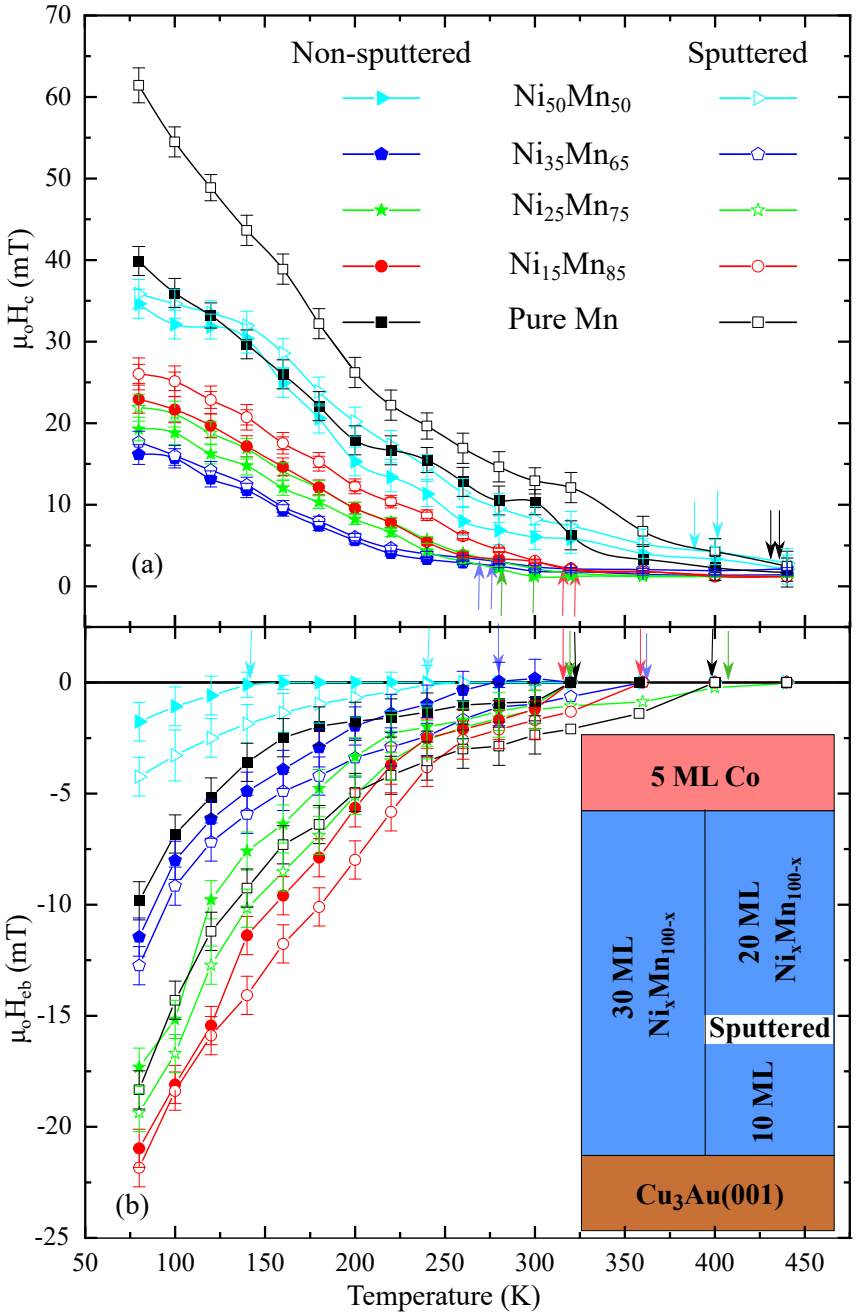


**Figure 4.7:** Temperature dependence of $H_c$ (a) and $H_{eb}$ (b) for equal thicknesses of ~30 ML $Ni_xMn_{100-x}$ in 5 ML Co/~30 ML $Ni_xMn_{100-x}$ bilayers on $Cu_3Au(001)$. The sketch in the inset shows how defects are introduced at nearly same depth of ~10 ML in one part of each sample.

4 ML $Mn/Cu_3Au(001)$, and (e) sputtered 4 ML/$Cu_3Au(001)$ films. Figure 4.5 (b, d, f) show line profiles taken along the solid lines in images Fig. 4.5 (a, c, e), rspectively. Figure 4.5 (c, e), shows Mn films with atomically flat surfaces

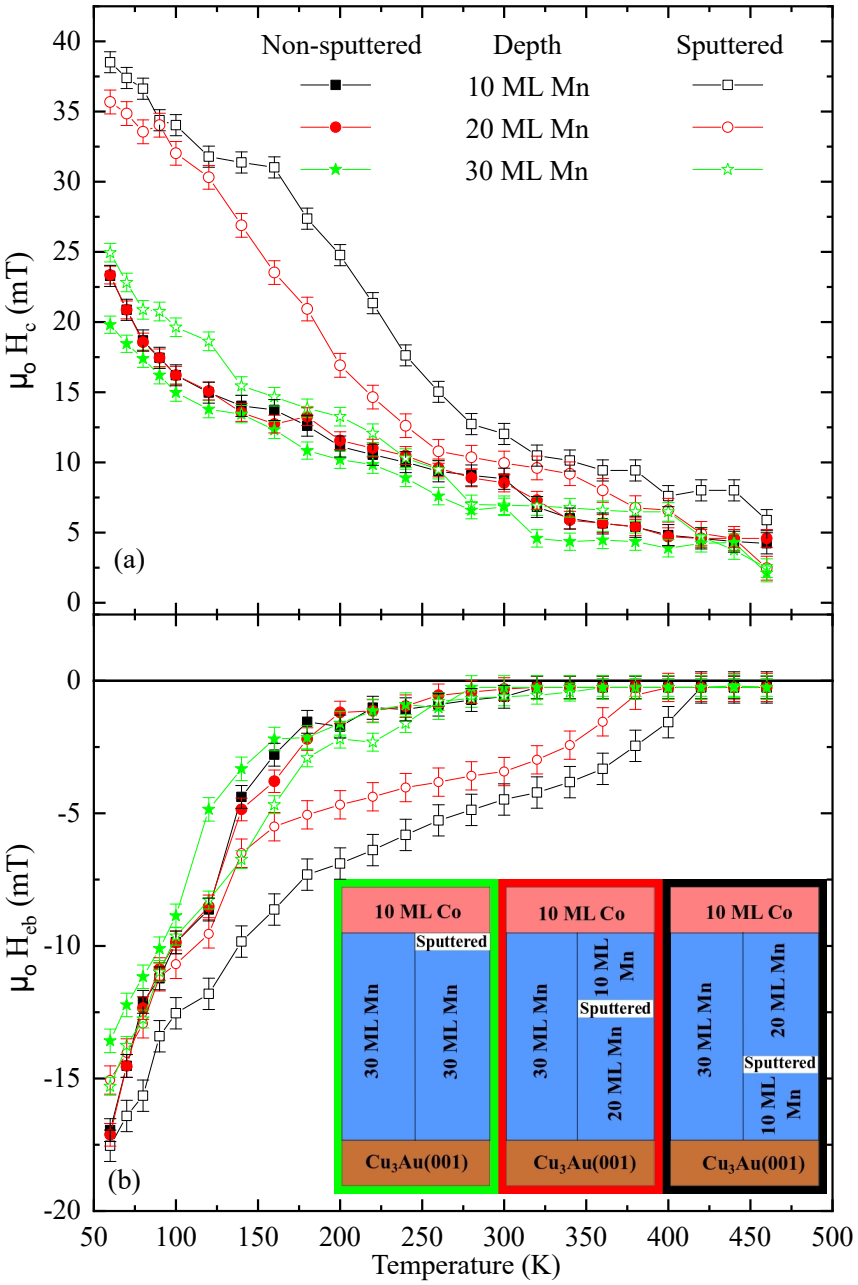


**Figure 4.8:** Temperature dependence of $H_c$ (a) and $H_{eb}$ (b) for equal thicknesses of ~30 ML of Mn in 10 ML Co/~30 ML Mn bilayers for both parts (sputtered and unsputtered) of the samples on $Cu_3Au(001)$. The inset (sketch) shows how defects are inserted at different depths in one part of all three samples. The frame color of each box in the inset corresponds to the respectively colored data points in the main figure. The filled symbols are for the unsputtered parts and the open symbols for the sputtered parts of the samples.

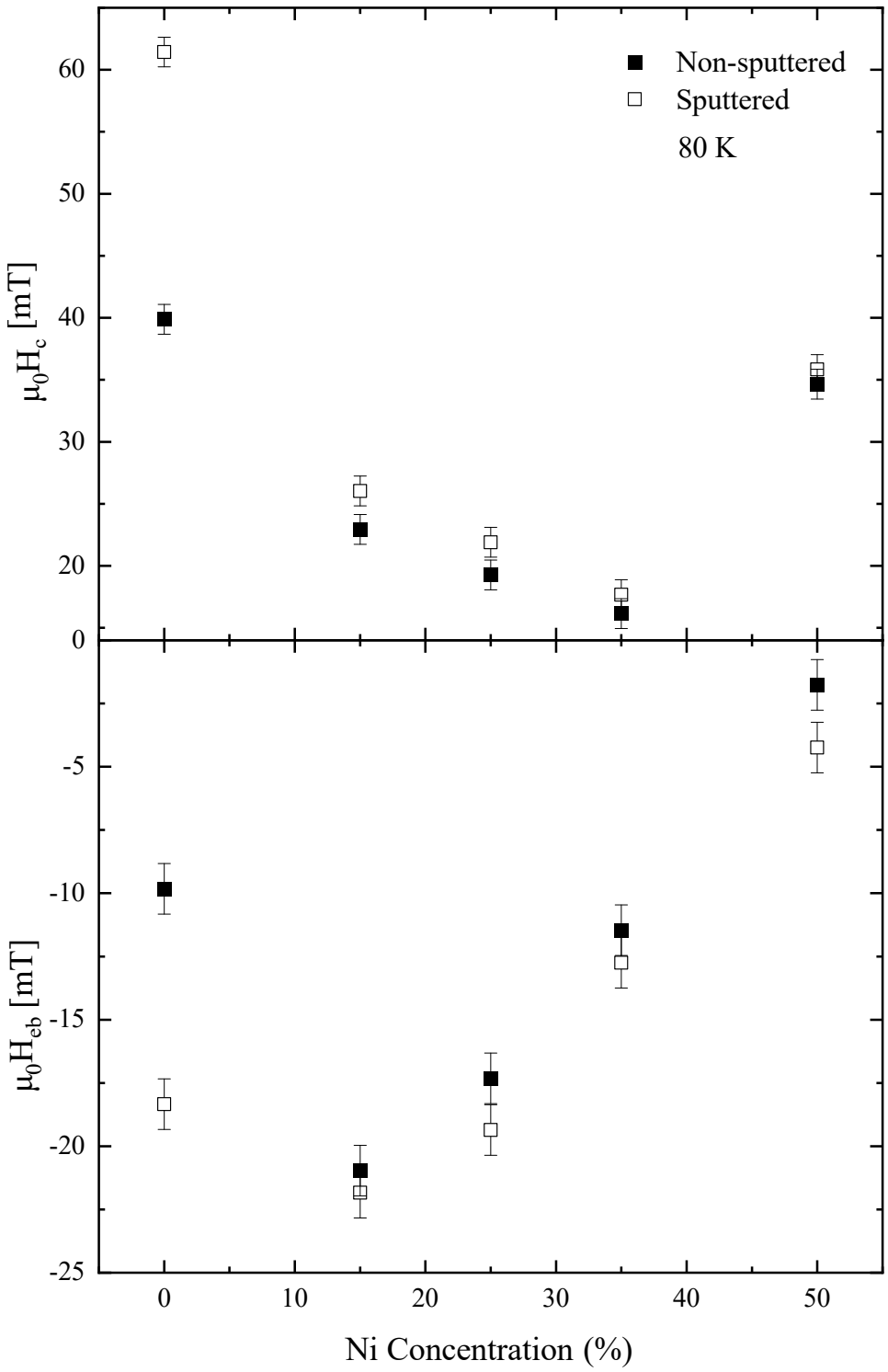


**Figure 4.9:** Ni concentration-dependent $H_c$ and EB field in $Ni_xMn_{100-x}$ alloys at 80 K for equal thicknesses of samples ~30 ML in 5 ML Co/30 ML $Ni_xMn_{100-x}$ bilayers on $Cu_3Au(001)$.

.

with small 2D islands of single atomic height on top, which have feature sizes of several nanometers. This observation is consistent with the layer-by-layer growth concluded from the MEED oscillations. Furthermore, a clear well-ordered surface is observed for the nonsputtered 4 ML Mn film, whereas a somewhat enhanced roughness can be seen on the surface of sputtered 4 ML Mn/$Cu_3$Au(001). These results are in accordance with Fig. 4.3 and 4.4. The separation between Mn atomic planes is obtained from the line scans.

Hysteresis loops are measured with longitudinal MOKE at different temperatures after field cooling with +2 mT from above the Néel temperature ($T_N$) of Mn and below the Curie temperature ($T_C$) of the Co layer i.e., ~480 K, which provided an EB shift along the negative field direction. Figure 4.6 shows an example of temperature-dependent hysteresis loops for IP magnetization of Co/$Ni_xMn_{100-x}$ bilayers. Here the sample is 10 ML Co/30 ML Mn/$Cu_3$Au(001) in Fig. 4.6 (a) and 10 ML Co/20 ML Mn/sputtered/10 ML Mn/$Cu_3$Au(001) in Fig. 4.6 (b).

Nearly rectangular-shaped loops for both cases are obtained, where a coercivity ($H_c$) enhancement with decreasing temperature can be observed and an exchange bias. Although the general behavior of the temperature-dependent hysteresis loops is similar for the unsputtered and sputtered cases, the details are different (Fig. 4.6). The main differences are (i) the $H_c$(T) for the sputtered part is almost 1.5 times that for the unsputtered part at low temperatures, and the reduction of $H_c$ to lower values occurs at higher temperatures for the sputtered part. (ii) the EB field ($H_{eb}$) for the sputtered part is vanishing at ~420 K, while it ceases for the unsputtered part below ~260 K, which means the blocking temperature is nearly doubled. In these kind of magnetic thin films, $H_c$ of the FM alone typically decreases about linearly with increasing temperature. A linear decrease of $H_c$ could thus just be due to the absence of exchange coupling between the AFM and the FM layer. In contrast, we observe a discontinuity in the slope of $H_c$ versus temperature, which is typical for exchanged-coupled/FM bilayer systems [91, 149, 150]. The point at which this discontinuity of the temperature-dependent $H_c$ occurs is considered as $T_N$. For its estimation, we follow the procedure already used in [149] and fit a straight line to the high-temperature side of the $H_c$(T) data to represent the behavior of the uncoupled FM layer. The temperature at which the measured $H_c$ significantly diverges from this line is defined as Néel temperature $T_N$ of the AFM layer. The error in this method is less than ± 10 K. To avoid an alloying effect of the AFM and FM materials at the interface, we did not take measurements above 500 K.

Figure 4.7 shows the temperature-dependent evaluation of $H_c$ (a) and $H_{eb}$

field (b) for samples with different concentrations x but similar thickness ~30 ML $Ni_xMn_{100-x}$, either sputtered after ~10 ML or unsputtered, in contact with in-plane magnetized FM Co. Generally, it is reported that EB starts near the peak of $H_c$ [96,121], which holds true for the pure Mn samples, but this is not the case all the time. For example, Maat *et al.*, found that $T_b$ occurs very close to $T_N$ without any $H_c$ peak down to the minimum temperature of 10 K [151]. From Fig. 4.6 (a) we can see that there is a considerable change in $H_c$ of all the samples and within the same sample too, i.e., between the sputtered and the unsputtered part of same samples, especially at lower temperatures. In case of pure Mn, the difference between he coercivity of sputtered and unsputtered is very big.

In Fig. 4.6 (b) same scenario again, a very big difference is seen in $H_{eb}$ for sputtered and unsputtered part of pure Mn and also a considerable change in sputtered and unsputtered parts of other four samples. For four samples (without pure Mn), there is a well defined trend: with decreasing x, $T_b$ shifts to higher temperatures, in both parts of each sample, interestingly. At lower temperatures especially, the difference in $H_{eb}$ is very clear between both parts of each sample and also among unsputtered parts of different samples. Similar results have been presented in Ref. [70, 73] for unsputtered bilayers NiMn/Ni/(Co)/$Cu_3$Au(001). The difference here is that while for IP magnetization in Ref. [70,73], Khan *et al.*, used 2 ML Co first on $Cu_3$Au(001) and the Ni is evporated on top of it before NiMn as an AFM has been deposited. We deposited directly NiMn on the $Cu_3$Au(001) crystal, introduced some defects within or on the surface of NiMn by Argon sputtering, and then introduced FM Co on top.

Comparing the sputtered samples to the unsputtered ones, higher values of $H_c$, $H_{eb}$ and $T_b$ are observed in the sputtered system.

Figure 4.8 depicts $H_c$(T) and $H_{eb}$(T) for three samples of pure Mn with equal thicknesses. Here defects are produced at different depths in the AFM Mn (from bottom to surface). The unsputtered parts of all three samples show nearly the same $H_c$, as expected. However, an increment in the sputtered parts is observed when we go deeper with the insertion of defects (see Fig. 4.8 (a)). It shows that sputtering at a larger depth is having a larger effect on $H_c$. In Fig. 4.8 (b) it is seen that sputtering at a larger depth is also having a larger effect on the EB. The main effect is not so much increasing the EB at the lowest temperatures, but shifting up $T_b$. Similar to $H_c$, $H_{eb}$ also gives similar values for the non-sputterd parts of all samples and yields a confirmation of the reproducibility of our samples.

Figure 4.9 shows the values of $H_c$ and EB versus the Ni concentration at a fixed temperature at 80 K for both part of the sample, i.e., unsputtered and sputtered. Figure 4.9 (a) shows how the $H_c$ values reduce with increasing Ni concentration up to 35 percent and increase again for the equiatomic sample. Figure 4.9 (b) shows how the EB values decrease with higher Ni(x) concentration, except for the pure Mn sample. Whether less or more, if we generalize the whole Fig. 4.9 for the sputtered part, $H_c$ and EB both are increased compared to the unsputtered part of the sample.

Note that the thickness of the FM Co is 5 ML in Fig. 4.7 and 10 ML in Fig. 4.8. The sample with the pure Mn layer in Fig. 4.7 (black data points) and the sample sputtered after the deposition of 10 ML Mn in Fig. 4.8 (also black data points) thus differ only by the thickness of the Co FM layer. If $H_c$ and $H_{eb}$ were exclusively determined by the coupling of the FM layer at the interface to the AFM layer, they would depend inversely on the thickness of the FM layer. Comparing the data of these two samples in Figs. 4.7 and 4.8, one can see that this is about the case, although there are subtle differences.

## 4.3 Discussion

We have got the following main results for the discussion :

**• Successful insertion of defects**

Successful insertion of defects within different depths of the AFM volume and on the surface of AFM has been carried out (Fig. 4.7 and 4.8).

**• Presence and identification of different kinds of defects**

There exist three kinds of defects in our samples of the AFM Mn layers, which are responsible for creating magnetic domains and the existence of the uncompensated pinned moments within these domains to produce the EB effect. These defects are:

(i) naturally occurring structural defects,

(ii) the chemical defects and

(iii) the deliberately introduced defects

We assume that chemical defects here occur by introducing Ni in the Mn system to make AFM $Ni_xMn_{100-x}$ alloy. While by the deliberately introduced defects we mean here the defects which occured by Ar ion sputtering, either in pure Mn or in the $Ni_xMn_{100-x}$ alloy.

The naturally occurring structural defects are unavoidable in all samples, which is the primary source of uncompensated pinned moments within the AFM magnetic domains and hence the EB effect.

For the unsputtered part of the samples, the chemical defects in the alloy NiMn play a significant role: by increasing Ni to the equiatomic concentration, the chemical defects can no longer be simple defects; instead, they provide the alloy opportunity to get more regular AFM spin structure with decreased anisotropy (Fig. 4.9). At Ni concentrations x=50 and x=0, the films have nearly perfect AFM spin structure with relatively smaller magnetic anisotropy, which results in a smaller EB field and smaller $T_b$. Insertion of chemical defects in Mn by adding less Ni in it produces magnetic domains in the AFM $Ni_xMn_{100-x}$ but still with more Mn-Mn neighbors than when more Ni is added to Mn, i.e., for $Ni_{50}Mn_{50}$. In the former case, more pinned spins can be created to enhance the magnetic anisotropy and hence higher exchange bias field and higher $T_b$ compared to the latter case. This is evident from our results in Fig. 4.9. These results are similar to previously obtained results [73] and are therefore attributed to (a) rotation of the non-collinear 3Q-like spin structure of $Ni_xMn_{100-x}$ from more out-of-plane to more in-plane direction for decreasing Ni concentration x, along with an associated increased magnetic anisotropy, and (b) a smaller domain wall width within the $Ni_xMn_{100-x}$ films at smaller x, leading to a smaller thickness required to establish exchange bias at a fixed temperature. On the other hand, in addition to these chemical defects, the insertion of structural defects, too, plays a significant role in the creation of AFM domains and hence pinned spins that are responsible for exchange bias. This is evident from the larger values of $H_{eb}$ (T) for the sputtered part of the $Ni_xMn_{100-x}$ compared to the unsputtered part of the sample.

**• Dominant role of structural defects within pure Mn**

The structural defects provided by Ar ion sputtering play a significant role in creating magnetic domains or uncompensated pinned moments within the pure Mn films compared to $Ni_xMn_{100-x}$. That is why we see more change or increase in $H_{eb}$(T) for the former case than the latter (Fig. 4.7). This is clear from the difference in the temperature-dependent $H_{eb}$ values for sputtered (black open symbols) and unsputtered (black filled symbols) part of the sample. This is because pure Mn sample obviously has a more significant number of Mn atoms exposed for sputtering and thus has more probability for the creation of a more significant number of uncompensated Mn pinned moments compared to $Ni_xMn_{100-x}$, where along with Mn atoms Ni atoms are also present. In pure Mn films, there exists a nearly perfect ordered structure which is when defected, results in a more effective production of domains containing more

pinned moments as compared to the case of $Ni_xMn_{100-x}$, which cannot produce that much number of pinned Mn on average because of the existence of Ni (Fig. 4.7 and 4.8).

**• Contribution of the structural defects with the depth in pure Mn**

The contribution of the structural defects increases with the distance from the FM layer (Fig. 4.8).

Stronger coupling between a pinning center and the FM layer results in a higher torque on the pinned moment in the AFM layer upon FM layer magnetization reversal, which could make it easier to break the pinning. In other words, if a pinning center is too close to the FM layer, no spin spiral or local horizontal domain wall might be accommodated, which would lead either to domains in the FM layer [152] or to the unpinning of the uncompensated moments to enhance the $H_c$. Following that idea, at higher temperatures, more distant pinning centers would thus dominate the EB, which consequently could exist only at larger film thicknesses. This would explain the increase of $H_{eb}$ and $T_b$ with AFM layer thickness [76]. These speculations are clearly confirmed by our results shown in Fig. 4.8. The results in Fig. 4.8 are fascinating: they show the contribution of all kinds of structural defects that occur in Mn films (naturally occurring structural defects, deliberately introduced structural defects at the interface and within the volume of the AFM Mn layer due to Ar sputtering). The contribution of the naturally occurring structural defects is evident from the unsputtered part of all the Mn films that couple with the Co film to emerge the EB effect. The interfacial defects certainly produce the EB effect, as is evident from the larger and smaller value of $H_{eb}(T)$ for the sputtered (green open symbols) and unsputtered (green open symbols) part, respectively. The volume defects within the Mn layer have an immense contribution to the EB effect (open red and open black symbols). Simultaneously, the results clearly differentiate the contribution of the bulk AFM spin structure from that of the FM/AFM interfacial contribution. The fact that the AFM bulk spin structure dominantly contributes to the phenomenon of exchange bias is fairly observed here. The $H_{eb}(T)$ values for the bulk defects due to sputtering are much larger (red and black symbols) than the interfacial defects (green symbols). There is possibility that deepen defects have an effect on further growth of the film, leading to defects also above the sputtered part.

## 4.4 Conclusion

In this chapter we have shown from the experimental results obtained by MOKE measurements on epitaxially grown $Co/Ni_xMn_{100-x}/Cu_3Au(001)$ samples exhibiting exchange bias ($0 \leq x \leq 50$), where in one part of the sample the $Ni_xMn_{100-x}$ layer is sputtered with a small dose of Ar ions at its surface or at different depths, that structural defects in the AFM layer introduced as a consequence of this sputtering lead to a higher exchange bias field and larger coercivity. It is attributed to a larger amount of magnetic pinning centers in the AFM layer, which are unanimously considered to be the origin of EB. These pinning centers are linked to structural or chemical defects and lead to an increase in the blocking temperature and a concomitant increase of the exchange bias field. This is most pronounced for samples with Ni concentrations of $x = 0$ and $x = 50$, which in the unsputtered state exhibit a smaller EB effect than the ones with Ni concentrations in between. This can be discussed as the effect of the introduced defects acting as pinning sites for EB, which in addition to the already-present defects determine the strength of the unidirectional anisotropy. Their smaller relative contribution in films with intermediate Ni concentrations can be attributed to the higher density of chemical defects in the chemically disordered alloy.

Introducing defects in $Co/Mn/Cu_3Au(001)$ samples, i.e., for $x = 0$, at different depths in the AFM Mn layer reveals a stronger effect on the EB for more deeply buried defects, while defecting the FM–AFM interface has a minor effect on the magnetic properties of the sample. This, on the one hand, confirms an assumption of the domain-state model of EB, namely that the pinning centers lying within the volume of the AFM layer are contributing the most to the EB effect and not the interfacial ones, on the other hand it demonstrates a distance dependence of the location of defects from the interface. The latter can be explained by a minimum distance required for an effective twisting of the coupling chain between pinning centers in the AFM layer and the FM-layer magnetization required to observe EB.

With the presented experiments, the two main ingredients responsible for the EB effect, i.e., the presence of uncompensated pinned magnetic moments acting as pinning centers and the location of these pinning centers within the volume of the AFM layer, have been tested by us. We could show that by introducing structural defects in the AFM layer at a certain distance from the interface to the FM layer, both the exchange bias field at a given temperature as well as the blocking temperature for EB can be significantly enhanced. The behavior of the EB upon introducing extra defects by slight sputtering

is compatible with a model in which local uncompensated pinned magnetic moments in the AFM layer interact with the FM layer by a path of direct exchange coupling within the AFM material.

# 5

# Growth, structure, and magnetic properties of artificially layered NiMn in contact to ferromagnetic Co on $Cu_3Au(001)$

## 5.1 Growth of artificially ordered alloys of Ni and Mn

In this work we fabricated artificially-ordered alloy films of Ni and Mn with atomic precision, i.e. in a layer-by-layer mode on a $Cu_3Au(001)$ single crystal. We have chosen Ni and Mn because in disordered alloy form, NiMn is a properly-explored single-crystalline AFM system [70–74,76,77,86,87,138,148]. Due to tiny lattice mismatch, $Ni_xMn_{100-x}$ shows layer-by-layer growth on $Cu_3Au(001)$ [70–74,76,77,138]. The repeated stacking of these different metallic layers (in sizes of atomic monolayers) is referred from now on as artificially-ordered layered films (ALF). $[Ni_1/Mn_m]$ or 1 ML Ni/**m** ML Mn/$Cu_3Au(001)$ multi-stacks with **m** ranges between 1 and 3 ML were prepared. The total thickness of these layered films was kept as 10, 12, 15, and 20 ML (Fig. 5.1). In parallel, for comparison, $Ni_xMn_{100-x}$ films of the same thicknesses and same Ni content were prepared in disordered alloy form too, to enable and understand the structural and magnetic properties in a better way for this system. One of the intriguing concepts in the study of these ALF is the interlayer magnetic exchange coupling of spins in one atomic layer to those in adjacent layers of same or different metal. The other aspect for this study would be that since the geometric arrangements in the ALF are highly selective compared to disordered alloys of the same elements, it is of great interest to compare the magnetization behaviors of both forms. We are specifically interested in

the ALF of Ni and Mn to have a model system which cannot exist naturally. This way one may design artificial system for specific applications. There are three basic pre requisites to grow ALF successfully along the film normal; (i) each layer thickness should be regulated on an atomic scale, (ii) interdiffusion should be sufficiently suppressed, especially at the interfaces and, (iii) deposited materials should form a layered structure in form of layer-by-layer growth.

$Ni_xMn_{100-x}$ films are prepared by the simultaneous evaporation of Ni and Mn on $Cu_3Au(001)$ while for the preparation of ALF of Ni and Mn, a special kind of shutter is used at the tip of the four-pocket evaporator to precisely control the evaporation of the materials, and open one pocket at a time. In alloy samples, the Ni concentration x was varied by optimizing the individual deposition rates while in the ALF case we kept nearly the same evaporation rate. The growth rate of the films is typically between 0.5 and 2 ML per minute, and was checked by counting the oscillations in the (0, 0) spot MEED intensity recorded during evaporation. Note that on the top of each sample, a 10 ML FM Co film is deposited, which grows epitaxially on top of NiMn or Mn AFM layers [70, 71, 73, 76, 138], and exhibits an in-plane easy axis of magnetization.

## 5.2 Results

Figure 5.1 shows schematic illustrations of the three types of ALF ultrathin films that have been prepared on $Cu_3Au(001)$ at T = 300 K, keeping the thickness of Ni to 1 ML while changing the thickness of the Mn layers from 1 to 3 ML. For each of these three geometries of ALF, four different thicknesses have been grown, namely 10, 12, 15 and 20 ML, by adjusting the thickness of the last Mn layer. For comparison, films of the same thicknesses were prepared with disordered $Ni_xMn_{100-x}$ alloys in the same conditions. Our aim was that for films of the same thickness, both ALF and disordered alloy should have nearly equal Ni content. For 20 ML of ALF, we have additionally investigated samples in which we exchanged the deposition sequence of Ni and Mn shown in Fig. 5.1 (d–f).

The growth of ALF of Ni and Mn and disordered AFM alloy $Ni_xMn_{100-x}$ at T = 300 K was monitored by means of MEED oscillations. Fig. 5.2 shows the reflected MEED intensity as a function of deposition time for 61 ML Mn on $Cu_3Au(001)$. The deposition time is converted into a monolayer thickness scale under the assumption that a maximum in the MEED intensity corresponds to a filled integer monolayer. For our work, full grip on MEED oscillations

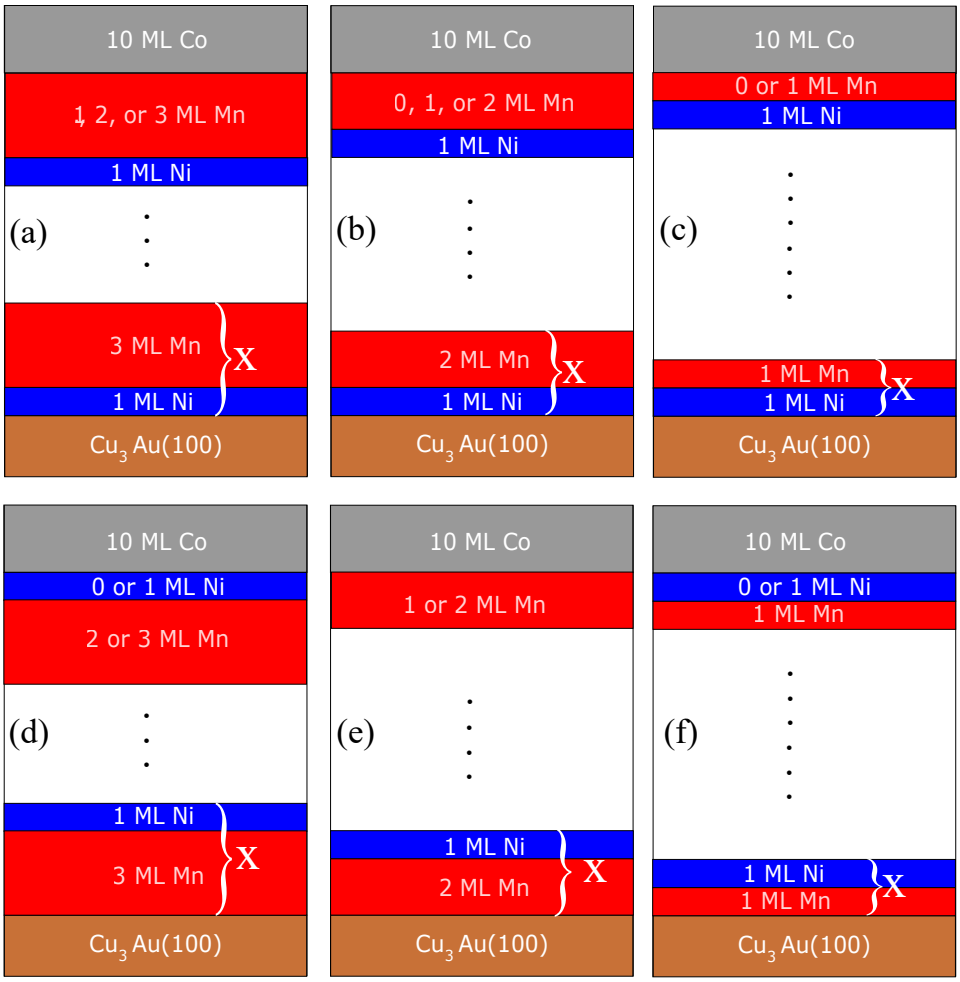


**Figure 5.1:** Schematic illustration of ALF of **m** ML Mn/1 ML Ni/$Cu_3Au$(001) (a–c) and 1 ML Ni/**m** ML Mn/$Cu_3Au$(001) (d–f); where **m** = 3 (5.1 (a) and (d)), **m** = 2 (5.1 (b) and (e)), **m** = 1 (5.1 (c) and (f)). The total thickness of these stacks is kept as 10, 12, 15 and 20 ML. 10 ML FM Co is always evaporated on top of these films for magnetic characterization.

with time for both Ni and Mn was one of the prerequisites. That is why we optimized initially the growth conditions. Ni always grows in layer-by-layer fashion on $Cu_3Au$(001) up to 20 ML [138, 153], Mn was also reported to grow in layer-by-layer growth mode [154], but this was not the case for all growth conditions [86, 137, 138, 155, 156]. The periodic oscillations of the specular beam intensity signify layer-by-layer growth in our case. In Fig. 5.2 the oscillations persist up to the end, i.e., 61 ML, where the shutter was closed, which has never been achieved before up to the best of our knowledge. The possible reasons might be the pressure during deposition and different MEED geometries: in our case, pressure was 8 $\times 10^{-10}$ mbar during the deposition of

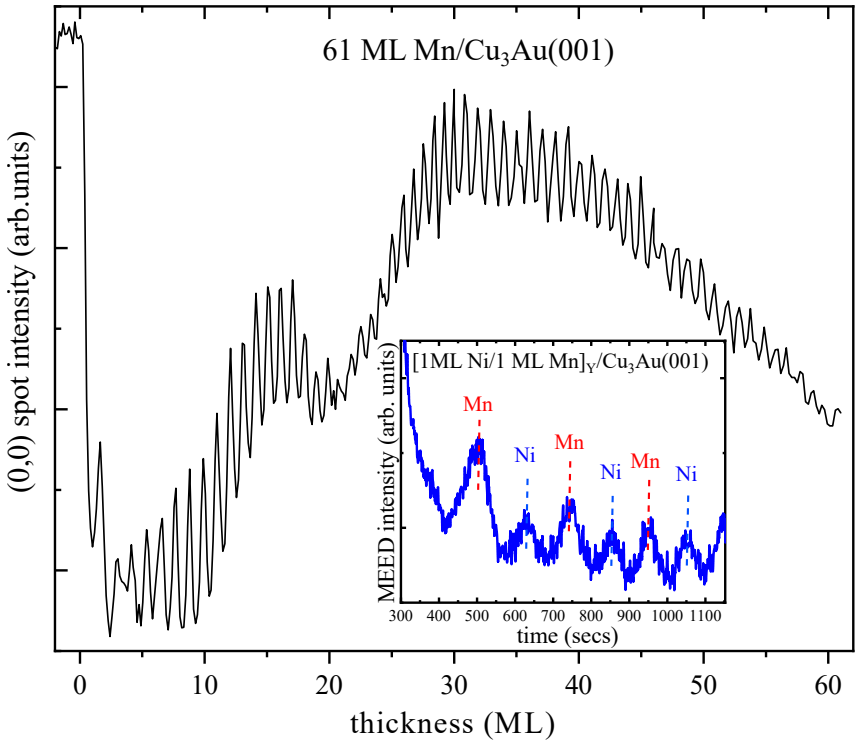


**Figure 5.2:** MEED oscillations during the deposition of 61 ML Mn on $Cu_3Au(001)$. The inset show MEED oscillations for a 6 ML Ni and Mn ALF on $Cu_3Au(001)$. The first maximum corresponds to 1 ML filling of Mn (represented by the red vertical bar) and the second maximum corresponds to an additional 1 ML Ni (represented by the blue vertical bar), and so forth.

the films, grazing angle (2° ) and the beam energy (2.5 keV ). In the previous works, grazing angles of 8.6° [154] and 1° [137, 155], and beam energies of 3 keV [154] and 5 keV [137, 155], respectively, have been used. These differences may affect the MEED oscillations.

In the MEED curves in Fig. 5.2 we can see a clear intensity minimum at 1.5 ML and then a rise up to 15 ML, followed by the immediate fall in the MEED curve intensity and the reduction in the amplitude of the MEED oscillations. Lin *et al.*, [137, 155] have reported with the help of STM, LEED images and LEED I(V) curves that Mn films on $Cu_3Au(001)$ deposited at room temperature undergo a sudden structural transition from *fcc* to *fct*. This can be speculated from the first transition in the intensity of our MEED oscillations as well, which occurs between 15-20 ML and which could not be achieved in Refs. [137, 155]. We also think that another structural transition may occur at 30 ML (second peak in the curve), as after the first transition (at 15 ML) the MEED intensity goes up (instead of coming down in the normal case)

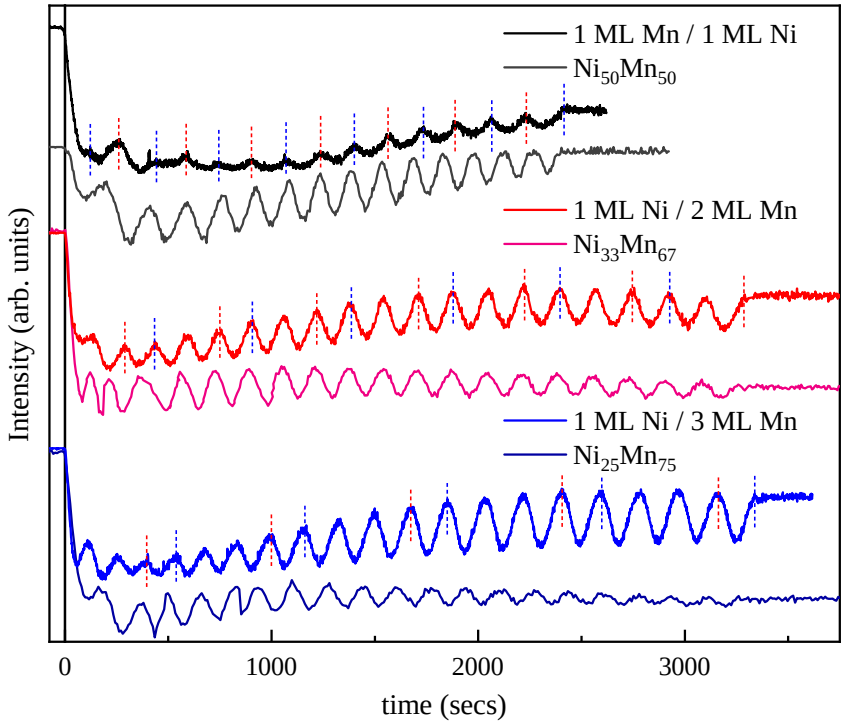


**Figure 5.3:** MEED oscillations for 15 and 20 ML ALF and corresponding disordered $Ni_xMn_{100-x}$ alloy films on $Cu_3Au(001)$. For ALF, the switching of the shutter between sources of Ni and Mn evaporation is marked with dashed vertical bars. The blue bar corresponds to 1 ML filling of Ni, while the red bar correlates to 1 ML (black curve), 2 ML (red curve), and 3 ML (blue curve) filling of Mn. For alloy films, the amplitude of the oscillations decreases with increasing Mn content during the deposition, while in the case of ALF, it depends on the Ni and Mn sequence. Depositing Mn (Ni, e.g., black curve) first in ALF, e.g., red and blue curves, the amplitude of the oscillations increases (decreases).

and then slowly reduces, accompanied by damped oscillations. However, to comprehend this observation of the second transition fully, it is necessary to perform a complete structural study of Mn films with growing thickness.

The inset in Fig. 5.2 shows MEED oscillations during the deposition of a 6 ML ALF of $[1\ Mn/1\ Ni]_3$ on $Cu_3Au(001)$. Ni shows reduced amplitudes of oscillation compared to Mn layers. A similar behavior has been reported for Fe/Cu ALF (small lattice mismatch between *fcc* Fe and *fcc* Cu) on Cu(001), where Cu has a higher amplitude of oscillations than Fe [157].

An oscillating MEED intensity, which is a fingerprint of a layer-by-layer growth mode, was found for all disordered $Ni_xMn_{100-x}$ alloys and the ALF.

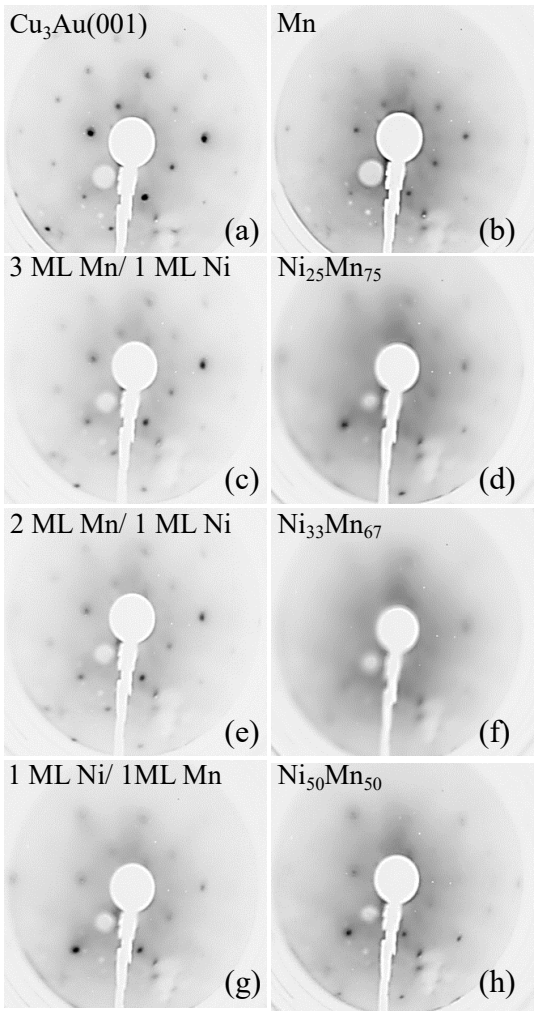


**Figure 5.4:** LEED patterns of (a) clean $Cu_3Au(001)$ and of 9 ML of (b) Mn, (c) 3 ML Mn/1 ML Ni, (d) $Ni_{25}Mn_{75}$, (e) 2 ML Mn/ 1 ML Ni, (f) $Ni_{33}Mn_{67}$, (g) 1 ML Mn/1 ML Ni, and (h) $Ni_{50}Mn_{50}$. All LEED images are taken at room temperature with a beam energy of 130 eV. The LEED patterns show a typical c(2×2) structure for all images. The LEED spots are sharper in case of ALF compared to the disordered $Ni_xMn_{100-x}$ alloy films.

Some of them are shown in Fig. 5.3. For ALF of **m** ML Mn/1 ML Ni or 1 ML Ni/**m** ML Mn, the switching of the shutter between sources of Ni and Mn evaporation, is marked with dashed vertical bars. Blue bars correspond to 1 ML filling of Ni, while red bars correlate to the 1 ML (black curve), 2 ML (red curve) and 3 ML (blue curve) filling of Mn. A difference in the MEED oscillation amplitudes for Ni and Mn in the ALF were only observed in 1 ML Mn/1 ML Ni films (clearly visible from the inset of Fig. reftwo), where Mn depicts higher amplitudes than Ni. For alloy films, the amplitude of the

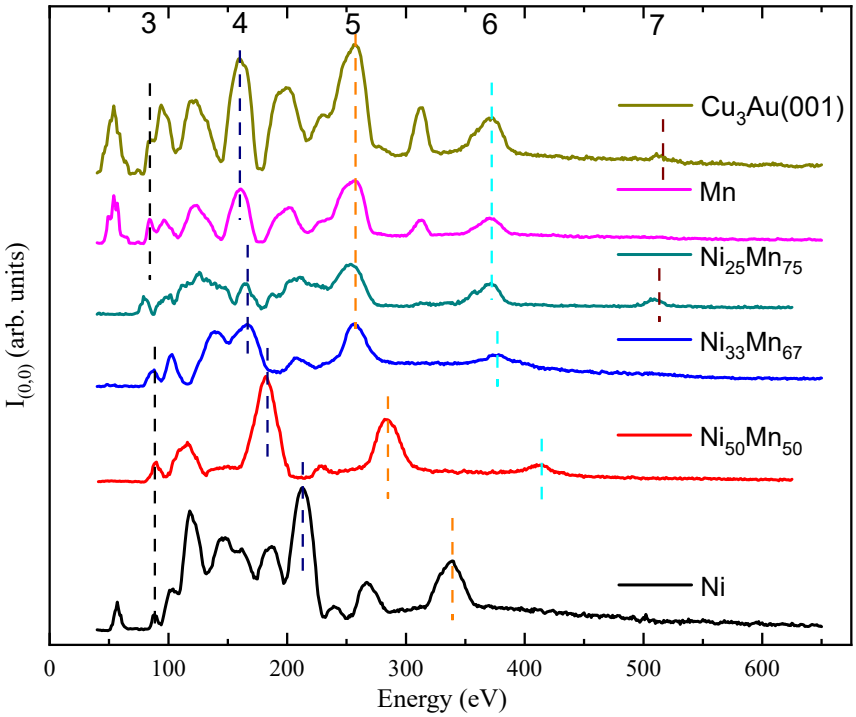


**Figure 5.5:** Room temperature LEED I(V) curves for a series of different 9 ML thick disordered $Ni_xMn_{100-x}$ (including pure Mn and Ni) films.

oscillations decreases with film thicknes, while it increases for ALF. The reason for this will be discussed later.

Figure 5.4 shows the LEED images for the substrate, pure Mn, disordered NiMn alloy, and ALF, of 9 ML thickness each. All the LEED images are taken at room temperature with a beam energy of 130 eV. The LEED patterns of ALF show typical c(2×2) superstructure with much sharper LEED spots compared to the disordered alloy films. The additional ordered structure of ALF might just come from a reconstruction of Mn atoms, or even be due to some Au segregation to the very first atomic layers of these films, as already reported for thin Mn, as well as Co-Ni alloy films grown on top of $Cu_3Au(001)$ [137,153], or it could be also due to the buckling of either the Mn atoms at the surface or in each layer [69].

The LEED I(V) curves for disordered NiMn alloy films, along with pure Ni and Mn (9 ML thick), as deposited at room temperature, are shown in Fig. 5.5. The (00) spot was used for obtaining the LEED I(V) curves with an incidence angle of $\theta = 85°$. Increasing the Ni content in these films, one can observe a clear shift of the peaks to higher energies.

Figure 5.6 shows room-temperature LEED I(V) curves for 9 ML thick

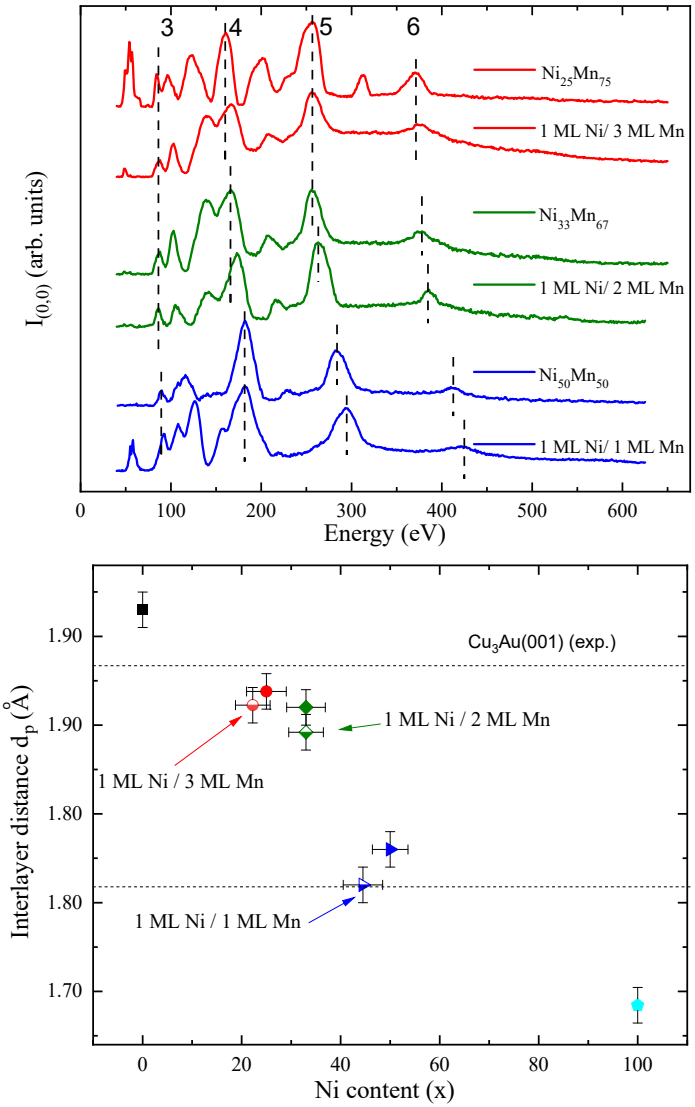


**Figure 5.6:** (a) Room-temperature LEED I(V) curves for 9 ML thick disordered $Ni_xMn_{100-x}$ and ALF of 1 ML Ni/**m** ML Mn/$Cu_3Au$(001), where **m** ranges from 1 to 3. Note the shift of the peaks to higher energies for ALF compared to the corresponding disordered alloy films. A shift of the peaks to higher energies is also observed with increasing Ni content within both types of films. (b) Interlayer spacing d versus Ni content x. The dashed lines at 1.883 and 1.76 Å indicate the interlayer distances in *fcc* $Cu_3Au$(001), as experimentally obtained here, and in bulk $L1_0$ NiMn along the c-axis, respectively. For ALF of 1 ML Ni/1 ML Mn films, d coincides with the value of the c-axis in bulk $L1_0$ NiMn. For pure Mn (x=0) and pure Ni (x=100) the interlayer distances were 1.92 and 1.69 Å.

disordered alloy $Ni_xMn_{100-x}$ together with the corresponding ALF of 1 ML Ni/**m** ML Mn, deposited on $Cu_3Au$(001). One can observe a shift of the

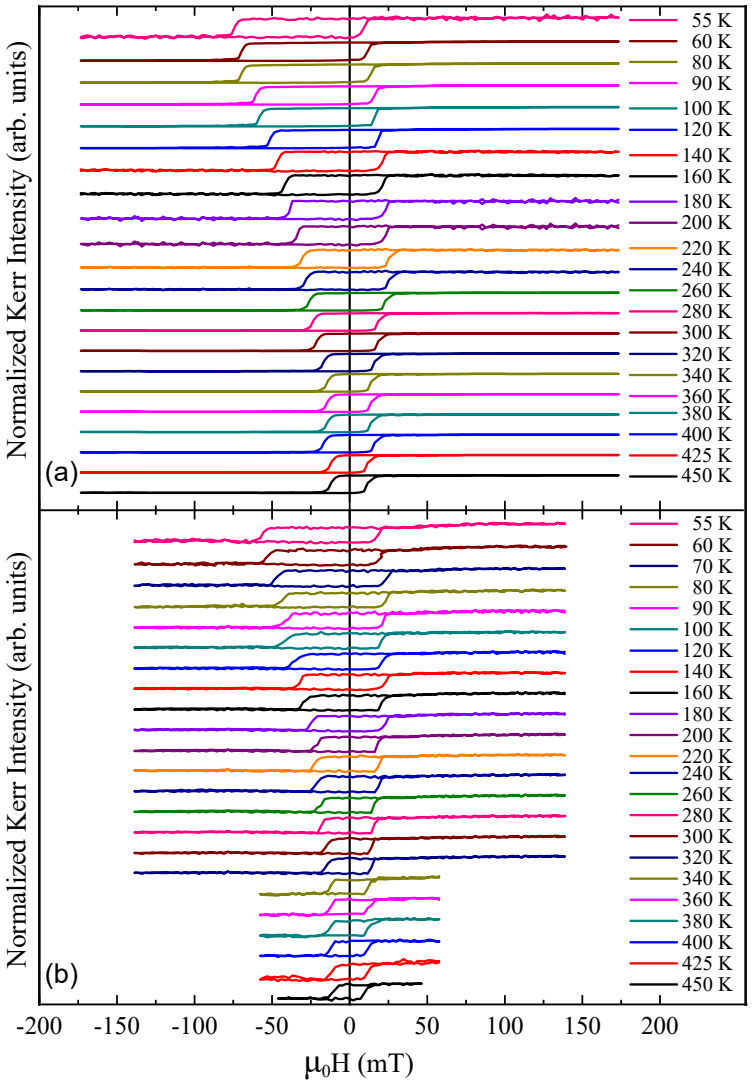


**Figure 5.7:** Normalized hysteresis loops for 10 ML Co on 15 ML thick (a) 2 ML Mn/1 ML Ni ALF and (b) $Ni_{33}Mn_{67}$ disordered alloy films, measured with longitudinal MOKE at different temperatures. The sample was field-cooled in +25 mT from 500 K, above $T_N$ of Mn and below the Curie temperature of the Co film.

peaks to higher energies for ALF compared to the corresponding disordered alloy films. The shift of the peaks to higher energies is also observed with increasing Ni content within both types of the prepared films. Fig. 5.6 (b) shows the resulting interlayer spacing d versus Ni content x. With increasing Ni concentration the interlayer distance decreases. It should be noted that in two of the ALF, namely, 1 ML Ni/3 ML Mn and 1 ML Ni/1 ML Mn, we have a bit less Ni content (2.78% and 5.5%, respectively) than in the corresponding $Ni_{25}Mn_{75}$ and $Ni_{50}Mn_{50}$ disordered alloys because at 9 ML the growth stops with Mn and not Ni. The size of the horizontal error bars for the Fig. 5.6

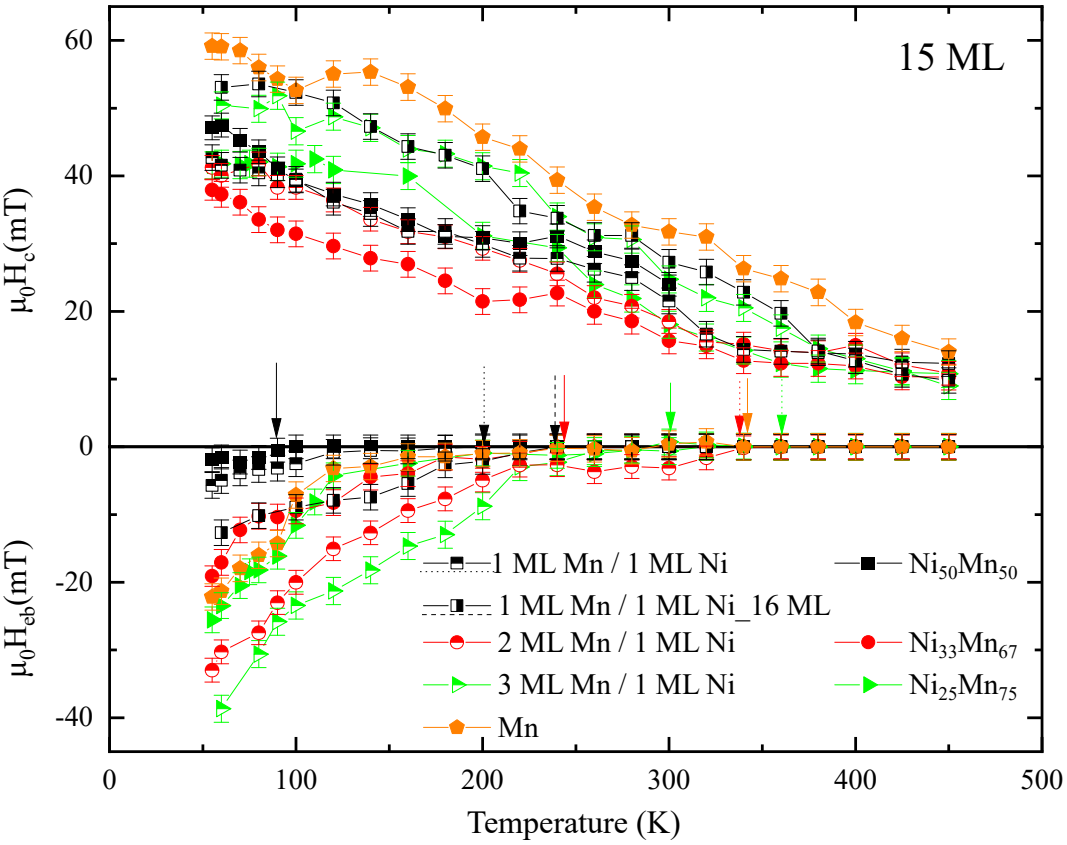


**Figure 5.8:** Temperature dependence of the coercivity (positive field axis) and exchange bias field (negative field axis) of 15 ML thick films of pure Mn, $Ni_{25}Mn_{75}$, $Ni_{33}Mn_{67}$,$Ni_{50}Mn_{50}$ disordered alloys and 3 ML Mn/1 ML Ni, 2 ML Mn/1 ML Ni, 1 ML Mn/1 ML Ni ALF. Note that an additional 1 ML Mn/1 ML Ni ALF of 16 ML thickness is also prepared for the comparison.

(b) were extracted from the uniformity of the film on the substrate. For the vertical error bars, firstly the average of multiple scans were taken, secondly the error was calculated from the slope of the fit which includes the error in the selection of the exact position of the peaks.

The interlayer distances are smaller for the ALF (compared to its corresponding disordered alloys), which is in agreement with the Fig. 5.4. The reason could be that the Mn sheets can develop a buckling to adopt to the smaller lattice constant of the substrate, which then continues through the layer, which is not possible for the disordered alloy films [69]. "The dashed lines at 1.88 and 1.76 indicate the interlayer distance in *fcc* $Cu_3Au(001)$, as experimentally obtained here, and in bulk $L1_0$ NiMn along the c-axis, respectively. For ALF of 1 ML Ni/1 ML Mn, d coincides with the value of the c-axis in the bulk $L1_0$ NiMn " [138].

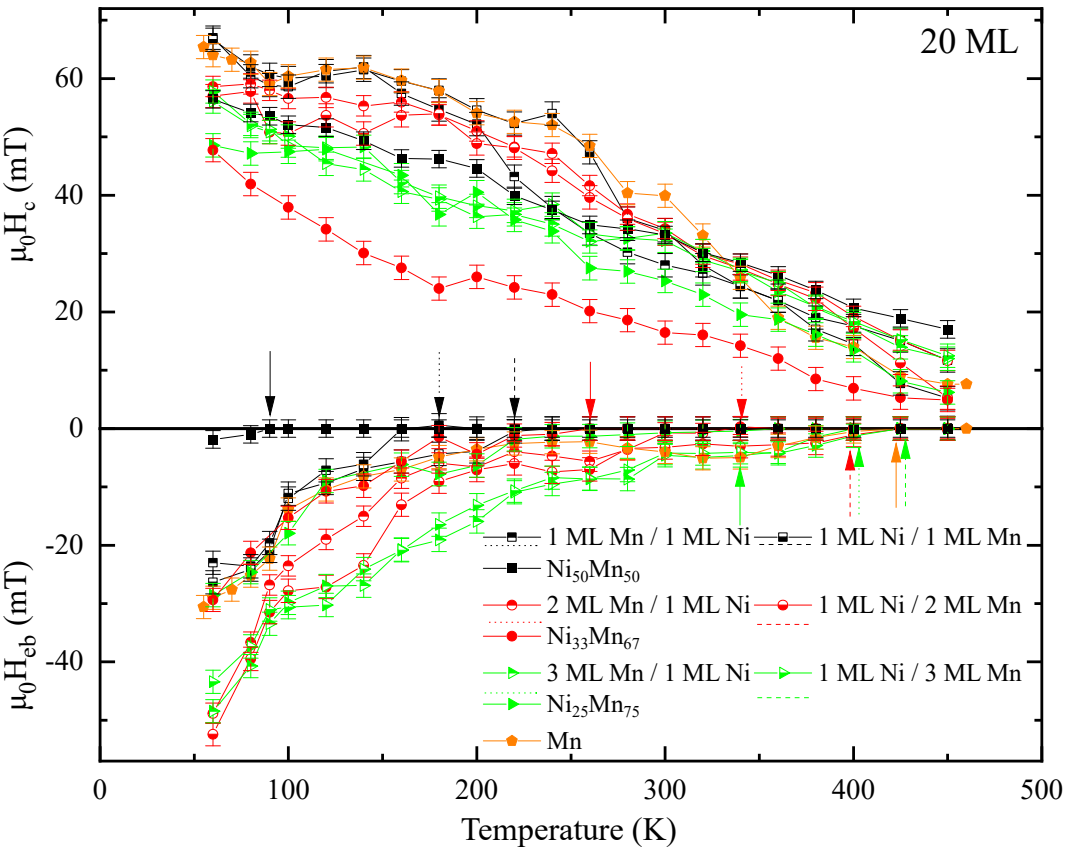


**Figure 5.9:** Temperature dependence of the coercivity (positive field axis) and exchange bias field (negative field axis) of 20 ML thick films of pure Mn, $Ni_{25}Mn_{75}$, $Ni_{33}Mn_{67}$, $Ni_{50}Mn_{50}$ disordered alloys and 3 ML Mn/1 ML Ni, 1 ML Ni/3 ML Mn, 2 ML Mn/1 ML Ni, 1 ML Ni/2 ML Mn, 1 ML Mn/1 ML Ni, 1 ML Ni/1 ML Mn ALF. The arrows indicate the blocking temperature for the $H_{eb}$ curves. Arrows with solid lines represent disordered alloys, arrows with dotted lines represent the ALF in which Ni was evaporated first, while arrows with dashed lines represent ALF in which Mn was evaporated first.

Magnetic hysteresis loops are measured with longitudinal MOKE at different temperatures after field cooling with +25 mT from above the Néel temperature ($T_N$) of Mn and below the Curie temperature ($T_C$) of the Co, i.e., from ~500 K, which provided an EB shift along the negative field direction. Figure 5.7 shows an example of temperature-dependent hysteresis loops. Here the samples are (a) 10 ML Co/15 ML $Mn_2Ni_1$ and (b) 10 ML Co/15 ML $Ni_{33}Mn_{67}$/$Cu_3Au$(001). Nearly rectangular-shaped loops for both cases are obtained, in which a coercivity ($H_c$) enhancement with decreasing temperature can be observed. Although the general behavior of the temperature-dependent hysteresis loops is similar for the ALF and disordered alloy cases, the details

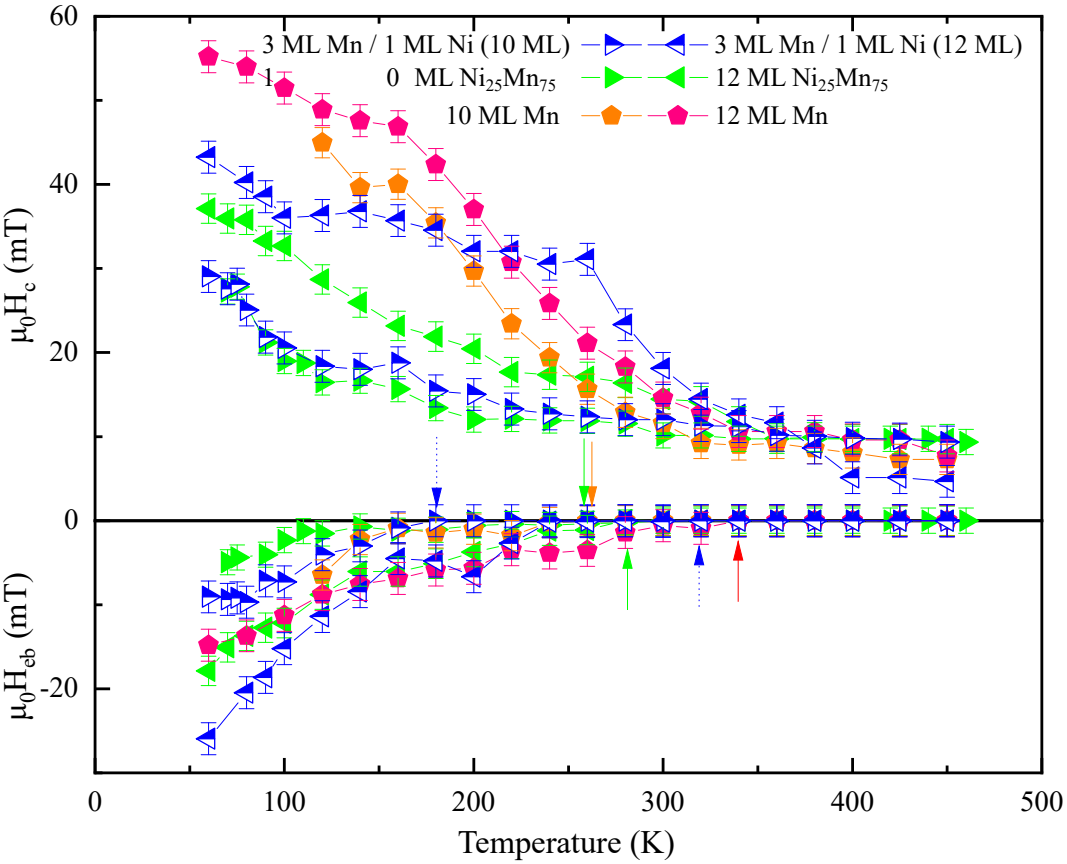


**Figure 5.10:** Temperature dependence of the coercivity (positive field axis) and exchange bias field (negative field axis) of 12 ML thick films of pure Mn, disordered $Ni_{25}Mn_{75}$ alloy and an ALF of 3 ML Mn/1 ML Ni. The arrows indicate the blocking temperature for the $H_{eb}$ curves. Downward (upward) faced arrows denote the 10 ML (12 ML) films.

are different. The main differences are (i) $H_c$(T) for the ALF is higher than that of the disordered alloy at low temperatures, and the reduction of $H_c$ to lower values occurs at higher temperatures for the ALF; (ii) the EB field ($H_{eb}$) for the ALF is vanishing at ~340 K, while it ceases for the disordered alloy below ~250 K, which means that the blocking temperature is also increased in the ALF.

Figure 5.8 shows the temperature-dependent evolution of the coercivity (positive field axis) and exchange bias field (negative field axis) of 15 ML thick films of pure Mn, $Ni_{25}Mn_{75}$, $Ni_{33}Mn_{67}$, $Ni_{50}Mn_{50}$ disordered alloys and 3 ML Mn/1 ML Ni, 2 ML Mn/1 ML Ni, 1 ML Mn/1 ML Ni ALF grown on $Cu_3Au$(001) in contact with in-plane magnetized FM Co. Note that in Fig. 5.8 one additional ALF 1 ML Mn/1 ML Ni film of different thickness, namely 16 ML, is shown together with the other films to see the behavior of 1 additional

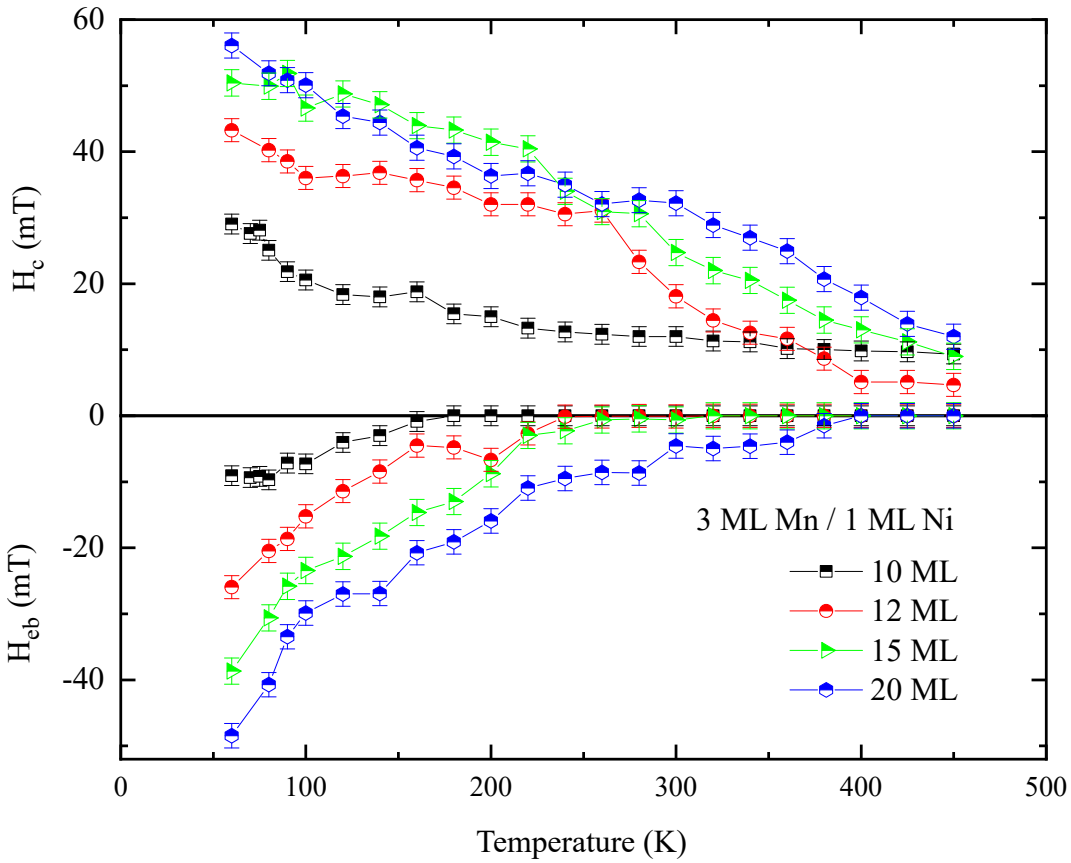


**Figure 5.11:** Temperature dependence of the coercivity (positive field axis) and exchange bias field (negative field axis) for different thicknesses of ALF of 3 ML Mn/1 ML Ni.

ML of Mn on top for this film. The coercivities of the ALF samples are higher than those of the disordered $Ni_xMn_{100-x}$ alloys, except in the equi-atomic case. Interestingly, adding one ML of Mn to the 1 ML Mn/1 ML Ni film, making it in total 16 ML, results in a higher coercivity, exchange bias field, and $T_b$ than 15 ML of the same Ni concentration as well as than in the corresponding equi-atomic disordered alloy. Again, with decreasing Ni concentration, $T_b$ shifts to higher values in both types of films, disordered alloys and ALF.

In this kind of magnetic thin film, $H_c$ of the FM layer alone typically decreases monotonically (with a small slope) with increasing temperature. A monotonic decrease of $H_c$ could thus be present also in the absence of exchange coupling between the AFM and the FM layers. However, we observe a discontinuity in the slope of $H_c$ versus temperature, which is typical for exchange-coupled AFM/FM bilayer systems [149]. The point at which this discontinuity of the temperature-dependent $H_c$ occurs is considered as $T_N$. For its estimation, we follow the procedure already used in [148, 149] and fit a straight line

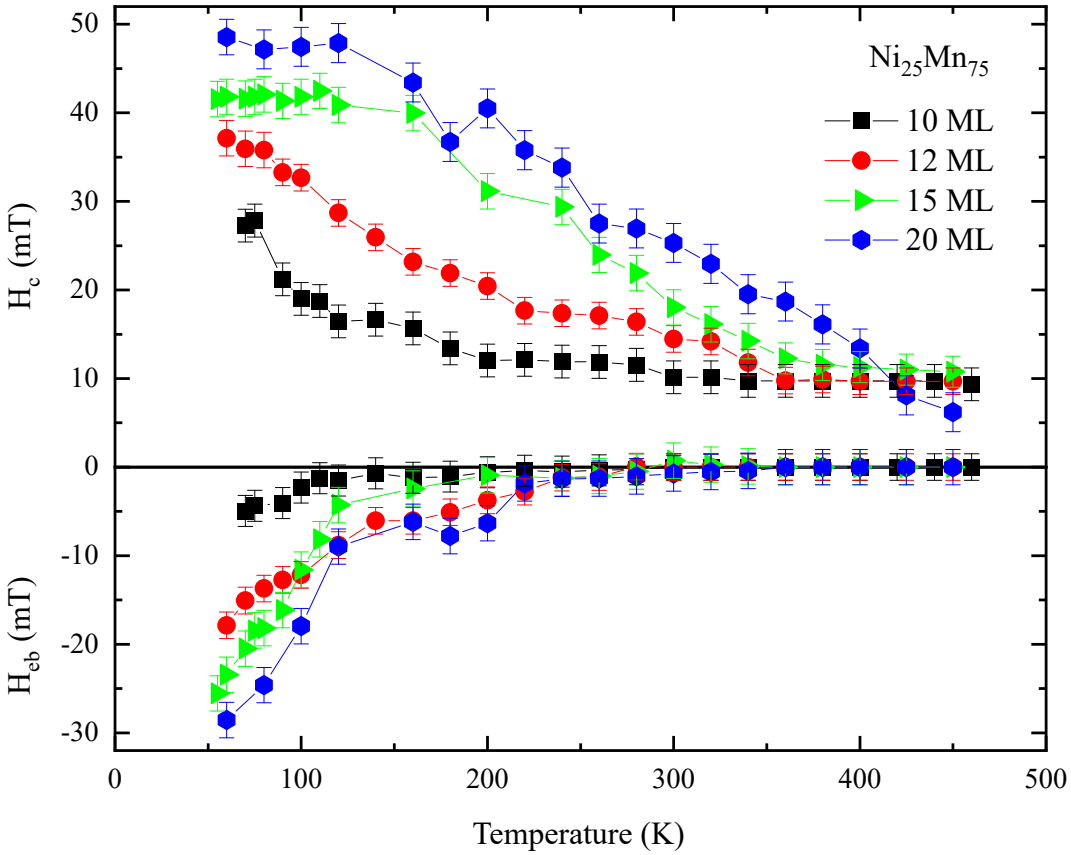


**Figure 5.12:** Temperature dependence of the coercivity (positive field axis) and exchange bias field (negative field axis) for different thicknesses of $Ni_{25}Mn_{75}$ films.

to the high-temperature side of the $H_c$(T) data to represent the behavior of the uncoupled FM layer. The temperature value at which the measured $H_c$ significantly diverges from this line is defined as Néel temperature $T_N$ of the AFM layer in the bilayer. The error in this method is less than $\pm$10 K [149]. To avoid an alloying effect of the AFM and FM materials and also at the interfaces of Ni and Mn in ALF particularly, we did not take measurements above 500 K.

It is also important to note that the exchange bias field and $T_b$ for the ALF are much higher than the ones of the corresponding disordered alloy films. This might be due to the vertical contraction of the layers caused by the buckling of Mn atoms in these ALF layers (Fig. 5.6), which provides stronger exchange coupling between layers in the AFM in these kind of films and as such enlarge the effect on the FM layer.

Figure 5.9 shows the temperature-dependent behavior of the coercivity (positive field axis) and exchange bias field (negative field axis) of 20 ML thick

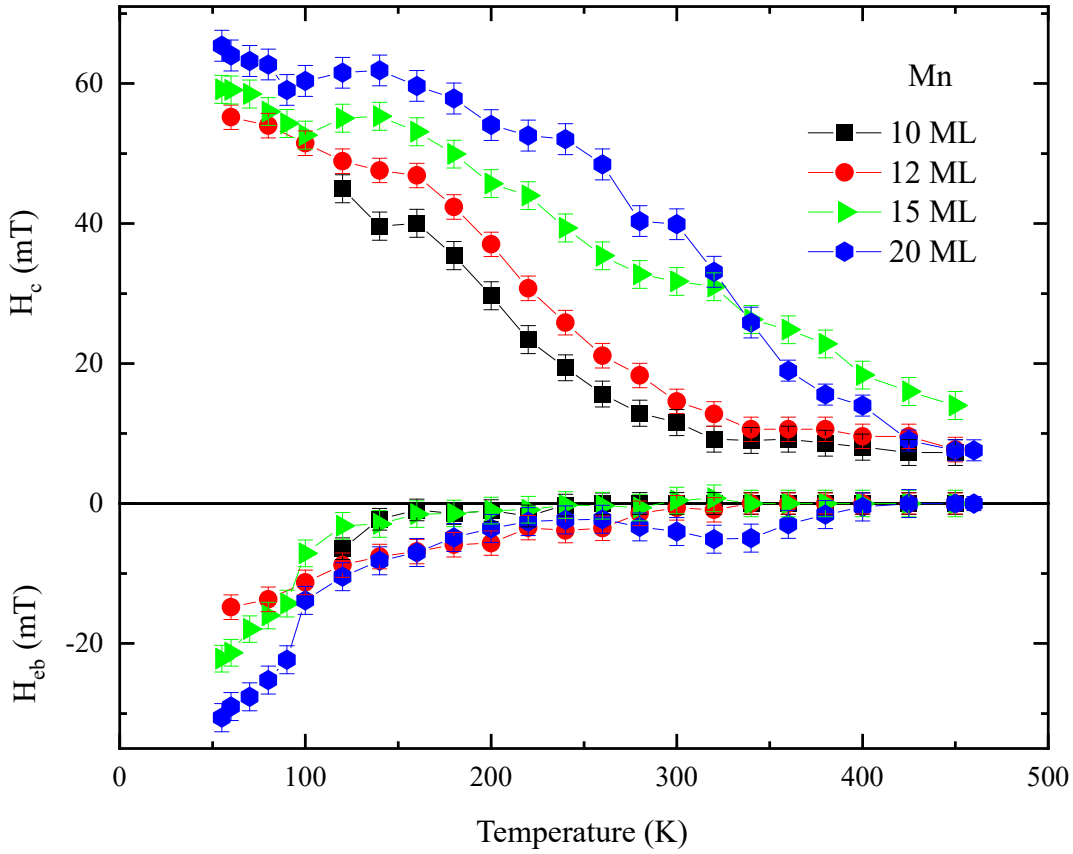


**Figure 5.13:** Temperature dependence of the coercivity (positive field axis) and exchange bias field (negative field axis) for different thicknesses of Mn films.

films of pure Mn, $Ni_{25}Mn_{75}$, $Ni_{33}Mn_{67}$, $Ni_{50}Mn_{50}$ disordered alloys and 3 ML Mn/1 ML Ni, 1 ML Ni/3 ML Mn, 2 ML Mn/1 ML Ni, 1 ML Ni/2 ML Mn, 1 ML Mn/1 ML Ni, 1 ML Ni/1 ML Mn ALF grown on $Cu_3Au(001)$ in contact with in-plane magnetized FM Co. As for the 20-ML films, $H_{eb}$ as well as $T_b$ increase with decreasing Ni concentration for both, disordered alloys and ALF. For each concentration, the ALF shows much higher $H_{eb}$ as well as $T_b$ and the same is true for the coercivity values. More specifically, the ALF when Mn is evaporated first and then Ni on top show even higher values of $H_{eb}$ as well as $T_b$.

This means that if the growth of ALF stops with a Mn layer on top rather than a Ni layer, then it boosts $H_{eb}$ as well as $T_b$, as it was the case in 16 ML ALF of 1 ML Mn/1 ML Ni which was compared to 15 ML of the same film (Fig. 5.8). The equi-atomic $Ni_{50}Mn_{50}$ disordered film hardly shows any exchange bias field, which is in agreement with the work of Khan *et al.* [138], but interestingly equi-atomic ALF, i.e., 1 ML Mn/1 ML Ni and 1 ML Ni/1

ML Mn, both show a sizeable exchange bias effect with $T_b$ of 180 K and 220 K, respectively. Exchange bias for the equi-atomic alloy films before was only found in 35 ML thick films [138]. The $Ni_{33}Mn_{67}$ disordered alloy film has a $T_b$ of 260 K, while the ALF with nearly the same Ni content shows a $T_b$ of 340 K (2 ML Mn/1 ML Ni) and 400 K (1 ML Ni/2 ML Mn), respectively. In the latter case we have one extra monolayer of Mn on top of the film compared to the former case, which means 5% more Mn in one geometry than in the other. Again, an additional top Mn layer is enlarging $H_{eb}$ as well as $T_b$, as already discussed above. $Ni_{25}Mn_{75}$ shows the second-highest value of the blocking temperature (340 K) among the disordered alloy films, after pure Mn (425 K). The ALF with nearly similar content of Ni and Mn to the $Ni_{25}Mn_{75}$ disordered alloy yields even higher values of coercivity, exchange bias field, and $T_b$ of 400 K (3 ML Mn/1 ML Ni) and 425 K (1 ML Ni/3 ML Mn).

Figure 5.10 presents the temperature-dependent coercivity (positive field axis) and exchange bias field (negative field axis) of 12 and 10 ML thick films of pure Mn, disordered $Ni_{25}Mn_{75}$ alloy, and the ALF of 3 ML Mn/1 ML Ni grown on $Cu_3Au(001)$ in contact with in-plane magnetized FM Co of 10 ML thickness. Also here, the ALF show higher values of the exchange bias field and $T_b$ compared to the corresponding disordered $Ni_xMn_{100-x}$ alloys.

For three selected samples, the temperature-dependence of coercivity and the exchange bias field for different thicknesses is shown in Figs. 5.11, 5.12, and 5.13. It shows that at a fixed lower temperature, e.g., 70-80 K, the coercivity and the exchange bias field increase with thickness for all three samples.

## 5.3 Discussion

Ni and Mn layers were successfully grown layer by layer with clear MEED oscillations on $Cu_3Au(001)$. Pronounced MEED oscillations for pure Mn had been observed by Schirmer *et al.*, for 20 ML thick films [154] and by Lin *et al.*, for about 8 ML [137], while others did not [86,137,138,155,156]. In analogy to the results reported by Lin *et al.*, [137,155], we interpret the discontinuity around 20 ML in our MEED curves as the signature of an fcc-fct structural transition. During the deposition of ALF of [Ni/Mn] in case of equal proportion of Ni and Mn, we saw that Mn shows a high amplitude of MEED oscillations while Ni show smaller amplitudes (Fig. 5.2). However other films with higher Mn proportion (Fig. 5.3) did not show such a behavior, which might be explained by film relaxation with higher Mn content.

LEED patterns of the clean $Cu_3Au(001)$ substrate and of different disordered $Ni_xMn_{100-x}$ alloy films (including pure Mn) reveal that the ordered

$Cu_3Au(001)$ surface is characterized by the (1/2, 1/2) spots of the c(2×2) superstructure, the pattern which is also found for the disordered alloy films (though with less intensity because of roughness) and ALF (with high intensity and sharpness of the surfaces). The reason for the ordered structure is discussed in detail for disordered NiMn alloy on $Cu_3Au(001)$ in Refs. [71,137,155]. The sharpness of the LEED spots and high intensity in the ALF probably reveals the long range coherent growth which can be confirmed from LEED I(V) curves (Fig. 5.6). The vertical interplanar distances obtained from these LEED I(V) curves in the kinematic approximation reveal a contraction in ALF compared to disordered alloy films for similar Ni content (Fig. 5.6). Our results agree with the findings discussed in a recent review article [158]. One of the possible reasons could be that there is no intermixing of Ni and Mn in ALF or, if there were intermixing, then it is strictly limited to the interfaces.

Altogether the blocking temperature extends to higher temperatures with decreasing Ni concentration in all samples (shown with the colored arrows in Figs. 5.8, and 5.9), which confirms previous results on this system [138]. When we consider the equiatomic case, the difference in the $T_b$ between ALF and disordered alloy (Figs. 5.8 and 5.9) is much more compare to the difference between other ALF e.g., 2 ML Mn/ 1 ML Ni and 3 ML Mn/1 ML Ni and its corresponding alloys i.e., $Ni_{33}Mn_{67}$ and $Ni_{25}Mn_{75}$, respectively. So by reducing Ni content the difference of $T_b$ between ALF and its disordered alloy also decreases (Figs. 5.8 and 5.9).

The important information from Fig. 5.9 is that ALF [Ni/Mn] or [Mn/Ni] show a higher coercivity and exchange bias field than the corresponding disordered $Ni_xMn_{100-x}$ alloys. Furthermore, in ALF [Ni/Mn] in which Mn is evaporated first, the blocking temperature, exchange bias field and coercivities are higher for the same thicknesses compared to the ALF where Ni is evaporated first. There could be many reasons for that, among them; for few films in ALF case when we start with evaporating Mn first, we end up with Mn again. This results in a bit more Mn than Ni compared to the [Mn/Ni] case when Ni is evaporated first (see Fig. 5.1). And thus more Mn means a large number of unpaired electrons than in other geometry of ALF (having few percent less Ni) of the same thickness and hence enhanced $H_{eb}$, $T_b$, and $H_c$. For a reference we can also take a look to pure Mn in the same graph (Fig. 5.8) as well as in Figs. 5.9 and 5.10, which shows higher values of $H_{eb}$ than any other $Ni_xMn_{100-x}$ alloy films for 20 ML thickness.

All in all, the interlayer exchange coupling is much stronger in ALF of NiMn compared to the disordered alloys (as seen from Figs. 5.8, 5.9, and 5.10), as these films show some reconstruction or buckling of the atoms in every sheet

which leads to the sharpness of the LEED spots and contraction in vertical interplanar spacing. From Figs. 5.8, 5.9 and 5.10 it is clear that $T_b$ increases to higher temperatures with (i) thickness and (ii) reduced Ni concentration for both, ALF and disordered alloys (more clearer from Figs. 5.11, 5.12, and 5.13). The investigations of these films was limited to a maximum thickness of 20 ML. The reason was that films thicker than this show mixing of the Ni and Mn layers while going beyond $T_{AFM}$ of NiMn for field-cooling the samples for magnetic measurements.

## 5.4 Conclusion

We have investigated the growth and structural properties of ALF single-crystalline ultrathin [Ni/Mn] samples and compared with the corresponding disordered $Ni_xMn_{100-x}$ alloy films on $Cu_3Au(001)$. For all samples our results revealed good epitaxial, layer-by-layer growth at a substrate temperature of 300 K. A weak c(2×2) superstructure was observed at the surface of the disordered $Ni_xMn_{100-x}$ alloy films, while it is sharper at the surface of ALF of [Ni/Mn]. The average perpendicular interlayer spacing of ALF is less than the one in corresponding disordered alloys, possibly caused by the buckling of the Mn and Ni atoms at the surface as well as in every grown layer. The ALF also shows stronger antiferromagnetism than corresponding disordered alloys.

We found that the structural properties are well connected to the magnetic ones and the decrease in interlayer spacing, which is attributed to long-range coherent growth of the ALF, strengthens the interlayer exchange coupling and causes enhanced exchange-bias field and coercivity in these films compared to the corresponding disordered alloy films.

# 6

# Magnetic properties of bilayers and trilayers of $Ni_xMn_{100-x}$ (x = 0, 25) in contact to ferromagnetic (Ni/) Co on $Cu_3Au(001)$

The appearance of perpendicular magnetization of an FM layer induced by adjacent AFM layers has drawn significant research interest in the area of magnetism especially in thin films. The reasons are its applicability to perpendicular magnetization-based logical devices [159–162] and the physics associated with the fundamental magnetic interactions in the bilayer and trilayer systems [163–169]. The crucial properties of perpendicular magnetic films, such as the corresponding coercivity and the magnitude of perpendicular magnetization, can be regulated by changing the relative thickness of FM or AFM layers [164, 170]. There is now a much more flexible means to control the perpendicular magnetic anisotropy (PMA) of magnetic thin films in magnetic devices desired for the modern magnetic recording industry [161, 171, 172]. In this chapter, with the help of MOKE measurements, we will unveil the AFM (Mn) nature that induces the perpendicular magnetization of an adjacent FM (Ni/Co) layer, irrespective of the growth temperature. A cover of Mn films that exhibit contracted fct-[vertical-to-in-plane lattice constant ratio (c/a) = 0.95] and expanded fct-like (c/a = 1.05) structures at different thickness levels induces in-plane magnetic anisotropy and PMA in Co/Ni films, respectively, confirming that the interlayer distance is a crucial parameter for establishing perpendicular magnetization. This finding presents the revitalized functionality of the AFM layer that has fundamentally been known for the coercivity enhancement and the occurrence of exchange bias phenomena for a long time.

## 6.1 Growth and structure of Mn on (Ni)/Co/$Cu_3$Au(001)

A number of MEED curves was recorded during Ni deposition, using either $Cu_3Au(001)$ or $Co/Cu_3Au(001)$ as substrates. Details have already been shown by Khan *et al.* [73,138]. Analysis of MEED curves has shown that the growth mode of $Ni/Co/Cu_3Au(001)$ is similar to that of Ni on $Cu_3Au(001)$ [73,138]. For nearly the same thickness, namely 12 ML of Ni on $Cu_3Au(001)$ and Ni on $Co/Cu_3Au(001)$, both show exactly the same interlayer distances and a very similar structure [73,138]. In this study, we investigated specifically the structural effects of ultrathin AFM films on the corresponding PMA they induce by comparing the crystalline structure and magnetic behaviors of epitaxially grown fct-like $Ni_xMn_{100-x}/Ni/Co/Cu_3Au(001)$ films. We observed a substantial modulation on the effect of the induced PMA, which occurred concurrently as the interlayer distance of the Mn films was changed and the thickness of the Mn films was varied. The findings provide clear experimental evidence that the interlayer distance of AFM films, which regulates the magnetic interaction between interfacial moments and moments within the volume, is a crucial parameter responsible for the induced PMA in AFM/FM films.

## 6.2 Results

The growth of AFM Mn on (Ni)/Co/$Cu_3$Au(001) at T=300 K or at 100 K was monitored by means of MEED. Figures 6.1 and 6.2 show selected LEED-specular spot I(V) curves and vertical interlayer distance ($d_p$), respectively, for the n ML Mn/5 ML Ni/5 ML Co films grown on $Cu_3Au(001)$. Mn films grown on Co/Ni bilayers, the $d_p$ value of thin Mn films (thickness of Mn films $t_{Mn} \leq 6$ ML) is 1.89 Å, similar for both RT and LT cases. Then, the $d_p$ value of the Mn films changes to approximately 1.71 Å, when $t_{Mn}$ is $\geq$ 12 ML. The crystalline structure of the Mn films can be conventionally classified on the basis of the ratio of the vertical and in-plane lattice constants (i.e., the c/a ratio). In the present study, Mn film c/a ratios close to either 0.95 or 1.05 indicate the presence of c-fct or e-fct structures. The presence of two metastable fcc-like phases on Mn films is consistent with the findings of previous experimental studies [137,168].

All the hysteresis loops are measured by longitudinal and polar MOKE for IP and OoP magnetized bilayers and trilayers, respectively. In this chapter from now on, mostly the lower and the upper FM layers will be called as FM1 and FM2, respectively. In some cases, like shown in Fig. 6.3 (c), two

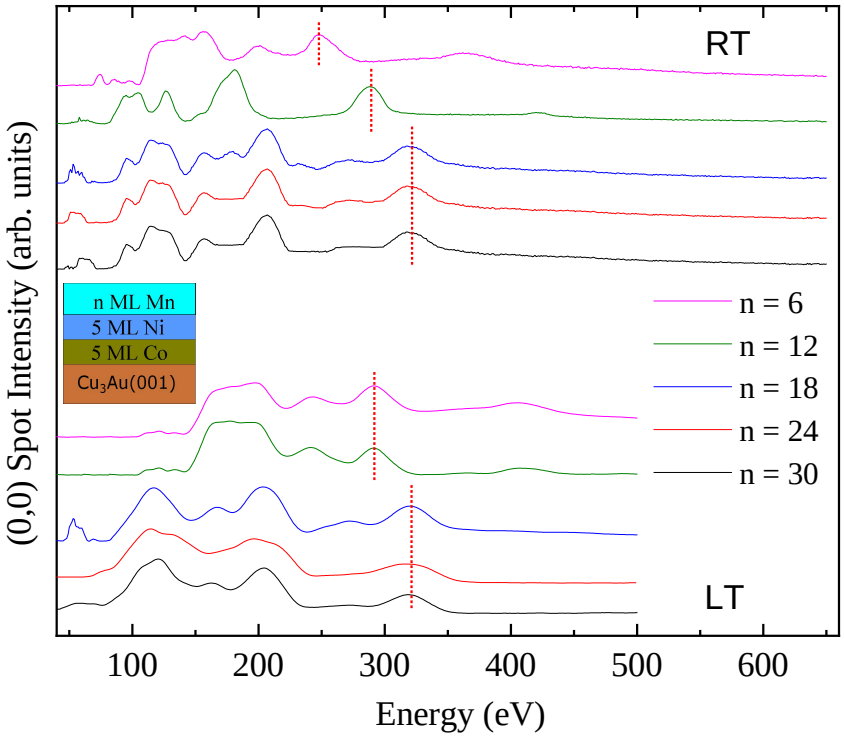


**Figure 6.1:** LEED-specular spot I(V) curves for various Mn films on the 5 ML Ni/5 ML Co/$Cu_3Au(001)$ films, grown and measured at 300 K (RT) and 100 K (LT). The red dashed bars label to each curve for for the 5th kinematic scattering peak.

different FM layers have been deposited one after the other (as FM1), making the total number of layers more than three. Despite this, we shall call our system 'trilayer'. A spin reorientation transition (SRT) has a key role in the magnetization direction of an FM and it mainly depends on the thickness of the FM layer. In previous works of Khan *et al.*, Ni has always OoP magnetization whether grown on $Cu_3Au(001)$ with thicknesses of 12–13 ML (FM1) below or on top of $Ni_xMn_{100-x}$ with thickness of 21–25 ML (FM2) at the upper interface [73,138]. To have the Ni magnetization in-plane (as FM1 or FM2) in the above-mentioned thickness regimes, 2–3 ML Co had been deposited either under the FM1 or on top of the FM2 Ni layer [73,138]. In our case the scenario is a bit different for the magnetization direction of 5 ML Ni on top of 5 ML Co on $Cu_3Au(001)$ and will be discussed in this chapter.

### 6.2.1 Bilayers

For a comparative study of IP versus OoP coupling in trilayers of type 2 samples shown in Fig. 6.3 (c), different FM films on top have been deposited on the two sides of the substrate, one side has shown an IP magnetization (10

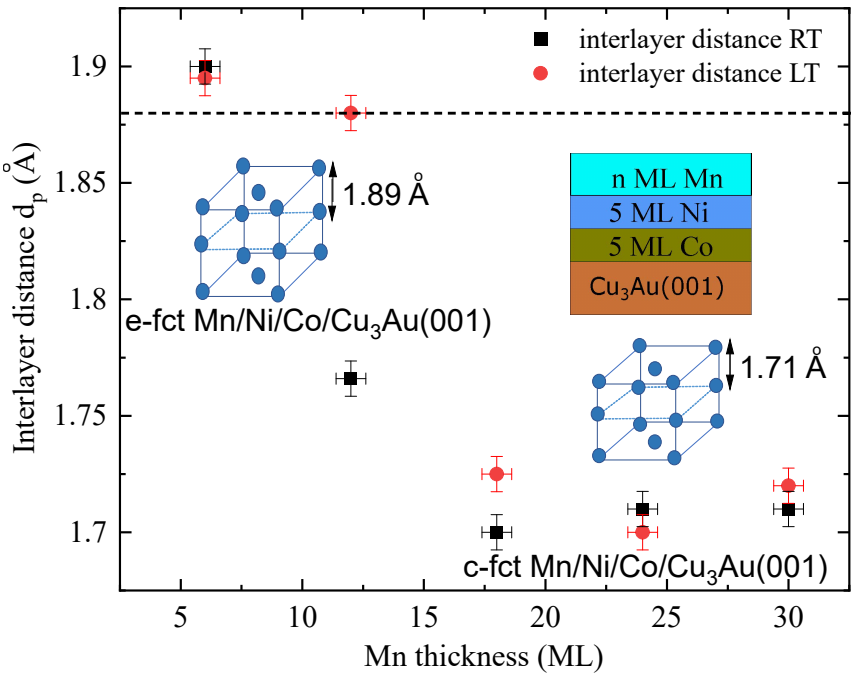


**Figure 6.2:** Average interlayer distance $d_p$ of various films calculated according to the kinematic peaks in the I(V) curves at RT and LT, respectively. $d_p$ of the Mn films changes from approximately 1.89 (e-fct Mn/Ni/Co/$Cu_3$Au(001)) to 1.71 Å (c-fct Mn/Ni/Co/$Cu_3$Au(001)) for thicknesses greater than 12 ML in both, the RT and LT case. The dashed line at 1.883 Å indicate the interlayer distance in fcc $Cu_3$Au(001).

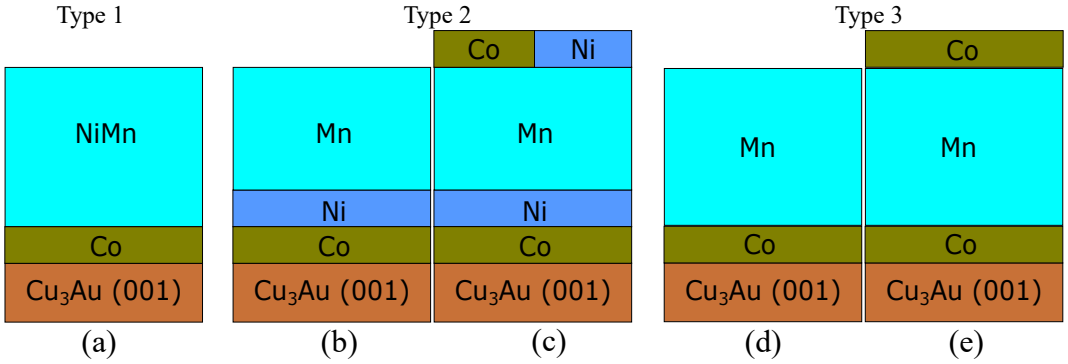


**Figure 6.3:** Schematic illustration of three types of samples of (FM2)/AFM/FM1 bilayer and trilayer systems that have been prepared.

ML Co/44 ML Mn/5 ML Ni/5 ML Co/$Cu_3$Au(001)) while the other side has an OoP magnetization (10 ML Ni/44 ML Mn/5 ML Ni/$Cu_3$Au(001)).

All the MOKE-measurements are done while " increasing the temperature

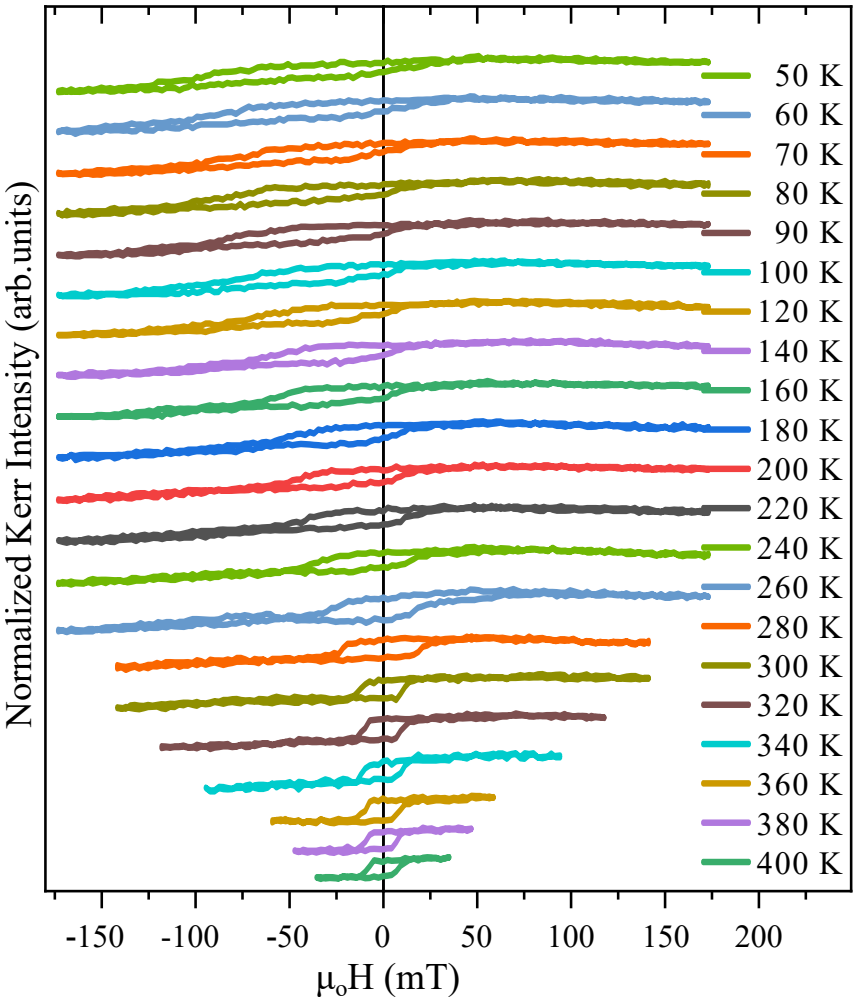


**Figure 6.4:** Normalized hysteresis loops for a 30 ML $Ni_{25}Mn_{75}$/10 ML Co/$Cu_3Au$(001) bilayer measured with longitudinal MOKE at different temperatures, deposited at room temperature.

from lower to higher values (not the other way around). All the samples under study in this chapter were field-cooled (FC) from 520 K (unless otherwise stated) in the FM layer magnetization direction of the respective probed interface. Samples were FC in the presence of a positive external magnetic field to get parallel alignment of the two FM layers. Due to the limited external magnetic field and the large $H_c$, the loop in the OoP configuration could only be observed above a certain temperature. That is why OoP measurements are started from higher temperatures compared to IP ones. The accuracy for the thickness measurement of Mn is within the error of around ±1 ML, for that of Ni is sub-ML and, for concentration of Ni(Mn) in $Ni_xMn_{100-x}$, it is less than ±2 %" [138].

Figure 6.4 shows an example of temperature-dependent hysteresis loops

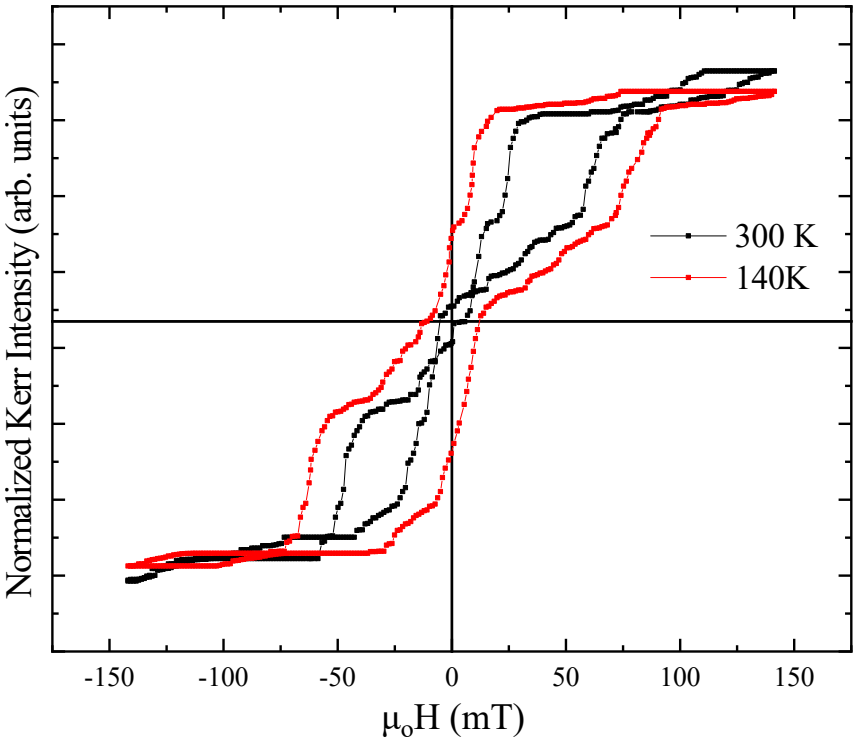


**Figure 6.5:** Normalized hysteresis loops for an as-prepared 30 ML $Ni_{25}Mn_{75}$/10 ML Co/$Cu_3Au$(001) bilayer measured with longitudinal MOKE at RT and at 140 K.

for 30 ML $Ni_{25}Mn_{75}$ on IP-magnetized Co, measured by longitudinal MOKE. The sample was deposited at room temperature; this applies from now on to all samples unless otherwise stated. One can see the temperature-dependent behavior of $H_c$ and $H_{eb}$ for the IP sample. The loops are clearly shifted to the negative side of the magnetic field axis at lower temperatures. "The exchange-biased loops are not of rectangular shape but rather tilted. At the blocking temperature ($T_b$), the temperature where EB finishes (here 280 K), the tilted shape of the hysteresis loops is changed to a more rectangular one. The reason for the tilted shape of the exchange-biased loops could be a locally different coupling strength at the interface of the bilayer. The higher the difference between the strength of the local uncompensated spins is, the more the loops are tilted " [138]. As the temperature is increased, $H_{eb}$ decreases for the sample, as expected. Exchange bias is observed for temperatures lower than 280 K. This shows that the 30 ML $Ni_{25}Mn_{75}$/10 ML Co bilayer under study provides weaker exchange bias as compared to 10 ML Co/30 ML $Ni_{25}Mn_{75}$, where exchange bias is observed for temperatures up to 400 K, as shown in chapter 4 (Fig. 4.7). The other difference is that in the former case, when measuring the as-grown bilayer before field cooling, one observes negative as well as pos-

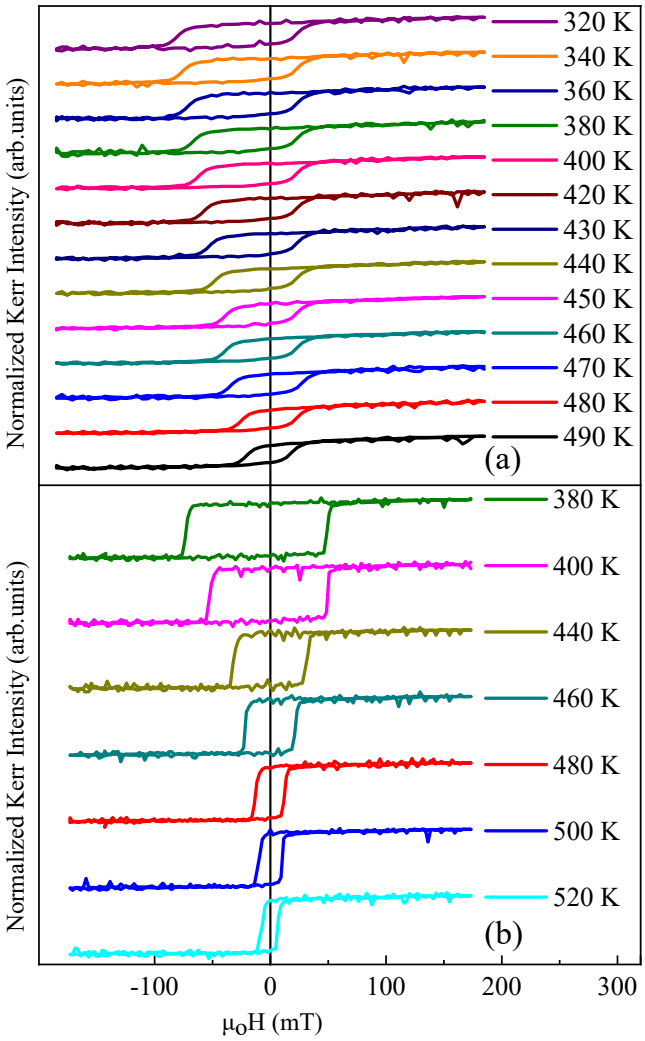


**Figure 6.6:** Normalized hysteresis loops for a 44 ML Mn/5 ML Ni/5 ML Co/$Cu_3Au$(001) bilayer measured with (a) longitudinal and (b) polar MOKE at different temperatures, deposited at room temperature.

itive EB shift shown in Fig. 6.5. "This is because the Co layer may exhibit domains with magnetization in different directions. This gives rise to the negative and to the positive shift simultaneously for the as-grown bilayer " [138], while in latter case we do not see this behavior at all. Similar results (both former and the latter) have been described in the work of Khan *et al.*, for NiMn/Ni/Co/$Cu_3Au$(001) [138].

An example of temperature-dependent hysteresis loops for both IP as well as OoP magnetization is shown in Fig. 6.6. Here we report on the experimental observations from a systematic study of the perpendicular exchange bias in the bilayers n ML Mn/5 ML Ni/5 ML Co on $Cu_3Au$(001) and the comparison

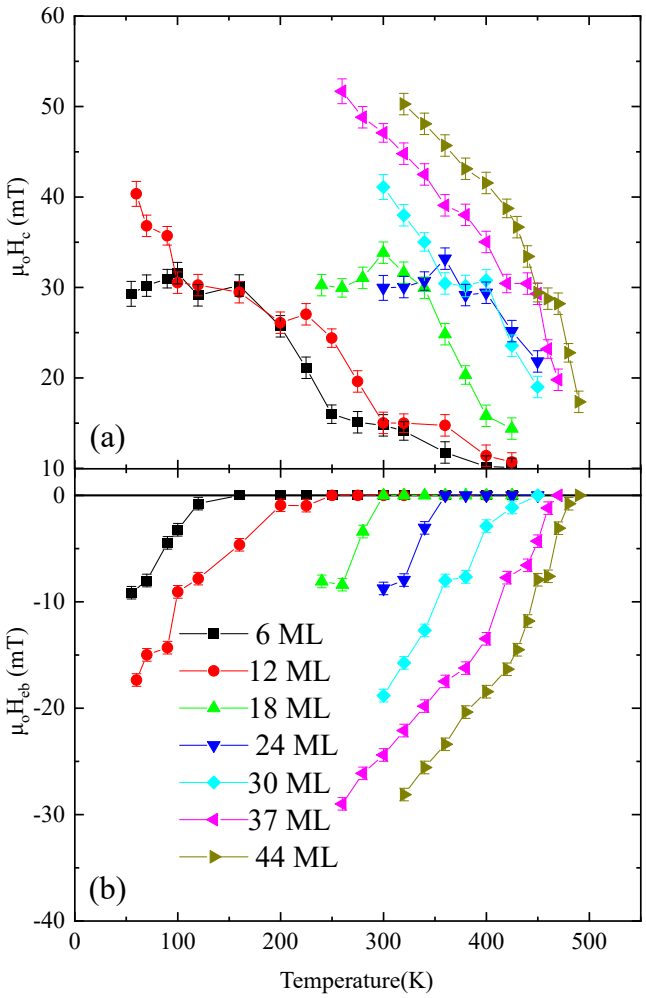


**Figure 6.7:** Temperature dependence of (a) coercivity and (b) exchange bias field for different thickness of IP magnetized bilayer Mn/5 ML Ni/5 ML Co/$Cu_3Au$(001). These bilayer films were deposited at room temperature.

with the corresponding longitudinal field cooling results. It is confirmed that perpendicular exchange bias can be established in AFM/FM bilayers when field-cooled along the surface normal direction. Such a behaviour is already reported in FeMn/(FeNi/FeMn)$_n$ [173]. Wang *et al.*, [164–166, 168–170] also show similar results in n ML Mn/1-3 ML Co/14 ML Ni/Cu (001). They have shown that Co/Ni films posses a weak in-plane magnetic anisotropy (IMA) and consequently changed to a PMA when the Mn films were further deposited, indicating that Mn films can induce a PMA on Co/Ni layers [164,165,168]. These results suggest that the PMA observed is possibly induced by the AFM Mn films through the AFM-FM exchange coupling, and this finding is consistent with those studies on FM/fcc-Mn and CoO/Ni bilayers [164, 167]. Slightly tilted loops for IP and rectangularly shaped loops for OoP were obtained,

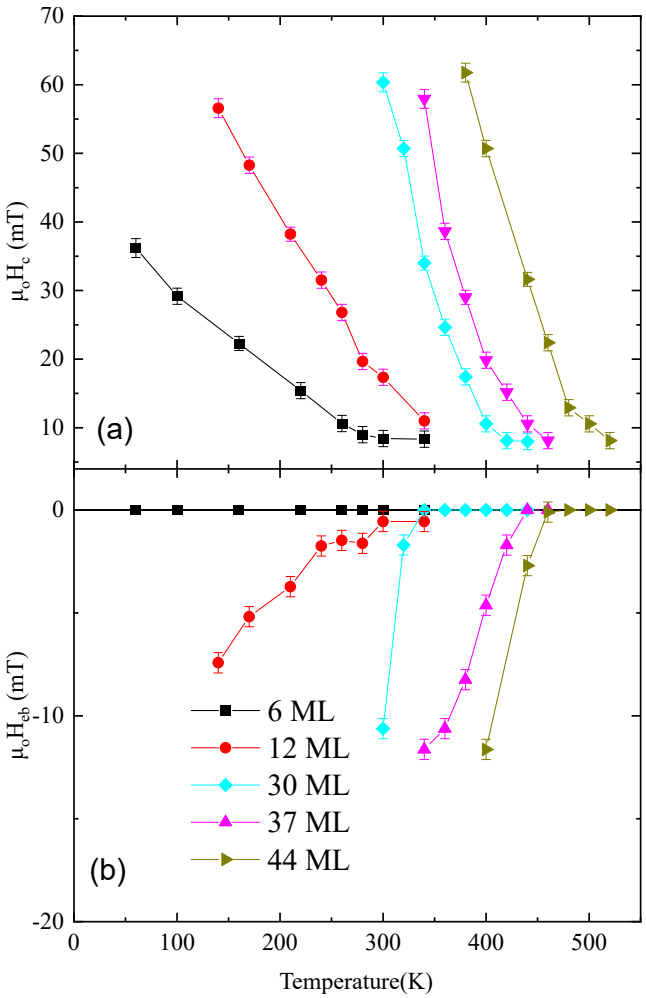


**Figure 6.8:** Temperature dependence of (a) coercivity and (b) exchange bias field for different thickness of OoP magnetized bilayer Mn/5 ML Ni/5 ML Co/$Cu_3Au$(001). These bilayer films were deposited at room temperature.

where a coercivity enhancement with decreasing temperature can be observed. Although the general behavior of the temperature-dependent hysteresis loops is similar for the IP and OoP cases, the details are different. The main differences between the two magnetization directions observed here are that the coercivity $H_c$ for OoP magnetization is bigger than that for IP magnetization at low temperatures, and that the reduction of $H_c$ to lower values occurs at higher temperatures for OoP magnetization. Then the two possibilities in this bilayer system could be that either we have grown Mn on type of FM1 (5 ML Ni/5 ML Co) which is close to a spin reorientation transition or it is the effect of the AFM (due to its thickness) on the FM, which enables to give us both IP as well as OoP magnetization [164–166, 168–170]. Otherwise a few ML of Co are enough to switch the Ni magnetization from OoP to IP [138].

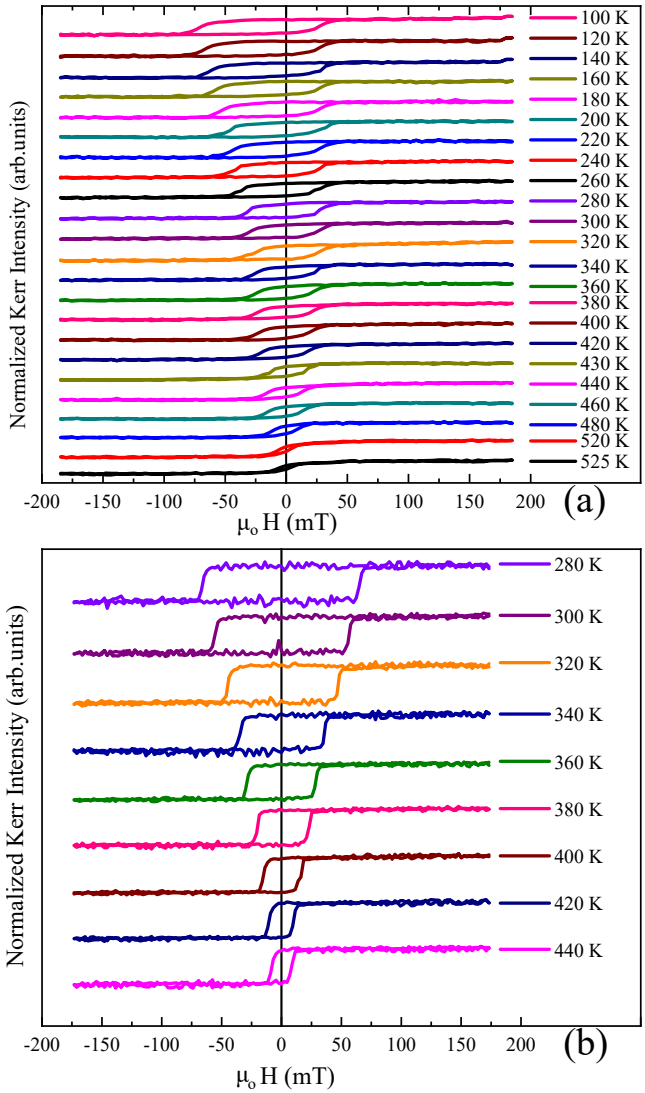


**Figure 6.9:** Normalized hysteresis loops for 44 ML Mn/5 ML Ni/5 ML Co/$Cu_3Au$(001) bilayer deposited at low temperature i.e., at 100 K measured with (a) longitudinal and (b) polar MOKE at different temperatures.

Figure 6.7 shows the temperature-dependent coercivity (a) and exchange bias field (b) for different thicknesses for Mn on 5 ML Ni/5 ML Co/$Cu_3Au$(001), obtained by longitudinal MOKE. These results reveal that the Mn thickness affects both the coercivity and the exchange bias field significantly. $T_b$, $T_N$ and $H_c$ become smaller with thinner Mn layer. Such kind of results are also reported in n ML Fe/m ML Mn/$Cu_3Au$(001) [137]. An other observation is that for larger Mn thickness, $T_b$ and $T_N$ are rather similar, while for smaller thickness, $T_b < T_N$.

Figure 6.8 shows the temperature-dependent coercivity (a) and exchange

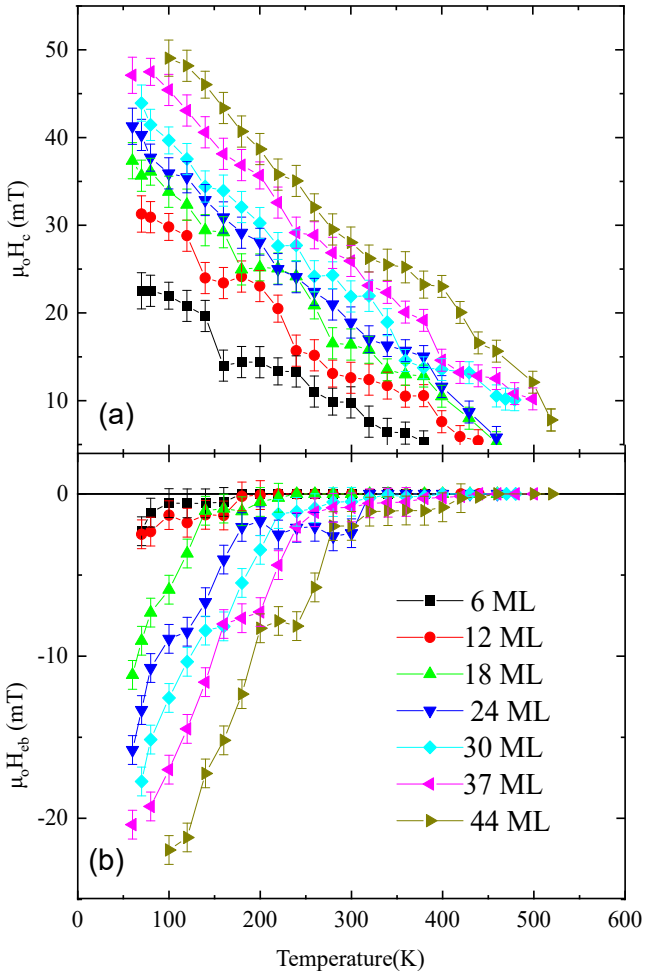


**Figure 6.10:** Temperature dependence of (a) coercivity and (b) exchange bias field for different thickness of IP magnetized bilayer Mn/5 ML Ni/5 ML Co/$Cu_3Au$(001), deposited at 100 K.

bias field (b) for different thicknesses of Mn on 5 ML Ni/5 ML Co/$Cu_3Au$(001), obtained by polar MOKE. These are the very same films shown in Fig. 6.7, which give IP as well as OoP loops. The results are similar but differ in details. Overall the results show that the Mn film thickness affects both the coercivity as well as the exchange bias field. $T_b$, $T_N$ and $H_c$ become higher with thicker Mn layer and in comparison to the IP part, the coercivities (especially at lower temperatures) are higher. Due to the unavailability of higher fields we were unable to measure at lower temperatures in this case.

Just like the film (shown in sketch 6.3 (b)) discussed in the last three paragraphs and prepared at room-temperature (RT), another film was reproduced and grown at 100 K. For this low-temperature (LT) grown sample, examples of temperature-dependent hysteresis loops for both IP as well as OoP magnetization are shown in Fig. 6.9. As a reminder, here the sample is 44 ML Mn/5

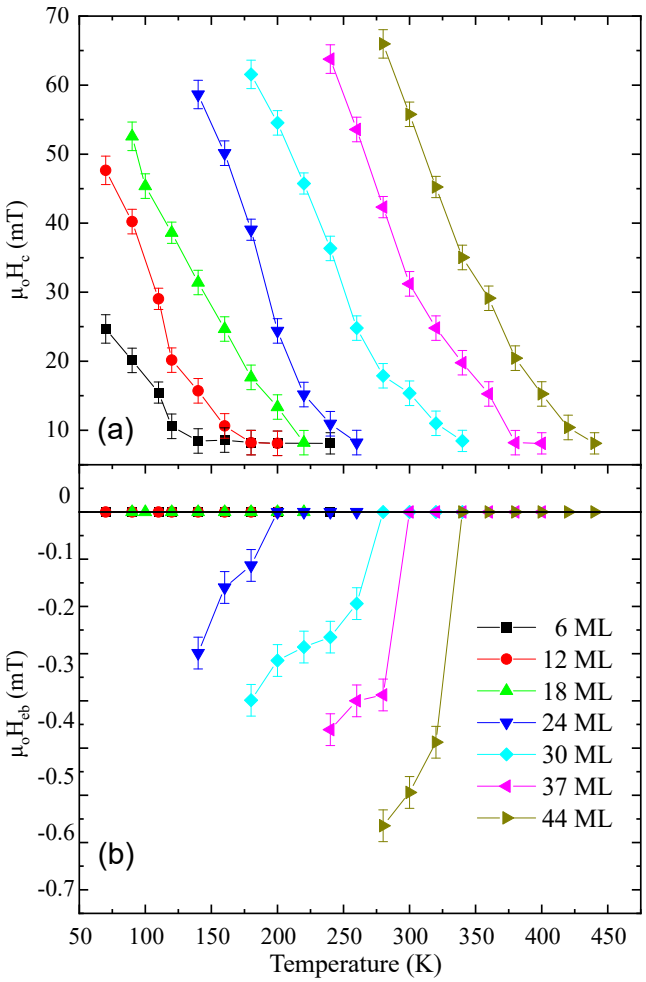


**Figure 6.11:** Temperature dependence of (a) coercivity and (b) exchange bias field for different thickness of OoP magnetized bilayer Mn/5 ML Ni/5 ML Co/$Cu_3Au$(001), deposited at 100 K

ML Ni/5 ML Co on $Cu_3Au$(001). Again, in analogy to the RT-grown sample, slightly tilted loops for IP and rectangularly shaped loops for OoP were obtained, where a coercivity enhancement with decreasing temperature can be observed, as expected. Although the general behavior of the temperature-dependent hysteresis loops is similar for the IP and OoP cases and also alike to the corresponding RT-grown sample, the details are different. The main differences between the two magnetization directions observed here (like in the RT-grown sample) are that the coercivity for OoP magnetization is bigger than that for IP magnetization, especially at low temperatures, and that the reduction of $H_c$ to lower values occurs at higher temperatures for OoP- as well as IP-magnetization compared to the RT-grown sample. The overall comparison of RT and LT samples shows that $T_b$, $T_N$, and $H_c$ are thickness- as well as growth-temperature-dependent in these samples. It will be discussed and

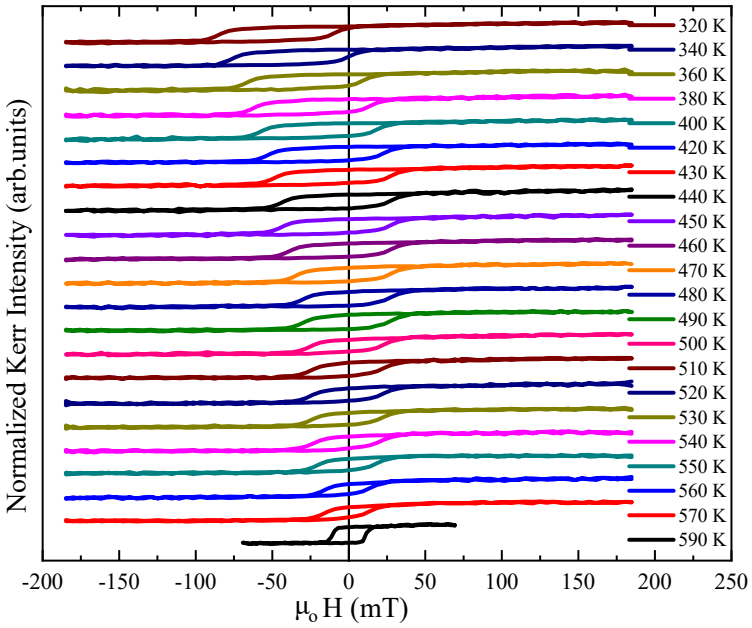


**Figure 6.12:** Normalized hysteresis loops for 44 ML Mn/10 ML Co/$Cu_3Au$(001) measured with longitudinal MOKE at different temperatures, deposited at room temperature.

clarified in the next two graphs.

Figure 6.10 shows the temperature-dependent coercivity (a) and exchange bias field (b) for different thicknesses of Mn on 5 ML Ni/5 ML Co/$Cu_3Au$(001), obtained by longitudinal MOKE grown at LT. These results show that the coercivity and the exchange bias field are film-thickness dependent. In comparison to the IP loops of the RT-grown sample, the behavior of the coercivity of the LT-grown sample is very systematic and does not show any saturation or jumps as the RT sample (for 18 and 24 ML thick Mn films in Fig. 6.7). In this LT-grown sample, $T_b$, $T_N$ and $H_c$ become larger with thicker Mn layer but all of them are smaller compared to the RT-grown sample. Such kind of results and behavior of Mn films are also reported for RT- and LT-grown n ML Fe/m ML Mn/$Cu_3Au$(001) samples [137].

Figure 6.11 shows the temperature-dependent coercivity (a) and exchange bias field (b) for different thicknesses of Mn on 5 ML Ni/5 ML Co/$Cu_3Au$(001), obtained by polar MOKE. Also the LT-grown samples give IP as well as OoP loops. The Mn film thickness affects both the coercivity and as well as the exchange bias field. $T_b$, $T_N$, and $H_c$ become higher with thicker Mn layer and in comparison to the IP results the coercivities (especially at lower temperatures) are higher. The coercivity, exchange bias field and $T_N$ are smaller overall in comparison to the RT-grown samples. For lower temperatures we were unable

to measure OoP loops due to limitations of the field. For the coercivity we do not see any saturation, which may occur at lower temperatures.

In parallel to the above two types of bilayer samples, also shown in Fig. 6.3 (a), and (b) (prepared at RT and LT), one more sample of similar thickness (44 ML) of the AFM i.e. Mn, in comparison to the second and third sample (depicted in Fig. 6.3 (b) prepared at RT and as well as LT) is deposited on 10 ML Co only (shown in Fig. 6.3 (d)). Fig. 6.12 shows temperature-dependent hysteresis loops for 44 ML Mn on IP magnetized Co, measured by longitudinal MOKE. The loops are clearly shifted to the negative side of the magnetic field axis at lower temperatures. This sample shows higher values of exchange bias compared to the other bilayer samples and details will be shown later together with its respective trilayer.

### 6.2.2 Trilayers

Figure 6.13 shows the temperature-dependent hysteresis loops for an IP-IP 10 ML Co/44 ML Mn/10 ML Co/$Cu_3Au$(001) trilayer sample. For all trilayers, both the FM1 and FM2 are parallely magnetized. From 60 up to 340 K in Fig. 6.13, the loops do not change much except that the exchange bias decreases with higher temperatures. Starting at 360 K, the loops split and two jumps of the magnetization are observed in each branch. For these two-step loops, the saturation field also increases. The reduced remanance at 460 K shows that it is due to an anti-parallel interlayer coupling between the two FM Co layers via the AFM Mn layer. The anti-parallel coupling slowly decreases with the rise in temperature and ceases at about 480 K. At this temperature, the coercivity reaches that of the individual Co layer and we define this temperature as the antiferromagnetic ordering temperature ($T_N$).

The corresponding bilayers of these samples, as discussed earlier, show magnetization in both directions, i.e. in IP as well as in OoP direction. For the trilayers grown at RT shown in Fig. 6.18 and Fig. 6.19 (see appendix), two kind of configurations are present in the two parts of the same sample, that is, at the one part, 10 ML Ni was evaporated and shows only OoP magnetization whereas on the other part, 10 ML Co was deposited and gives exclusively an IP magnetization. Recently Wang *et al.*, [174] have reported in a 12 ML Ni/2 ML Co/Mn/Co/Cu(001) trilayer that PMA can also be induced and controlled by varying the thickness of the bottom in-plane Co ultra-thin film. For FC, +100 mT external magnetic field was applied from 500 K. The loops are more tilted in the IP case than for the OoP magnetization, but if we compare to their respective bilayers, the loops are completely different in shape in case of OoP bilayers compared to the respective trilayers. In contrast to the rectangular

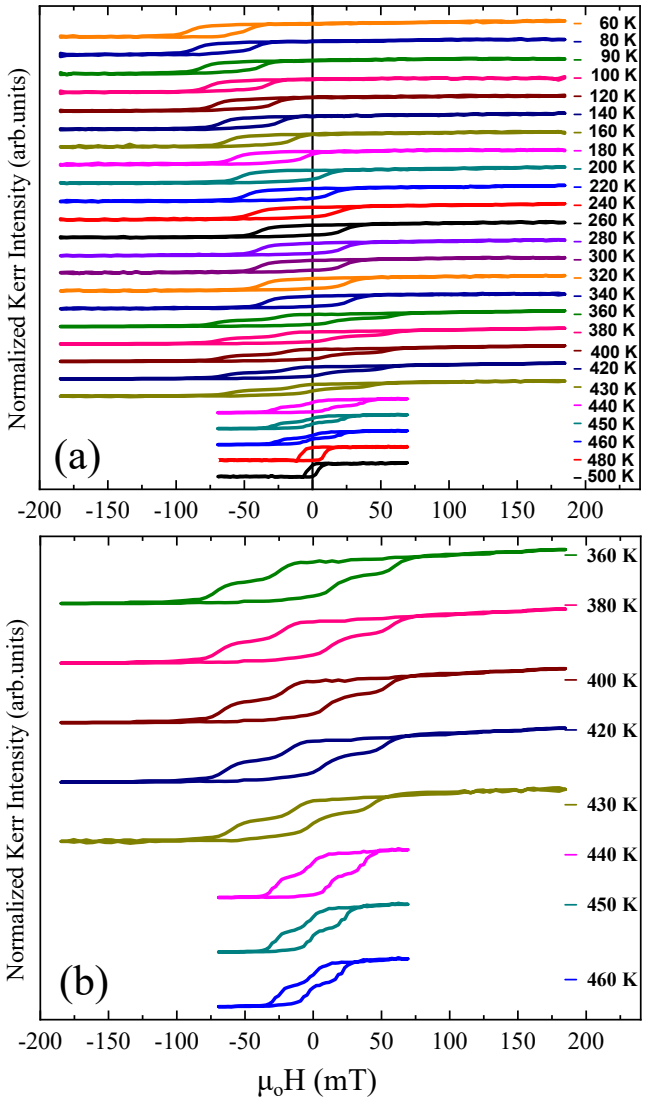


**Figure 6.13:** Normalized hysteresis loops for a 10 ML Co/44 ML Mn/10 ML Co/$Cu_3Au$(001) trilayer measured with (a) longitudinal MOKE at different temperatures, deposited at room temperature. (b) shows the magnification of double step loops between 360 K–460 K temperatures in (a).

shaped loops in bilayers, the corresponding trilayer shows tilted hysteresis loops.

Similar films as presented in Fig. 6.18 and Fig. 6.19 (see appendix) were also prepared at low temperature (100 K) shown in Fig. 6.14 and Fig. 6.15. In this sample, the loops at higher temperatures in the OoP case turn to more square-shape above 380 K. The coercivity in both Fig. 6.14 and Fig. 6.15 is smaller compared to the corresponding bilayers, more prominently at lower temperatures. The exchange bias field decreases in the LT-deposited trilayers,

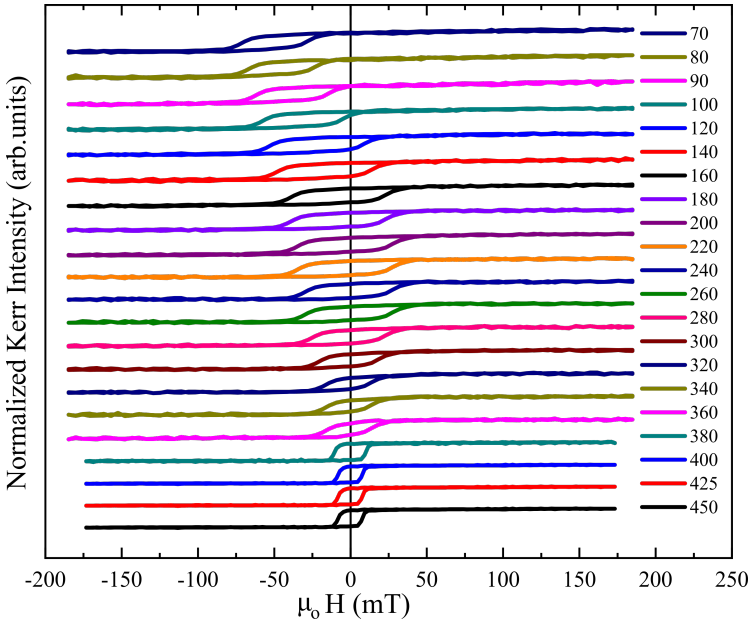


**Figure 6.14:** Normalized hysteresis loops for 10 ML Ni/44 ML Mn/5 ML Ni/5 ML Co/$Cu_3Au$(001) measured with polar MOKE at different temperatures, deposited at low temperature (100 K).

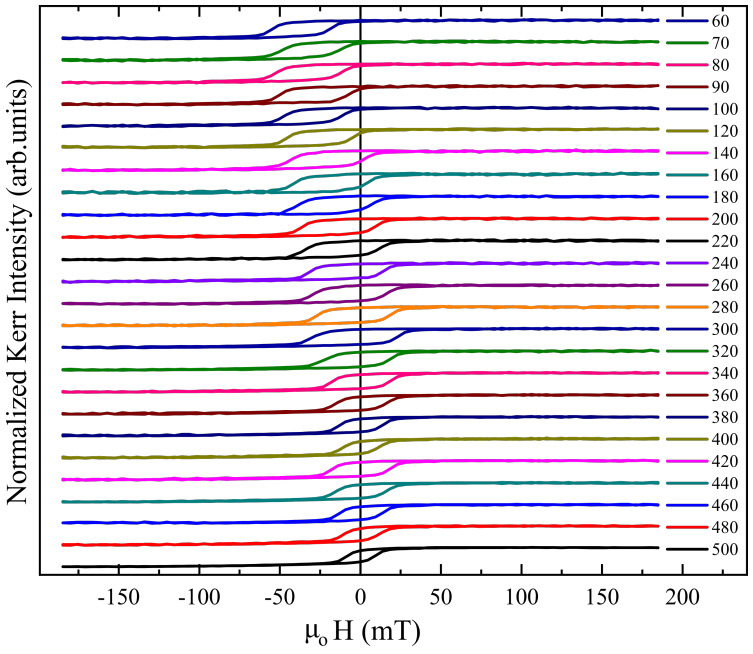


**Figure 6.15:** Normalized hysteresis loops for 10 ML Co/44 ML Mn/5 ML Ni/5 ML Co/$Cu_3Au$(001) measured with longitudinal MOKE at different temperatures, deposited at low temperature (100 K).

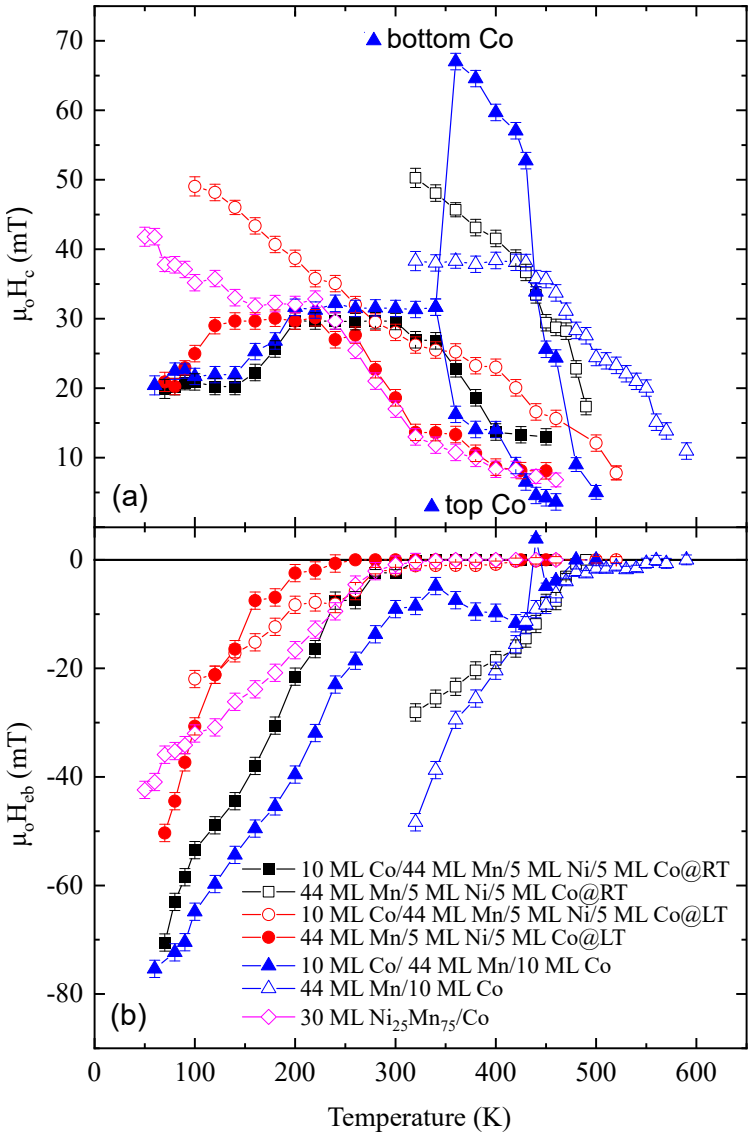


**Figure 6.16:** Comparison of (a) coercivity and (b) exchange bias field of IP-magnetized samples containing 44 ML thick Mn films deposited at different temperatures. 30 ML NiMn bilayer is shown only for completion and its trilayer has not been measured. 10 ML Co/44 Mn/10 ML Co shows double loops just above its blocking temperature. In this sample, the coercivity was evaluated for both minor loops and is labeled as coercivity of the top/bottom Co layer as FM2 and FM1 layers, respectively.

compared to the one grown at RT.

Figure 6.16 compares temperature-dependent curves for $H_c$ and the exchange-bias field of IP bilayers with their respective IP-magnetized trilayers. This 30 ML NiMn/Co bilayer is just plotted for the comparison of the three types of

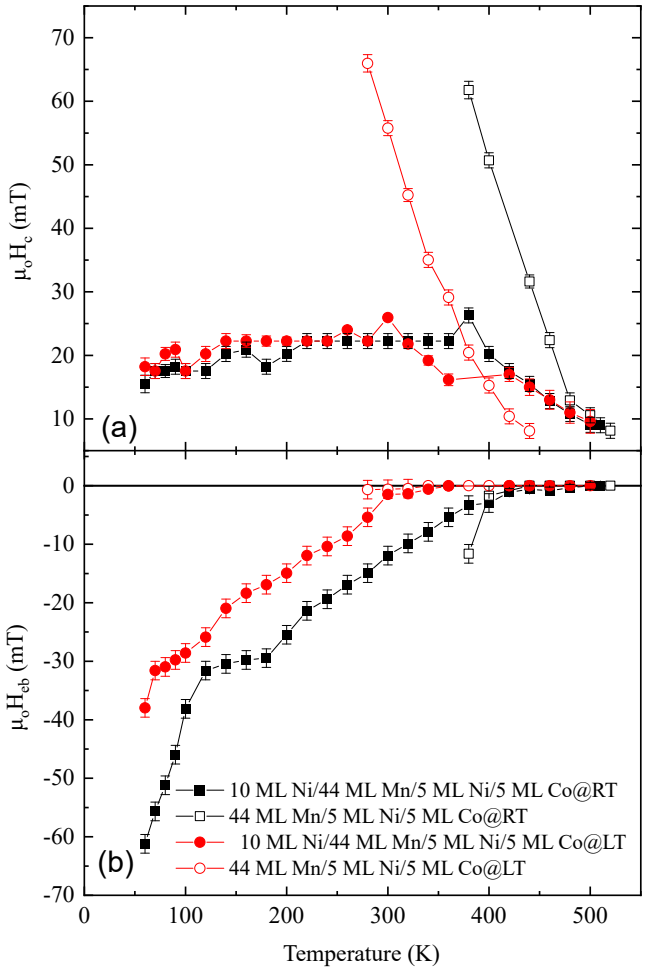


**Figure 6.17:** Comparison of (a) coercivity and (b) exchange bias field of OoP-magnetized bilayers containing 44 ML thick Mn films versus their corresponding trilayers, deposited at different temperatures.

.

samples discussed at the start of the chapter and the trilayer of this sample was not measured. In Fig. 6.16 for all cases the $T_N$ changes. For the bilayers, the $T_N$ occurs at slightly higher temperatures. The coercivity for all trilayers decreases compared to their corresponding bilayers (we are considering the average coercivity in the case of the 10 ML Co/44 ML Mn/10 ML Co trilayer). A similar trend is observed for the exchange-bias field, in all trilayers the value is smaller than in the bilayers. The $T_b$ comes at higher temperatures for bilayers than in the respective trilayers. The samewas observed for NiMn/(Ni)/Co/$Cu_3Au$(001) by Khan et. al [138]. So coercivity, exchange-bias field, $T_N$ and $T_b$ in this system depend on (i) the thickness of the AFM film as shown in Figs. 6.7, 6.8, 6.10, and 6.11, (ii) whether sample is a bilayer or a trilayer (as just discussed for the lower values in the trilayer

case) (iii) the growth temperature (the RT samples have higher values than the LT-evaporated sample), and finally (iv) the type (quality) of FM1 (which also dictates the above parameters). Similar results have been reported for RT- and LT-grown n ML Fe/m ML Mn/$Cu_3Au$(001) samples [137]. It should be noted that although the thickness of the $Ni_{25}Mn_{75}$ sample is not the same is in the other bilayer samples, it still shows higher values of the exchange-bias field (especially at higher temperatures) than the bilayer and trilayer sample grown at LT. The $Ni_{25}Mn_{75}$ bilayer shows two-step loops in the as-grown samples Fig. 6.5 and will be discussed in the next section. The trilayers with pure Co as FM1 show double-step loops (not observed in other trilayers where Ni/Co was used as FM1). Such a two-step behaviour was shown by Hagelschuer et. al. in Ni/NiMn/Ni/Cu(001) and by Zhang et. al. in Co/Mn/Co/Cu(001) [72, 175]. In the former case the double-step behaviour was mainly controlled with the AFM NiMn thickness: for an odd number of NiMn atomic layers it appeared, but not for an even number [72, 175]. In the latter case the double-step behavior was dictated by the FM1, a complete or integer number of monolayer of FM1 was showing this behavior, while a single-loop behavior was present in the case of half-filled layers of FM1 [72, 175].

Figure 6.17 shows the comparison of temperature-dependent curves for $H_c$ and the exchange-bias field of OoP bilayers and their respective OoP-magnetized trilayers grown at either LT or RT. In the OoP-magnetized component, similar to the IP-magnetized part, bilayers, whether grown at LT or RT, show a higher coercivity at lower temperatures than trilayers. The $T_N$ of both trilayers and the bilayer grown at RT shows same values, while for the bilayer grown at LT shows clearly smaller value of $T_N$ than its corresponding trilayer. In the RT-grown sample, the trend of exchange-bias field values is similar to the IP sample and bilayers show higher exchange-bias fields than trilayers, while for the sample grown at LT the case is contrary. Due to the unavailability of high magnetic fields we were unable to measure at lower temperatures in OoP-magnetized bilayer samples. Again the growth temperature of the sample plays a key role and the RT-grown sample shows higher exchange bias field than the LT sample.

## 6.3 Discussion

We have got the following main results for the discussion :

• **Successful growth of samples, varied by the FM1 or the AFM layer**

As shown in Fig. 6.3, three different types of samples were prepared. A two-

step magnetization reversal is observed in the as-grown IP bilayer samples of type 1 (Fig. 6.3 (a), for which the hysteresis loops are shown in Fig. 6.5) when measured along one of the two axes, because Co exhibits magnetic domains in opposite directions [138]. Therefore, the FM-layer domains with magnetization parallel (antiparallel) to the AFM layer pinned spins provide negative (positive) loop shift due to EB. This kind of simultaneous negative and positive shift has been also reported for a CrMn/Co bilayer [176]. Another experimental evidence for two different types of interfacial uncompensated Fe moments in an exchange-biased $Co/FeF_2$ bilayer has been reported where some moments are pinned and coupled parallel and some antiparallel to the FM layer [177].

The second type of bilayer samples, Fig. 6.3 (b), shows an unexpected result in terms that it shows an IP as well as OoP magnetization, whether grown at LT or RT. In contrast, the first and third type of samples (Fig. 6.3 (a) and (d)) show only IP magnetization, as expected. Normally a sub-monolayer Co on 15 ML Ni/Cu(001) is enough to pull the magnetization to in-plane, due to the strong shape anisotropy of Co. For not so clean vacuum, the out-of-plane anisotropy gets stronger, then maybe 2 ML Co is required [178]. Then possibly the reason for being somehow close to the spin reorientation transition in the present samples could be the effect of the Mn layer, which could play a role for the anisotropy.

The experimental curves shown in Figs. 6.7, 6.8, 6.10, and 6.11 clearly demonstrate remanance in both directions, in-plane and out-of-plane. This could mean that either it is a real canting (i.e., there is a minimum of the free energy at a canted angle between in-plane and out-of-plane), or that local minima of the free energy exist at both directions. In Co/FeMn on Cu(001) it has been observed previously that an FeMn layer, when it is antiferromagnetically ordered, changes the magnetization direction of Co from in-plane [110] to in-plane [100] [179]. But according to previous reports [166, 180], the strength of perpendicular magnetocrystalline anisotropy of magnetic films is linked to the out-of-plane $m_{orbital}/m_{spin}$ ratio [168]. Thus, a sizable out-of-plane $m_{orbital}/m_{spin}$ ratio for the uncompensated Mn moments in the n ML Mn/5 ML Ni/5 ML Co film could suggest the establishment of a high perpendicular crystalline anisotropy of these moments, as already reported in Mn/Co/Ni/Cu(001) [164–166, 168, 169, 174]. These uncompensated Mn moments at the FM/AFM interface are considered to be the origin of the PMA established in n ML Mn/5 ML Ni/5 ML Co films [164–166, 168, 169, 174]. An e-fct to c-fct transition was observed in the Mn films in Mn/5 ML Ni/5 ML $Co/Cu_3Au(001)$ with changing $t_{Mn}$. We thus suggest that the $d_p$ of Mn films is a crucial factor influencing the behavior of such films in inducing PMA in

adjacent FM layers.

The third type of bilayer sample, Fig. 6.3 (d), 44 ML Mn/Co/$Cu_3Au$(001) (Fig. 6.12) shows the highest $T_N$ and $T_b$ in comparison to the IP-magnetized bilayer films of the type 1 and 3 with identical Mn thickness Fig. 6.16. The same film was then sandwiched between IP-magnetized Co films and shows a temperature-induced change of the spin state of a Mn layer, Fig. 6.13. Below the ordering temperature $T_N$ of the AFM layer, a strong antiparallel coupling between the two FM layers is evident from Fig. 6.13. Below a certain temperature, this interlayer coupling suddenly disappears. This is interpreted as a temperature-driven spin-reorientation transition of the AFM spin structure, which affects the magnetic coupling at the AFM/FM interface.

• **LT and RT-grown samples**

To understand more about the second type of samples Fig. 6.3 (b-c), they were reproduced under exactly the same conditions but at different growth temperature (100 K). But the curiosity remained the same, these LT-prepared samples show exactly the same IP as well as OoP magnetization direction, simultaneously. We see definitely a slight decrease in the values of coercivity, exchange-bias field, $T_N$, and $T_b$ in the LT-grown samples, as has been observed also in Fe/Mn/$Cu_3Au$(001) [137] and the change in properties within different-temperature-grown samples was related to structural and morphological changes. The roughness increases in the sample prepared at low temperature, which causes them to have an earlier structural transition than the RT-prepared samples as a function of Mn thickness [137].

## 6.4 Conclusion

We have observed double-shifted loops in as-prepared $Ni_{25}Mn_{75}$/Co bilayers. This double-shift loop is assumed to be due to the coexistence of positive and negative exchange bias. We also systematically investigated the structural and magnetic properties of AFM thin films with respect to antiferromagnet-induced PMA in epitaxially grown fct-like Mn/Ni/Co/$Cu_3Au$(001) films. The investigation results improve the understanding of the phenomenon of AFM-induced PMA in AFM/FM layers and can facilitate the development of next-generation perpendicular-based spintronic devices that exploit the crystalline structures of ultrathin AFM layers. Significant exchange bias is observed in RT-Mn/Ni/Co bilayers, both in IP and OoP directions simultaneously, which increases with Mn thickness. The exchange bias coupling in LT-Mn/Ni/Co bilayers is much weaker than that in RT-Mn/Ni/Co and drastically varies

with Mn film thickness due to the enhanced roughness in LT-grown films.

Ultrathin AFM Mn films sandwiched between in-plane-magnetized Co layers on $Cu_3Au(001)$ show a transition in the spin structure at a temperature between the blocking temperature for exchange-bias and the antiferromagnetic ordering temperature. The spin structure present above this transition temperature leads to a significant antiparallel interlayer coupling. This is mediated by direct exchange coupling through the AFM spin structure, which disappears at $T_N$. Exploiting the transition of the spin structure could be a way of controlling the magnetic properties of a multilayered magnetic system by taking advantage of the sudden onset of interlayer coupling, the corresponding jump in coercivity, or the change in the AFM spin structure itself.

# Bibliography


[1] J. F. Gregg, I. Petej, E. Jouguelet, and C. Dennis: *Spin electronics—a Review*. Journal of Physics D: Applied Physics **35**, R121 (2002).

[2] G. A. Prinz: *Magnetoelectronics*. Science **282**, 1660–1663 (1998).

[3] M. Ziese: *Spin transport in semiconductors*. in: Spin Electronics, Springer (2001).

[4] J. L. Simonds: *Magnetoelectronics today and tomorrow.*. Physics Today **48**, 26–32 (1995).

[5] N. Farzad and N. Alain: *Nanomagnetism and spintronics: fabrication, materials, characterization and applications*. World Scientific (2010).

[6] S. S. P. Parkin, K. P. Roche, M. G. Samant, P. M. Rice, R. B. Beyers, R. E. Scheuerlein, E. J. O'sullivan, S. L. Brown, J. Bucchigano, D. W. Abraham, et al.: *Exchange-biased magnetic tunnel junctions and application to nonvolatile magnetic random access memory*. Journal of Applied Physics **85**, 5828–5833 (1999).

[7] J. M. Daughton: *Magnetic tunneling applied to memory*. Journal of Applied Physics **81**, 3758–3763 (1997).

[8] J. M. Daughton: *Magnetoresistive memory technology*. Thin Solid Films **216**, 162–168 (1992).

[9] S. Tehrani, E. Chen, M. Durlam, M. DeHerrera, J. M. Slaughter, J. Shi, and G. Kerszykowski: *High density submicron magnetoresistive random access memory*. Journal of Applied Physics **85**, 5822–5827 (1999).

[10] J. Lohau, A. Moser, C. T. Rettner, M. E. Best, and B. D Terris: *Effect of ion beam patterning on the write and read performance of perpendicular granular recording media*. IEEE Transactions on Magnetics **37**, 1652–1656 (2001).

[11] S. Sun, C. B. Murray, D. Weller, L. Folks, and A. Moser: *Monodisperse FePt nanoparticles and ferromagnetic FePt nanocrystal superlattices*. Science **287**, 1989–1992 (2000).

[12] C. A. Ross: *Patterned magnetic recording media.* Annual Review of Materials Research **31**, 203–235 (2001).

[13] M. N. Baibich, J.M. Broto, A. Fert, F. N. V. Dau, F. Petroff, and P. Etienne: *g. Creuzet, A. Friederich, and J. Chazelas.* Physical Review Letters **61**, 2472 (1988).

[14] G. Binasch, P. Grünberg, F. Saurenbach, and W. Zinn: *Enhanced magnetoresistance in layered magnetic structures with antiferromagnetic interlayer exchange.* Physical Review B **39**, 4828 (1989).

[15] R. E Camley and J. Barnaś: *Theory of giant magnetoresistance effects in magnetic layered structures with antiferromagnetic coupling.* Physical Review Letters **63**, 664 (1989).

[16] J. Barnaś, A. Fuss, R. E. Camley, P. Grünberg, and W. Zinn: *Novel magnetoresistance effect in layered magnetic structures: Theory and experiment.* Physical Review B **42**, 8110 (1990).

[17] R. Q Hood and L. M. Falicov: *Boltzmann-equation approach to the negative magnetoresistance of ferromagnetic–normal-metal multilayers.* Physical Review B **46**, 8287 (1992).

[18] P. Grünberg, R. Schreiber, Y. Pang, M.B. Brodsky, and H. Sowers: *Layered magnetic structures: Evidence for antiferromagnetic coupling of Fe layers across Cr interlayers.* Physical Review Letters **57**, 2442 (1986).

[19] S. S. P. Parkin, N. More, and K. P. Roche: *Oscillations in exchange coupling and magnetoresistance in metallic superlattice structures: Co/Ru, Co/Cr, and Fe/Cr.* Physical Review Letters **64**, 2304 (1990).

[20] M. T. Johnson, S. T. Purcell, N. W. E. McGee, R. Coehoorn, J. A. D. Stegge, and W. Hoving: *Structural dependence of the oscillatory exchange interaction across Cu layers.* Physical Review Letters **68**, 2688 (1992).

[21] T Shinjo: *Magnetic Properties of Interfaces and Magnetoresistance in Multilayers.* in: Ordering at Surfaces and Interfaces: Proceedings of the Third NEC Symposium Hakone, Japan, October 7–11, 1990, p. 305 (2012).

[22] Y. Wu, K. Li, J. Qiu, Z. Guo, and G. Han: *Antiferromagnetically coupled hard/Ru/soft layers and their applications in spin valves.* Applied Physics Letters **80**, 4413–4415 (2002).

[23] T. Ono and T. Shinjo: *Magnetoresistance of multilayers prepared on microstructured substrates*. Journal of the Physical Society of Japan **64**, 363–366 (1995).

[24] M. L. Reed, N. A. El-Masry, H. H. Stadelmaier, M. K. Ritums, M. J . Reed, C. A. Parker, J. C. Roberts, and S. M. Bedair: *Room temperature ferromagnetic properties of (Ga, Mn)N*. Applied Physics Letters **79**, 3473–3475 (2001).

[25] T. Sasaki, S. Sonoda, Y. Yamamoto, K. Suga, S. Shimizu, K. Kindo, and H. Hori: *Magnetic and transport characteristics on high Curie temperature ferromagnet of Mn-doped GaN*. Journal of Applied Physics **91**, 7911–7913 (2002).

[26] G. A. Medvedkin, T. Ishibashi, T. Nishi, K. Hayata, Y. Hasegawa, and K. Sato: *Room temperature ferromagnetism in novel diluted magnetic semiconductor* $Cd_{1-x}Mn_xGeP_2$. Japanese Journal of Applied Physics **39**, L949 (2000).

[27] N. Theodoropoulou, A. F. Hebard, M. E. Overberg, C. R. Abernathy, S. J. Pearton, S. N. G. Chu, and R. G. Wilson: *Unconventional carrier-mediated ferromagnetism above room temperature in ion-implanted (Ga, Mn) P: C*. Physical Review Letters **89**, 107203 (2002).

[28] Y. Matsumoto, M. Murakami, T. Shono, T. Hasegawa, T. Fukumura, M. Kawasaki, P. Ahmet, T. Chikyow, S. Koshihara, and H. Koinuma: *Room-temperature ferromagnetism in transparent transition metal-doped titanium dioxide*. Science **291**, 854–856 (2001).

[29] K. Ueda, H. Tabata, and T. Kawai: *Magnetic and electric properties of transition-metal-doped ZnO films*. Applied Physics Letters **79**, 988–990 (2001).

[30] M. Tanaka and Y. Higo: *Large tunneling magnetoresistance in GaMnAs/AlAs/GaMnAs ferromagnetic semiconductor tunnel junctions*. Physical Review Letters **87**, 026602 (2001).

[31] M. Tanaka: *Ferromagnet (MnAs)/III–V semiconductor hybrid structures*. Semiconductor Science and Technology **17**, 327 (2002).

[32] G. A. Prinz: *Spin-polarized transport*. Physics Today **48**, 58–63 (1995).

[33] R. Fiederling, M. Keim, G. al Reuscher, W. Ossau, G. Schmidt, A. Waag, and L. W. Molenkamp: *Injection and detection of a spin-polarized current in a light-emitting diode*. Nature **402**, 787–790 (1999).

[34] T. Fujisawa, D. Guy Austing, Y. Tokura, Y. Hirayama, and S. Tarucha: *Allowed and forbidden transitions in artificial hydrogen and helium atoms*. Nature **419**, 278–281 (2002).

[35] Sh. Yuasa, T. Nagahama, A. Fukushima, Yo. Suzuki, and K. Ando: *Giant room-temperature magnetoresistance in single-crystal Fe/MgO/Fe magnetic tunnel junctions*. Nature Materials **3**, 868–871 (2004).

[36] H. Ohno, D. Chiba, F. Matsukura, T. Omiya, E. Abe, T. Dietl, Y. Ohno, and K. Ohtani: *Electric-field control of ferromagnetism*. Nature **408**, 944–946 (2000).

[37] Su. Datta and B. Das: *Electronic analog of the electro-optic modulator*. Applied Physics Letters **56**, 665–667 (1990).

[38] D. J. Monsma, J. C. Lodder, T. J. Popma, and B. Dieny: *Perpendicular hot electron spin-valve effect in a new magnetic field sensor: The spin-valve transistor*. Physical Review Letters **74**, 5260 (1995).

[39] T. Hayashi, H. Shimada, H. Shimizu, and M. Tanaka: *Tunneling spectroscopy and tunneling magnetoresistance in (GaMn)As ultrathin heterostructures*. Journal of Crystal Growth **201-202**, 689–692 (1999).

[40] D. Chiba, N. Akiba, F. Matsukura, Y. Ohno, and H. Ohno: *Magnetoresistance effect and interlayer coupling of (Ga, Mn)As trilayer structures*. Applied Physics Letters **77**, 1873 (2000).

[41] I. Žutić, J. Fabian, and S. D. Sarma: *Spintronics: Fundamentals and applications*. Reviews of Modern Physics **76**, 323–410 (2004).

[42] M. Johnson, B. R. Bennett, M. J. Yang, M. M. Miller, and B. V. Shanabrook: *Hybrid Hall effect device*. Applied Physics Letters **71**, 974–976 (1997).

[43] S. V. Dijken, X. Jiang, and S. S. P. Parkin: *Room temperature operation of a high output current magnetic tunnel transistor*. Applied Physics Letters **80**, 3364–3366 (2002).

[44] S. Franchi: *Molecular beam epitaxy: fundamentals, historical background and future prospects*. in: Molecular Beam Epitaxy, Elsevier (2013).

[45] T. Shinjo: *Interface magnetism*. Surface Science Reports **12**, 51–98 (1991).

[46] L. Breth: *Detection of weak magnetic fields : the TMR fluxgate sensing technology and its limits*. Ph. D. thesis, Vienna University of Technology (Austria), (2016).

[47] J. Nogués and I. K. Schuller: *Exchange bias*. Journal of Magnetism and Magnetic Materials **192**, 203–232 (1999).

[48] A. E. Berkowitz and K. Takano: *Exchange anisotropy — a review*. Journal of Magnetism and Magnetic Materials **200**, 552–570 (1999).

[49] R. L. Stamps: *Mechanisms for exchange bias*. Journal of Physics D: Applied Physics **33**, R247–R268 (2000).

[50] M. Kiwi: *Exchange bias theory*. Journal of Magnetism and Magnetic materials **234**, 584–595 (2001).

[51] M. Jimbo: *Present status of antiferromagnetic materials in spin valves*. Journal-Magnetics Society of Japan **22**, 12–18 (1998).

[52] M. Lederman: *Performance of metallic antiferromagnets for use in spin-valve read sensors*. IEEE Transactions on Magnetics **35**, 794–799 (1999).

[53] T. Lin, C. Tsang, R. E. Fontana, and J. K. Howard: *Exchange-coupled Ni-Fe/Fe-Mn, Ni-Fe/Ni-Mn and NiO/Ni-Fe films for stabilization of magnetoresistive sensors*. IEEE Transactions on Magnetics **31**, 2585–2590 (1995).

[54] T. Lin, D. Mauri, N. Staud, C. Hwang, J. Kent Howard, and G. L. Gorman: *Improved exchange coupling between ferromagnetic Ni-Fe and antiferromagnetic Ni-Mn-based films*. Applied Physics Letters **65**, 1183–1185 (1994).

[55] A. J. Devasahayam and M. H. Kryder: *Biasing materials for spin-valve read heads*. IEEE Transactions on Magnetics **35**, 649–654 (1999).

[56] G. W. Anderson, Y. Huai, and M. Pakala: *Spin-valve thermal stability: The effect of different antiferromagnets*. Journal of Applied Physics **87**, 5726–5728 (2000).

[57] Z. Qian, J. M. Sivertsen, J. H. Judy, B. A. Everitt, S. Mao, and E. S. Murdock: *Exchange coupling of radio frequency sputtered NiMn/NiFe and NiFe/NiMn bilayers*. Journal of Applied Physics **85**, 6106–6108 (1999).

[58] S. Soeya, S. Tadokoro, T. Imagawa, M. Fuyama, and S. Narishige: *Magnetic exchange coupling for bilayered $Ni_{81}Fe_{19}/NiO$ and trilayered $Ni_{81}Fe_{19}/NiFeNb/NiO$ films*. Journal of Applied Physics **74**, 6297–6301 (1993).

[59] M. J. Carey and A. E. Berkowitz: *Exchange anisotropy in coupled films of $Ni_{81}Fe_{19}$ with NiO and $Co_xNi_{1-x}O$*. Applied Physics Letters **60**, 3060–3062 (1992).

[60] J. P. Nozières, S. Jaren, Y. B. Zhang, A. Zeltser, K. Pentek, and V. S. Speriosu: *Blocking temperature distribution and long-term stability of spin-valve structures with Mn-based antiferromagnets.* Journal of Applied Physics **87**, 3920–3925 (2000).

[61] A. Veloso, P. P Freitas, N. J. Oliveira, J. Fernandes, and M. Ferreira: *Spin valve heads with a corrosion resistant MnRh exchange layer.* IEEE Transactions on Magnetics **34**, 2343–2347 (1998).

[62] M. Saito, Y. Kakaihara, T. Watanabe, and N. Hasegawa: *Exchange coupling between antiferromagnetic PtMn and ferromagnetic film.* Journal-Magnetics Society of Japan **21**, 505–508 (1997).

[63] M. Sano, S. Araki, M. Ohta, K. Noguchi, H. Morita, and M. Matsuzaki: *Exchange coupling and GMR properties in ion beam sputtered hematite spin-valves.* IEEE Transactions on Magnetics **34**, 372–374 (1998).

[64] S. Soeya, Hi. Hoshiya, M. Fuyama, and S. Tadokoro: *Exchange coupling between ferromagnetic fcc $Ni_{81}Fe_{19}$ and antiferromagnetic bcc CrMnPt films.* Journal of Applied Physics **80**, 1006–1011 (1996).

[65] S. Bae, J. H. Judy, P. J. Chen, W. F. Egelhoff Jr., and S. Zurn: *High thermal stability of exchange-biased bilayers and bottom giant magnetoresistive spin valves using an $\alpha$-$Fe_2O_3$ antiferromagnetic layer.* Applied Physics Letters **78**, 4163–4165 (2001).

[66] E. Krén, E. Nagy, I. Nagy, L. Pál, and P. Szabó: *Structures and phase transformations in the MnNi system near equiatomic concentration.* Journal of Physics and Chemistry of Solids **29**, 101–108 (1968).

[67] B. Dai, J. W. Cai, W. Y. Lai, F. Shen, Z. Zhang, and G. H. Yu: *Approach to optimize the pinning effect of a NiMn layer with reduced thickness under a much shortened annealing process.* Applied Physics Letters **82**, 3722–3724 (2003).

[68] J. S. Kasper and J. S. Kouvel: *The antiferromagnetic structure of NiMn.* Journal of Physics and Chemistry of Solids **11**, 231–238 (1959).

[69] C. L. Gao, A. Ernst, A. Winkelmann, J. Henk, W. Wulfhekel, P. Bruno, and J. Kirschner: *Noncollinear surface spin density by surface reconstruction in the alloy NiMn.* Physical Review Letters **100**, 237203 (2008).

[70] M. Y. Khan, C. B. Wu, M. Erkovan, and W. Kuch: *Probing antiferromagnetism in NiMn/Ni/(Co)/$Cu_3$Au(001) single-crystalline epitaxial thin films.* Journal of Applied Physics **113**, 023913 (2013).

[71] W. A. A. Macedo, P. L. Gastelois, Maximiliano D. Martins, W. Kuch, J. Miguel, and M. Y. Khan: *Growth, structure, and magnetic properties of epitaxial $Ni_xMn_{100-x}$ single layers and $Co/Ni_xMn_{100-x}$ bilayers on $Cu_3Au(100)$.* Physical Review B **82**, 134423 (2010).

[72] T. Hagelschuer, Y. A. Shokr, and W. Kuch: *Spin-state transition in antiferromagnetic $Ni_{0.4}Mn_{0.6}$ films in Ni/NiMn/Ni trilayers on Cu(001).* Physical Review B **93**, 054428 (2016).

[73] M. Y. Khan, C. B. Wu, S. K. Kreft, and W. Kuch: *Concentration- and thickness-dependent magnetic properties of $Ni_xMn_{100-x}$ in epitaxially grown $Ni_xMn_{100-x}/Ni/(Co/)Cu_3Au(001)$.* Journal of Physics: Condensed Matter **25**, 386005 (2013).

[74] M. Erkovan, Y. A. Shokr, D. Schiestl, C. B. Wu, and W. Kuch: *Influence of $Ni_xMn_{1-x}$ thickness and composition on the Curie temperature of Ni in $Ni_xMn_{1-x}/Ni$ bilayers on $Cu_3Au(001)$.* Journal of Magnetism and Magnetic Materials **373**, 151–154 (2015).

[75] M. Y. Khan, Y. A. Shokr, and W. Kuch: *Coupling of pinned magnetic moments in an antiferromagnet to a ferromagnet and its role for exchange bias.* Journal of Physics: Condensed Matter **32**, 075801 (2019).

[76] M. Y. Khan, C. B. Wu, W. Kuch, et al.: *Pinned magnetic moments in exchange bias: Role of the antiferromagnetic bulk spin structure.* Physical Review B **89**, 094427 (2014).

[77] Y. A. Shokr, M. Erkovan, C. B. Wu, B. Zhang, O. Sandig, and W. Kuch: *Temperature-induced sign change of the magnetic interlayer coupling in $Ni/Ni_{25}Mn_{75}/Ni$ trilayers on $Cu_3Au(001)$.* Journal of Applied Physics **117**, 175302 (2015).

[78] L. Ding, P. F. Ladwig, X. Yan, and Y. A. Chang: *Thermodynamic stability and diffusivity of near-equiatomic Ni–Mn alloys.* Applied Physics Letters **80**, 1186–1188 (2002).

[79] L. Pál, E. Krén, G. Kádár, P. Szabó, and T. Tarnóczi: *Magnetic Structures and Phase Transformations in Mn-Based CuAu-I Type Alloys.* Journal of Applied Physics **39**, 538–544 (1968).

[80] A. Sakuma: *Electronic structures and magnetism of CuAu-type MnNi and MnGa.* Journal of Magnetism and Magnetic Materials **187**, 105–112 (1998).

[81] D. Spisak and J. Hafner: *Electronic and magnetic structure of Mn-Ni alloys in two and three dimensions.* Journal of Physics: Condensed Matter

**11**, 6359 (1999).

[82] V. V. Godlevsky and K. M. Rabe: *Soft tetragonal distortions in ferromagnetic $Ni_2MnGa$ and related materials from first principles*. Physical Review B **63**, 134407 (2001).

[83] M. F. Toney, M. G. Samant, T. Lin, and D. Mauri: *Thickness dependence of exchange bias and structure in MnPt and MnNi spin valves*. Applied Physics Letters **81**, 4565–4567 (2002).

[84] C. Loch, W. Maass, B. Ocker, and K. Röll: *Structure and annealing of NiMn spin valves*. Journal of Applied Physics **85**, 4460–4462 (1999).

[85] M. S. Lund, M. R. Fitzsimmons, S. Park, and C. Leighton: *Temperature-dependent magnetic interface location in interdiffused exchange biased bilayers*. Applied Physics Letters **85**, 2845–2847 (2004).

[86] C. Tieg, W. Kuch, S. G. Wang, and J. Kirschner: *Growth, structure, and magnetism of single-crystalline $Ni_xMn_{100-x}$ films and NiMn/Co bilayers on Cu(001)*. Physical Review B **74**, 094420 (2006).

[87] J. Reinhardt, M.and Seifert, M. Busch, and H. Winter: *Magnetic interface coupling between ultrathin Co and $Ni_xMn_{100-x}$ films on Cu(001)*. Physical Review B **81**, 134433 (2010).

[88] N. Cheng, J. Ahn, and K. M. Krishnan: *Epitaxial growth and exchange biasing of PdMn/Fe bilayers grown by ion-beam sputtering*. Journal of Applied Physics **89**, 6597–6599 (2001).

[89] R. F. C Farrow, R. F. Marks, M. F. Toney, S. David, A. J. Kellock, J. A. Borchers, K. V. O'Donovan, and D. J. Smith: *Spontaneous chemical ordering and exchange bias in epitaxial $Mn_{0.52}Pd_{0.48}/Fe(001)$ bilayers prepared at room temperature*. Applied Physics Letters **80**, 808–810 (2002).

[90] F. Bruno, D. Cvetko, L. Floreano, R. Gotter, C. Mannori, L. Mattera, R. Moroni, S. Prandi, S. Terreni, A. Verdini, et al.: *Combined photoelectron and X-ray diffraction from ultrathin Fe films on $Cu_3Au(001)$*. Applied Surface Science **162**, 340–345 (2000).

[91] C. Mitsumata, A. Sakuma, and K. Fukamichi: *Mechanism of the exchange-bias field in ferromagnetic and antiferromagnetic bilayers*. Physical Review B **68**, 014437 (2003).

[92] W. H. Meiklejohn and C. P. Bean: *New magnetic anisotropy*. Physical Review **105**, 904 (1957).

[93] W. H. Meiklejohn and C. P. Bean: *New magnetic anisotropy*. Physical Review **102**, 1413 (1956).

[94] W. H. Meiklejohn: *Exchange anisotropy—a Review*. Journal of Applied Physics **33**, 1328–1335 (1962).

[95] J. Nogués, J. Sort, V. Langlais, V. Skumryev, S. Suriñach, J. S. Muñoz, and M. D. Baró: *Exchange bias in nanostructures*. Physics Reports **422**, 65–117 (2005).

[96] J. Nogués and I. K. Schuller: *Exchange bias*. Journal of Magnetism and Magnetic Materials **192**, 203–232 (1999).

[97] J. Nogués, D. Lederman, T. J. Moran, I. K. Schuller, and K. V. Rao: *Large exchange bias and its connection to interface structure in $FeF_2$-Fe bilayers*. Applied Physics Letters **68**, 3186–3188 (1996).

[98] R. Jungblut, R. Coehoorn, M. T. Johnson, and J. Stegge: *Orientational dependence of the exchange biasing in molecular-beam-epitaxy-grown $Ni_{80}Fe_{20}/Fe_{50}Mn_{50}$ bilayers*. Journal of Applied Physics **75**, 6659–6664 (1993).

[99] B. Dieny, V. S. Speriosu, S. Metin, S. S. P Parkin, B. A. Gurney, P. Baumgart, and D. R. Wilhoit: *Magnetotransport properties of magnetically soft spin-valve structures*. Journal of Applied Physics **69**, 4774–4779 (1991).

[100] B. Dieny, V. S. Speriosu, S. S. P Parkin, B. A. Gurney, D. R. Wilhoit, and D. Mauri: *Giant magnetoresistive in soft ferromagnetic multilayers*. Physical Review B **43**, 1297 (1991).

[101] J. Nogués, T. J. Moran, D. Lederman, I. K. Schuller, and K. V. Rao: *Role of interfacial structure on exchange-biased $FeF_2$-Fe*. Physical Review B **59**, 6984 (1999).

[102] T. J. Moran, J. Nogués, D. Lederman, and I. K. Schuller: *Perpendicular coupling at Fe-$FeF_2$ interfaces*. Applied physics Letters **72**, 617–619 (1998).

[103] J. Nogués, D. Lederman, T. J. Moran, and I. K. Schuller: *Positive Exchange Bias in $FeF_2$-Fe Bilayers*. Physical Review Letters **76**, 4624 (1996).

[104] C. Leighton, J. Nogués, H. Suhl, and I. K. Schuller: *Competing interfacial exchange and Zeeman energies in exchange biased bilayers*. Physical Review B **60**, 12837 (1999).

[105] C. Hou, H. Fujiwara, and K. Zhang: *Structural origin of coercivity enhancement and exchange-bias field in double antiferromagnet/ferromagnet bilayers.* Applied Physics Letters **76**, 3974–3976 (2000).

[106] C. Leighton, J. Nogués, B. J. Jönsson-Åkerman, and I. K. Schuller: *Coercivity enhancement in exchange biased systems driven by interfacial magnetic frustration.* Physical Review Letters **84**, 3466 (2000).

[107] F. Radu and H. Zabel: *Exchange bias effect of ferro-/antiferromagnetic heterostructures.* in: Magnetic heterostructures,Springer Tracts in Modern Physics, Springer (2008).

[108] A. Aharoni: *Introduction to the Theory of Ferromagnetism.* Vol. 109, Clarendon Press (2000).

[109] J. S. Jiang, G. P. Felcher, A. Inomata, R. Goyette, C. Nelson, and S. D. Bader: *Exchange-bias effect in Fe/Cr(211) double superlattice structures.* Physical Review B **61**, 9653 (2000).

[110] A. P. Malozemoff: *Random-field model of exchange anisotropy at rough ferromagnetic-antiferromagnetic interfaces.* Physical Review B **35**, 3679 (1987).

[111] J. Esser, U. Nowak, and K. D. Usadel: *Exact ground-state properties of disordered Ising systems.* Physical Review B **55**, 5866 (1997).

[112] Y. Imry and S. K Ma: *Random-field instability of the ordered state of continuous symmetry.* Physical Review Letters **35**, 1399 (1975).

[113] U. Nowak, K. D. Usadel, J. Keller, P. Miltényi, B. Beschoten, and G. Güntherodt: *Domain state model for exchange bias. I. Theory.* Physical Review B **66**, 014430 (2002).

[114] B. Beckmann, U. Nowak, and K. D. Usadel: *Asymmetric reversal modes in ferromagnetic/antiferromagnetic multilayers.* Physical Review Letters **91**, 187201 (2003).

[115] P. Miltényi, M. Gierlings, J. Keller, B. Beschoten, G. Güntherodt, U. Nowak, and K. D. Usadel: *Diluted antiferromagnets in exchange bias: Proof of the domain state model.* Physical Review Letters **84**, 4224 (2000).

[116] A. Misra, U. Nowak, and K. D. Usadel: *Control of exchange bias by diluting the antiferromagnetic layer.* Journal of Applied Physics **93**, 6593–6595 (2003).

[117] A. Misra, U. Nowak, and K. D. Usadel: *Structure of domains in an exchange-bias model.* Journal of Applied Physics **95**, 1357–1363 (2004).

[118] H. Shi, D. Lederman, and E. E. Fullerton: *Exchange bias in $Fe_xZn_{1-x}F_2/Co$ bilayers.* Journal of Applied Physics **91**, 7763–7765 (2002).

[119] A. Mougin, T. Mewes, M. Jung, D. Engel, A. Ehresmann, H. Schmoranzer, J. Fassbender, and B. Hillebrands: *Local manipulation and reversal of the exchange bias field by ion irradiation in FeNi/FeMn double layers.* Physical Review B **63**, 060409 (2001).

[120] T. Mewes, R. Lopusnik, J. Fassbender, B. Hillebrands, M. Jung, D. Engel, A. Ehresmann, and H. Schmoranzer: *Suppression of exchange bias by ion irradiation.* Applied Physics Letters **76**, 1057–1059 (2000).

[121] M. Ali, C. H. Marrows, M. Al-Jawad, B. J. Hickey, A. Misra, U. Nowak, and K. D. Usadel: *Antiferromagnetic layer thickness dependence of the IrMn/Co exchange-bias system.* Physical Review B **68**, 214420 (2003).

[122] J. Keller, P. Miltényi, B. Beschoten, G. Güntherodt, U. Nowak, and K. D. Usadel: *Domain state model for exchange bias. II. Experiments.* Physical Review B **66**, 014431 (2002).

[123] W. Kuch, L. I. Chelaru, F. Offi, J. Wang, M. Kotsugi, and J. Kirschner: *Three-dimensional noncollinear antiferromagnetic order in single-crystalline FeMn ultrathin films.* Physical Review Letters **92**, 017201 (2004).

[124] C. H. Marrows: *Three-dimensional exchange bias in $\{Co/Pd\}_N/FeMn$.* Physical Review B **68**, 012405 (2003).

[125] Y. Endoh and Y. Ishikawa: *Antiferromagnetism of $\gamma$ iron manganes alloys.* Journal of the Physical Society of Japan **30**, 1614–1627 (1971).

[126] S. Kawarazaki, K. Fujita, K. Yasuda, Y. Sasaki, T. Mizusaki, and A. Hirai: *Direct evidence for triple-Q spin-density wave in fcc antiferromagnetic Mn-Ni alloy.* Physical Review Letters **61**, 471 (1988).

[127] I. K. Schuller, R. Morales, X. Batlle, U. Nowak, and G. Güntherodt: *Role of the antiferromagnetic bulk spins in exchange bias.* Journal of Magnetism and Magnetic Materials **416**, 2–9 (2016).

[128] X. Chi, F. Ma, A. Luo, A. Du, J. Wang, and Y. Hu: *Role of antiferromagnetic bulk exchange coupling on exchange-bias propagation.* Physics Letters A **379**, 2772–2776 (2015).

[129] R. Morales, Z. P Li, J. Olamit, K. Liu, J. M. Alameda, and I. K. Schuller: *Role of the antiferromagnetic bulk spin structure on exchange bias.* Physical Review Letters **102**, 097201 (2009).

[130] A. C. Basaran, T. Saerbeck, J d. l. Venta, H. Huckfeldt, A. Ehresmann, and I. K. Schuller: *Exchange bias: The antiferromagnetic bulk matters.* Applied Physics Letters **105**, 072403 (2014).

[131] UHV Instruction Manual: *evaporator EFM3/4.* Omicron, Germany, (1999).

[132] M. P. Seah: *Quantitative Auger electron spectroscopy and electron ranges.* Surface Science **32**, 703–728 (1972).

[133] C. Davisson and L. H. Germer: *Diffraction of electrons by a crystal of nickel.* Physical Review **30**, 705 (1927).

[134] K. Heinz: *LEED and DLEED as modern tools for quantitative surface structure determination.* Reports on Progress in Physics **58**, 637 (1995).

[135] J. B. Pendry: *Low energy electron diffraction: the theory and its application to determination of surface structure.* Vol. 2, Academic Press (1974).

[136] G. Ertl and J. Küppers: *Low energy electrons and surface chemistry.* Vch Weinheim (1985).

[137] W. C. Lin, T. Y. Chen, L. C. Lin, B. Y Wang, Y. W. Liao, K. J. Song, and M. T. Lin: *Comparison of the crystalline structure, morphology, and magnetic properties of $\gamma$-phase $Mn/Cu_3Au(100)$ ultrathin films by varying the growth temperature.* Physical Review B **75**, 054419 (2007).

[138] M. Y. Khan: *Probing the antiferromagnetism of NiMn with ferromagnetic Ni in exchange-biased bilayers and trilayers on $Cu_3Au(001)$.* Ph. D. thesis, Freie Univärsität Berlin, (2012).

[139] W. Kuch, A. Dittschar, K. Meinel, M. Zharnikov, C. M. Schneider, J. Kirschner, J. Henk, and R. Feder: *Magnetic-circular-dichroism study of the valence states of perpendicularly magnetized Ni (001) films.* Physical Review B **53**, 11621 (1996).

[140] M. Zharnikov, A. Dittschar, W. Kuch, C. M. Schneider, and J. Kirschner: *Interplay between structure and magnetism in Fe/Cu(100) upon temperature variation.* Journal of Magnetism and Magnetic Materials **174**, 40–56 (1997).

[141] F. Offi, W. Kuch, and J. Kirschner: *Structural and magnetic properties of $Fe_xMn_{1-x}$ thin films on Cu(001) and on Co/Cu(001).* Physical Review B **66**, 064419 (2002).

[142] W. Braun: *Applied RHEED: reflection high-energy electron diffraction during crystal growth*. Vol. 154, Springer Science & Business Media (1999).

[143] F. Offi: *Magnetic interaction between antiferromagnetic and ferromagnetic films: $Co/Fe_{50}Mn_{50}$ bilayers on Cu(001)*. Ph. D. thesis, Universitäts- und Landesbibliothek Sachsen-Anhalt, (2002).

[144] Julian Chen: *Introduction to Scanning Tunneling Microscopy Third Edition*. Vol. 69, Oxford University Press, USA (2021).

[145] E. R. Moog and S. D. Bader: *Smoke signals from ferromagnetic monolayers: p(1× 1) Fe/Au(100)*. Superlattices and Microstructures **1**, 543–552 (1985).

[146] Z. Q. Qiu and S. D. Bader: *Surface magneto-optic Kerr effect (SMOKE)*. Journal of Magnetism and Magnetic Materials **200**, 664–678 (1999).

[147] K. Sato: *Measurement of magneto-optical Kerr effect using piezo-birefringent modulator*. Japanese Journal of Applied Physics **20**, 2403 (1981).

[148] T. Shinwari, I. Gelen, Y. A. Shokr, I. Kumberg, M. Sajjad, I. Ikramullah, W. Kuch, and M. Y. Khan: *Bulk and Interfacial Effects in the $Co/Ni_xMn_{100-x}$ Exchange-Bias System due to Creation of Defects by $Ar^+$ Sputtering*. Physica Status Solidi (RRL)–Rapid Research Letters **15**, 2100195 (2021).

[149] M. Stampe, P. Stoll, T. Homberg, K. Lenz, and W. Kuch: *Influence of ferromagnetic-antiferromagnetic coupling on the antiferromagnetic ordering temperature in $Ni/Fe_xMn_{1-x}$ bilayers*. Physical Review B **81**, 104420 (2010).

[150] K. Lenz, S. Zander, and W. Kuch: *Magnetic proximity effects in antiferromagnet/ferromagnet bilayers: The impact on the Néel temperature*. Physical Review Letters **98**, 237201 (2007).

[151] S. Maat, K. Takano, S. S. P Parkin, and E. E. Fullerton: *Perpendicular exchange bias of Co/Pt multilayers*. Physical Review Letters **87**, 087202 (2001).

[152] W. Kuch, F. Offi, L. I. Chelaru, M. Kotsugi, K. Fukumoto, and J. Kirschner: *Magnetic interface coupling in single-crystalline Co/FeMn bilayers*. Physical Review B **65**, 140408 (2002).

[153] B. Y. Wang, W. C. Lin, Y. W. Liao, K. J. Song, and M. T. Lin: *Depth-dependent fct to fcc strain relaxation in $Co_xNi_{1-x}/Cu_3Au(100)$ alloy films*. Surface Science **600**, 4517–4526 (2006).

[154] B. Schirmer, B. Feldmann, A. Sokoll, Y. Gauthier, and M. Wuttig: *Tetragonal distortion of Mn films on $Cu_3Au(100)$.* Physical Review B **60**, 5895 (1999).

[155] W. C. Lin, L. C. Lin, T. Y. Chen, B. Y. Wang, K. J. Song, and M. T. Lin: *Growth, structure, and magnetism of $\gamma$-phase Mn ultrathin films on $Cu_3Au(100)$.* Journal of Applied Physics **97**, 10K112 (2005).

[156] A. Tange, C. Gao, M. T. Chiang, C. T.and Lin, W. Wulfhekel, and J. Kirschner: *Magnetic Structure of Mn Films on $Cu_3Au(100)$ Revealed by Spin-Polarized Scanning Tunneling Microscopy.* Materials Transactions **56**, 1484–1487 (2015).

[157] J. Shen, Z. Gai, and J. Kirschner: *Growth and magnetism of metallic thin films and multilayers by pulsed-laser deposition.* Surface Science Reports **52**, 163–218 (2004).

[158] A. Sáenz-Trevizo and A. M. Hodge: *Nanomaterials by design: a review of nanoscale metallic multilayers.* Nanotechnology **31**, 292002 (2020).

[159] S. Mangin, D. Ravelosona, J. A. Katine, M. J. Carey, B. D. Terris, and E. E. Fullerton: *Current-induced magnetization reversal in nanopillars with perpendicular anisotropy.* Nature Materials **5**, 210–215 (2006).

[160] Y. Shiroishi, K. Fukuda, I. Tagawa, H. Iwasaki, S. Takenoiri, H. Tanaka, H. Mutoh, and N. Yoshikawa: *Future options for HDD storage.* IEEE Transactions on Magnetics **45**, 3816–3822 (2009).

[161] S. Ikeda, K. Miura, H. Yamamoto, K. Mizunuma, H. D. Gan, M. Endo, S. Kanai, J. Hayakawa, F. Matsukura, and H. Ohno: *A perpendicular-anisotropy CoFeB–MgO magnetic tunnel junction.* Nature Materials **9**, 721–724 (2010).

[162] D. C. Worledge, G. Hu, D. W. Abraham, J. Z. Sun, P. L. Trouilloud, J. Nowak, S. Brown, M. C. Gaidis, E. J. O'sullivan, and R. P. Robertazzi: *Spin torque switching of perpendicular Ta/CoFeB/MgO-based magnetic tunnel junctions.* Applied Physics Letters **98**, 022501 (2011).

[163] B.Y. Wang, C. H. Hsiao, B. X. Liao, C. Y. Hsu, T. H. Li, Y. L. Hsu, Y. M. Lai, M. S. Tsai, T. H. Chuang, and D. H. Wei: *Perpendicular magnetic anisotropy induced by NiMn-based antiferromagnetic films with in-plane spin orientations: Roles of interfacial and volume antiferromagnetic moments.* Physical Review B **104**, 024424 (2021).

[164] B. Y. Wang, N. Y. Jih, W. C. Lin, C. H. Chuang, P. J. Hsu, C. W. Peng, Y. C. Yeh, Y. L. Chan, D. H. Wei, and M. T. Chiang, W. C. Lin:

*Driving magnetization perpendicular by antiferromagnetic-ferromagnetic exchange coupling.* Physical Review B **83**, 104417 (2011).

[165] B.Y Wang, J. Y. Hong, K. H. Ou Yang, Y. L. Chan, D. H. Wei, H. J. Lin, and M. T. Lin: *How antiferromagnetism drives the magnetization of a ferromagnetic thin film to align out of plane.* Physical Review Letters **110**, 117203 (2013).

[166] B. Y. Wang, C. C. Chiu, W. C. Lin, and M. T. Lin: *Enhanced perpendicular magnetic anisotropy in Fe/Mn bilayers by incorporating ultrathin ferromagnetic underlayer through magnetic proximity effect.* Applied Physics Letters **103**, 042407 (2013).

[167] P. Kuświk, P. L. Gastelois, M. M. Soares, H. C. N. Tolentino, M. Santis, A. Y. Ramos, A. D. Lamirand, M. Przybylski, and J. Kirschner: *Effect of CoO/Ni orthogonal exchange coupling on perpendicular anisotropy of Ni films on Pd (001).* Physical Review B **91**, 134413 (2015).

[168] B. Y. Wang, P. H. Lin, M. S. Tsai, C. W. Shih, M. J. Lee, C. W. Huang, N. Y. Jih, P. Y. Cheng, and D. H. Wei: *Crucial role of interlayer distance for antiferromagnet-induced perpendicular magnetic anisotropy.* Physical Review B **92**, 214435 (2015).

[169] B. Y. Wang, M. S. Tsai, C. W. Huang, C. W. Shih, C. J. Chen, K. Lin, J. J. Li, N. Y. Jih, C. I. Lu, T. H. Chuang, and D. H. Wei: *Effects of the antiferromagnetic spin structure on antiferromagnetically induced perpendicular magnetic anisotropy.* Physical Review B **96**, 094416 (2017).

[170] N. Y. Jih, B. Y. Wang, Y. L. Chan, D. H. Wei, and M. T. Lin: *Extending the Control of Antiferromagnetic–Ferromagnetic Exchange Coupling on Perpendicular Magnetization into the Soft Magnetic Regime.* Applied Physics Express **5**, 063008 (2012).

[171] K. Yakushiji, T. Saruya, H. Kubota, A. Fukushima, T. Nagahama, S. Yuasa, and K. Ando: *Ultrathin Co/Pt and Co/Pd superlattice films for MgO-based perpendicular magnetic tunnel junctions.* Applied Physics Letters **97**, 232508 (2010).

[172] J. C. Slonczewski: *Current-driven excitation of magnetic multilayers.* Journal of Magnetism and Magnetic Materials **159**, L1–L7 (1996).

[173] H. Xing, K. Keshoju, S. M. Zhou, and L. Sun: *Field cooling induced perpendicular exchange bias in FeMn/(FeNi/FeMn) _n multilayers.* Journal of Applied Physics **101**, 09E509 (2007).

[174] B. Y Wang, C. Huang, M. S. Tsai, K. Lin, C. C. Chung, N. Y Jih, C. I. Lu, T. H. Chuang, and D. H. Wei: *Promoting control of antiferromagnet-induced perpendicular magnetic anisotropy in magnetic multilayers: Effects of applying in-plane magnetic supporting layers*. Applied Physics Express **12**, 043004 (2019).

[175] B. Zhang, C. B. Wu, and W. Kuch: *Tailoring interlayer coupling and coercivity in Co/Mn/Co trilayers by controlling the interface roughness*. Journal of Applied Physics **115**, 233915 (2014).

[176] N. N. Phuoc, N. P. Thuy., N. A. Tuan, N. T. Thanh, N. n Thanh Nam, et al.: *Coexistence of positive and negative exchange bias in CrMn/Co bilayers*. Journal of Magnetism and Magnetic Materials **298**, 43–47 (2006).

[177] H. Ohldag, H. Shi, E. Arenholz, J. Stöhr, and D. Lederman: *Parallel versus antiparallel interfacial coupling in exchange biased Co/FeF $_2$*. Physical Review Letters **96**, 027203 (2006).

[178] W. Kuch, J. Gilles, S. S. Kang, S. Imada, S. Suga, and J. Kirschner: *Magnetic-circular-dichroism microspectroscopy at the spin reorientation transition in Ni(001) films*. Physical Review B **62**, 3824 (2000).

[179] W. Kuch, F. Offi, L. I. Chelaru, J. Wang, K. Fukumoto, M. Kotsugi, J. Kirschner, and J. Kuneš: *Huge magnetocrystalline anisotropy of X-ray linear dichroism observed on Co/FeMn bilayers*. Physical Review B **75**, 224406 (2007).

[180] P. Bruno: *Tight-binding approach to the orbital magnetic moment and magnetocrystalline anisotropy of transition-metal monolayers*. Physical Review B **39**, 865 (1989).

# List of Acronyms

| | |
|---|---|
| AD | areal density |
| AES | Auger electron spectroscopy |
| AFM | antiferromagnet |
| ALF | artificially layered film |
| AMR | anisotropic-magnetoresistance |
| CMA | cylindrical mirror analyzer |
| EB | exchange-bias |
| FC | field cooled |
| FCC | face centre cubic |
| FCT | face centre tetragonal |
| FM | ferromagnet |
| GMR | giant-magnetoresistance |
| H | applied field |
| $H_c$ | coercive field |
| HDD | hard disk drive |
| $H_{eb}$ | exchange-bias field |
| IBM | International Business Machines Corporation |
| IP | in-plane |
| IT | information technology |
| I(V) | intensity versus energy |
| LEED | low-energy electron diffraction |
| L-MOKE | longitudinal magneto-optic Kerr effect |
| MEED | medium-energy electron diffraction |
| ML | monolayer |
| MOKE | magneto optic Kerr effect |
| MRAM | magnetic random access memory |
| OoP | out of plane |
| PMA | perpendicular magnetic anisotropy |
| P-MOKE | polar magneto optic Kerr effect |
| RHEED | reflection high-energy electron diffraction |
| SNR | signal-to-noise ratio |
| SP-STM | spin-polarized scanning tunneling microscopy |
| STM | scanning tunneling microscopy |

| | |
|---|---|
| $T_b$ | blocking temperature |
| $T_c$ | Curie temperature |
| TMR | tunneling-magnetoresistance |
| T-MOKE | transverse magneto-optic Kerr effect |
| $T_N$ | Néel temperature |
| UHV | ultra-high vacuum |
| ZFC | zero-field cooled |

# Selbstständigkeitserklärung

Hiermit versichere ich, die vorliegende Dissertation eigenständig und ausschließlich unter Verwendung der angegebenen Quellen und Hilfsmittel angefertigt zu haben. Die vorliegende Arbeit ist in dieser oder anderer Form zuvor nicht als Prüfungsarbeit zur Begutachtung vorgelegt worden.

Berlin, den

Tauqir Shinwari

# Appendix

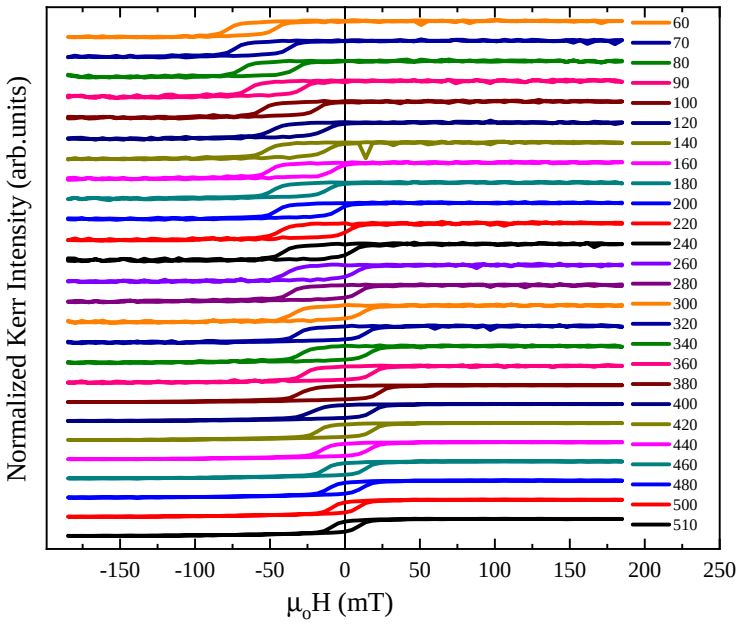


**Figure 6.18:** Normalized hysteresis loops for 10 ML Ni/44 ML Mn/5 ML Ni/5 ML Co/$Cu_3Au$(001) trilayer measured with polar MOKE at different temperatures, deposited at room temperature.

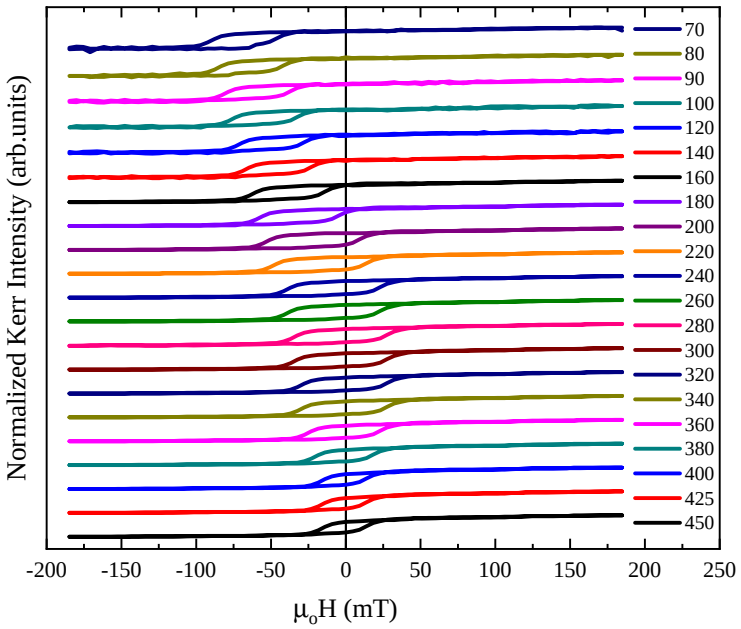


**Figure 6.19:** Normalized hysteresis loops for 10 ML Co/44 ML Mn/5 ML Ni/5 ML Co/$Cu_3Au$(001) trilayer measured with longitudinal MOKE at different temperatures, deposited at room temperature.

# List of publications

## Publications

- Tauqir Shinwari, Ismet Gelen, Yasser A. Shokr, Ivar Kumberg, Ikramullah, Muhammad Sajjad, Wolfgang Kuch, and M. Yaqoob Khan. Bulk and interfacial effects in the Co/$Ni_xMn_{100-x}$ exchange-bias system due to creation of defects by Ar ion sputtering. Phys. Status Solidi RRL **15**, 2100195 (2021).

- Ivar Kumberg, Evangelos Golias, Niko Pontius, Rahil Hosseinifar, Karl Frischmuth, Ismet Gelen, Tauqir Shinwari, Sangeeta Thakur, Schüßler-Langeheine, Peter Oppeneer, and Wolfgang Kuch. Accelerating the laser-induced demagnetization of a ferromagnetic film by antiferromagnetic order in an adjacent layer. Phys. Rev. B **102**, 214418 (2020).

- Tauqir Shinwari, Ismet Gelen, Melek Villanueva, Ivar Kumberg, Yasser A. Shokr, and Wolfgang Kuch. Growth, structure, and magnetic properties of artificially layered NiMn in contact to ferromagnetic Co on $Cu_3Au(001)$ (in preparation).

- Ivar Kumberg, Evangelos Golias, Sebastien Hadjadj, Rahil Hosseinifar, Sangeeta Thakur, Tauqir Shinwari, Ismet Gelen, Niko Pontius, Schüßler-Langeheine, Clemens von Korf Schmising, Sangeeta Sharma, and Wolfgang Kuch. Laser-induced magneto-optical changes in resonant X-ray reflectivity measurements (in preparation).

## Talk/Posters

- Tauqir Shinwari, Ismet Gelen, Ivar Kumberg, Yasser A. Shokr, Muhammad Sajjad, Ikramullah, M. Yaqoob Khan, Wolfgang Kuch. **Talk**: Bulk and interfacial effects in the Co/$Ni_xMn_{100-x}$ exchange-bias system due to creation of defects by Ar ion sputtering. $84^{th}$ Annual Meeting of DPG and DPG-Tagung (DPG Meeting) of the Condensed Matter Section (SKM), online (27.09 - 1 .10.2021)

- Tauqir Shinwari, Ismet Gelen, Melek Villanueva, Ivar Kumberg, Yasser A.

Shokr, Wolfgang Kuch. **Poster**: Growth, structure, and magnetic properties of artificially layered NiMn in contact to ferromagnetic Co on $Cu_3Au(001)$. $84^{th}$ Annual Meeting of DPG and DPG-Tagung (DPG Meeting) of the Condensed Matter Section (SKM), online (27.09 - 1 .10.2021)

- Ismet Gelen, Tauqir Shinwari, Yasser A. Shokr, Evangelos Golias, and Wolfgang Kuch. **Poster**: Scanning tunneling microscopy study of submonolayer growth of $Mn_x$ $Au_{1-x}$ on Cu(001). DPG-Frühjahrstagung (DPG Spring Meeting) of the Surface Science Division, online (01 - 04.03.2021)

- Ivar Kumberg, Evangelos Golias, Ismet Gelen, Rahil Hosseinifar, Sangeeta Thakur, Tauqir Shinwari, Jendrik Gördes, Schüßler-Langeheine, Sangeeta Sharma, Peter Oppeneer, Wolfgang Kuch. **Poster**: Effects of antiferromagnetic coupling and interfaces on light induced (de-)magnetization dynamics investigated by pump-probe soft X-ray reflectivity. Ultrafast Spintronic Phenomena and Materials (USPM), Ostrov, Czech Republic (02.-05.03.2020)

- Tauqir Shinwari, M. Yaqoob Khan, Ismet Gelen, Ivar Kumberg, Yasser A. Shokr, Evangelos Golias, and Wolfgang Kuch. **Poster**: Influence of defects inside the ($Ni_xMn_{100-x}$) antiferromagnetic layer on exchange bias in $Co/Ni_xMn_{100-x}$ bilayers. DPG Spring Meeting 2019 of the Condensed Matter Section, Regensburg (31.03.–05.04.2019)

- Ivar Kumberg, Karl Frischmuth, Tauqir Shinwari, Ismet Gelen, Lalmin Kipgen, Lucas Arruda, Fabian Nickel, Evangelos Golias, Wolfgang Kuch. X-ray reflection studies on Ni/NiMn and Co. **Poster**: The European Magnetism Association (ESM), Krakow, Poland, (17.-28.09.2018)

- Tauqir Shinwari, M. Yaqoob. Khan, Ikram Ullah, M. Sajjad, Izran Ullah, Y. A. Shokr, and W. Kuch. **Poster**: Influence of Bulk and Interface Defects in the Antiferromagnetic Layer for the Exchange-Bias Effect 2018 Joint Meeting of the DPG and EPS Condensed Matter Divisions, Berlin (11.–16.03.2018)

# Acknowledgements

"First of all, I wish to express my immense gratitude to my Ph.D. supervisor Prof. Dr. Wolfgang Kuch for providing me an opportunity to do my Ph.D. work in his research group. He always offered me professional guidance and encouragement throughout this research work. Without his valuable help, it would have been almost impossible for me to accomplish this job.

I thank Prof. Dr. Katharina J. Franke for her willingness to co-assess this thesis. Special thanks to the committee of my PhD thesis and defense. I warmly acknowledge the help of my friends and lab fellows Dr. Yasser Shokr, Dr. Sangeeta Thakur, Dr. Evangelos Golias, Ivar Kumberg, Ismet Gelen, Dr. Melek Villanueva, Dr. Muhammad Yaqoob Khan, Rahil Hosseinifar, and all other members of AG Kuch for providing me with a cooperative, memorable company and a feasible working environment. I can not forget the amicable behavior and selfless assistance from Dr. Matthias Bernien at the start of my Ph.D. Special thanks to the AG Kuch secretary Marion Badow for helping me on many occassions and to Engr. Uwe Lipowski for technical assistance. Many thanks to our former group fellows for their cooperation. I am very thankful for my country's fellow friends, especially Irtaza Hassan and Jiggz club; their company gave me a memorable time during my stay in Berlin. I am also thankful to the cryogenic laboratory, electronics, and machine-parts repairing workshops for assisting me having the working lab. I am grateful to the Senator of District Khyber (Ex-FATA), Pakistan, and Freie Universität Berlin, for their financial support during my stay in Germany. In the end, I consider it obligatory to acknowledge and thank all members of my family, parents, uncles, and my siblings. My parents' prayers and moral support always strengthened me whenever I felt weak and alone being miles away from them. I dedicate my thesis to my wife, Mahnoor Shinwari, her love and care always encouraged me to do my level best, and to my uncle Muhammad Yousaf Shinwari for always being there for my family in the crises"